Politecnico di Milano

Physics Department

The Role of Materials and Device Engineering in Photoelectrochemical Hydrogen Production from Hybrid Organic Systems

Doctoral Program in Physics - Cycle: XXXIII

Ph.D. Candidate: Antonio Alfano

Supervisor: Dr. Fabio Di Fonzo

Tutor: Prof. Guglielmo Lanzani

PhD Program Coordinator: Prof. Marco Finazzi

Abstract

The dramatic impact of fossil fuels exploitation is becoming more and more evident, with consequences potentially irreversible if actions will not be taken in due time. In this scenario, promoting the penetration of renewable sources in the energetic market plays a fundamental role. Solar energy holds the potential to replace high carbon-emitting sources due to its high abundance and widespread distribution. To this end, photoelectrochemical hydrogen production gained momentum through the years, as it allows to directly produce H_2 when photons with sufficient energy are absorbed by a semiconducting material immersed in an electrochemical solution.

The focus of this Ph.D. thesis will be the current challenges and future potential development of hybrid photocathodes (HPC) for Hybrid Organic Photoelectrochemical water splitting (HOPEC - WS). Furthermore, some relevant touchpoints with the field of hybrid organic perovskite solar cells (PSC) will be discussed. To this extent, the very first demonstration of a working tandem system employing solely organic based photoactive materials will be unveiled. This system, where a state-of-the-art HPC is coupled to a high performing PSC, achieves substantial solar-to-hydrogen (STH) efficiency exceeding 2%, comparable to similar systems based on inorganic semiconductors. A tailor-made model has then been developed and validated through the achieved experimental results. This allowed to perform a sensitivity analysis which highlighted the most influential HPC-related parameters that need to be improved to target 10% STH and 20% STH in the short- and long-term perspective.

Successively a first step toward this short-term goal will be discussed, where the realization of an upgraded HPC will be presented focusing on two core topics. The first addresses the development of a novel WSe_2 hole selective layer (HSL) which properties will be tuned acting on the post deposition treatments, selectively accessing the 1T', 1T and 2H phases from the starting amorphous-nanocrystalline as-deposited matrix. The second one targets the replacement of the extensively studied P3HT donor polymer with the high performing PCDTBT *push-pull* copolymer to boost the photovoltage and photocurrent of the device. The optimized multi-layered architecture made of ITO/WSe_2/PCDTBT:PC70BM/TiO_2/RuO_2 is further proven to retain its performance both in neutral and acidic pH with a stability exceeding 14 hours operated at 0 V_{RHE}.

This is particularly relevant since the stability of organic based devices exposed to harsh environments represents one of the major obstacles on the way of their large-scale deployment. This applies both to the field of HOPEC, organic photovoltaic and particularly to PSC. To face this issue, a dedicated chapter will discuss how innovative solutions can be designed to impart moisture resistance to the latter class. By applying the knowledge of the field of HOPEC-WS to PSC device engineering, a novel P3HT-based HSL which embeds CuSCN nanoplateletets as water splitting active species has been developed. The efficiency of this layer in preventing moisture-related degradation of the solar cell is further demonstrated, stabilizing its performances in high RH environment up to 28 days.

Table of Contents

List of Figures

List Of Tables

Chapter 1
Introduction

The history of technological development is bound to the exploitation of a variety of energy sources. Tied in a cyclical fashion, the scientific progress beats the time of the current energetic scenario obsolescence. This concept motivates nowadays call to action to enable a transition to a sustainable energetic paradigm. The unsuitableness of a fossil-fuel based economy has shaped a broad panorama of topics where urgent actions must be taken in order to mitigate the increasingly evident environmental damages. Among the actions undertaken worldwide by several organizations, the European Commission has signed a *European Green Deal* (EGD)[1] which goal is to make Europe the first climate-neutral continent. This formally obliges each subscriber to plan and execute targeted initiatives to mitigate carbon emissions in relevant fields such as technological development, residential, transportation, industrial and energetic.

The point of contact of all these areas is the identification of a new energy vector. The rationale is to reduce the main source of Greenhouse Gas (GHG) emissions, where energy related activities account for 75% EU's total. Indeed, actions targeted to the replacement of fossil fuels are among the first steps taken under the EGD. Despite renewable sources accounted for 17% of the EU gross final energy consumption, the intermittent nature of this sources is hampering their penetration to the market. Solar energy conversion in electricity through photovoltaic (PV) cells stems as clear example. Considering a typical power distribution demand from the grid over a working day, the main peaks will occur in the early morning and late afternoon, roughly coincident with the daily commute routine. However, the peak of solar irradiance falls in between these two windows of demand, as schematically depicted in Figure 1. Thus, avoiding grid overloads in low demand periods requires devising suitable energy accumulation technologies. A convenient way to store solar energy is to convert it into chemical energy and then, analogously to hydrocarbons, to release it on-demand. The concept of Solar Fuel falls under the aforementioned definition, among which hydrogen is emerging as a viable candidate.

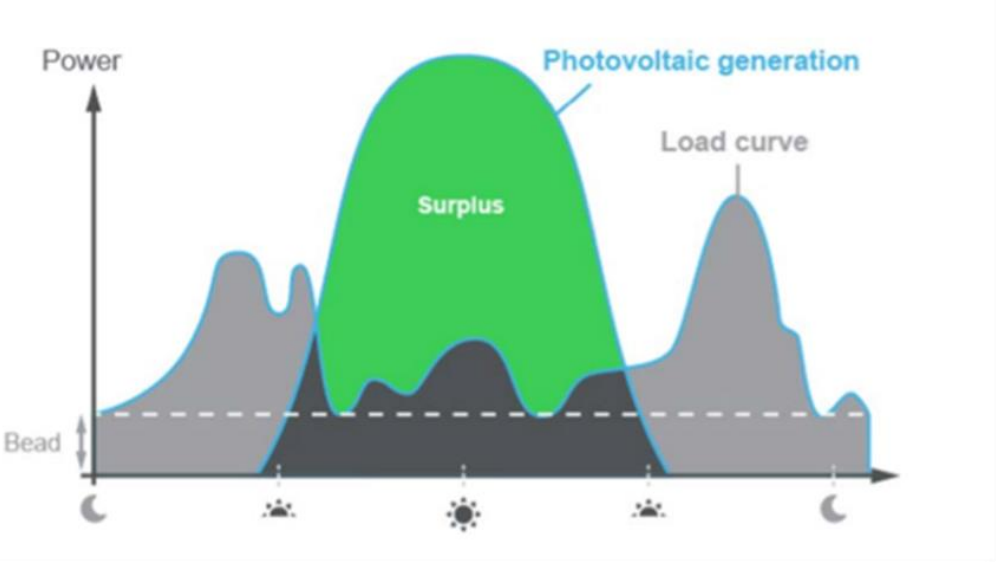

Figure 1: Schematic description of solar power generation vs grid power demand over the course of a typical day. Reference from Schneider Electric.

1.1 Hydrogen Economy

The use of hydrogen as a sustainable energy vector has been first envisaged by Prof. Bockris[2] in 1970 and currently represents the gateway to re-design a broad range of energy related activities. In the Hydrogen Economy framework, the simplest known molecule utilizations range from transportation to heat and electricity production through combustion engines, gas turbines and fuel cells. Thanks to its high abundancy, energy density and no pollutants by-products released during its utilization cycle, hydrogen holds the potential to match the expectations. Nevertheless, hydrogen utilization represents just part of the whole energy life cycle. A truly carbon-neutral scenario can only be achieved if hydrogen production itself comes from processes which do not lead to pollutant emission. Unfortunately, as of today only 4% of the global hydrogen production exploits renewable sources while the remaining 96% relies on fossil-fuels. The use of technologies like steam reforming unavoidably corrupts the concept of a sustainable Hydrogen Economy since CO_2 is still released in the environment, not at the end-use phase but in the production step. To cut the dependency from hydrocarbons, a novel source of hydrogen shall be identified. Water, the natural carrier of hydrogen, can be split into its constitutive elements at the expense of an energy input. Since the only way to decarbonise the whole process is to rely on renewable sources, attention must be paid to identifying a suitable technology which can enable the whole cycle to be carbon free.

This ultimately allowed to define the concept of Green Hydrogen, as opposed to Black and Grey Hydrogen which production leads to heavy / mild carbon emission. The EU is promoting a massive campaign which frames the current energy scenario

and sets the ground for Green Hydrogen to become a key player in the next decades. A comprehensive analysis can be found in the quoted documents[3,4], while here only some key figures will be provided to frame this topic.

The EU strategy focuses on how and where Green Hydrogen can have a substantial influence on decarbonising sectors such as industry, buildings, power and transportation. The key concept is that hydrogen can serve as a mean to accommodate the variable renewable energy supply, eventually allowing to reduce the energy-related CO_2 emission by more than 90% if suitable sector coupling is achieved. To this extent, hydrogen produced from direct exploitation of renewables can be channelled into sectors in which, at the current stage, no economically viable alternatives exist to replace fossil fuels. To meet these goals, the projected Green Hydrogen production in the 2020-2024 timeframe is set to 1 million tonnes. A graphical representation of how this clean fuel can be deployed to link sectors in which deep decarbonization is needed is shown in Figure 2.

To fuel this transition, EU is planning to pump in investments in the order of € 180-470 billion by 2050, estimating the amount of people employed in this sector to be around 1 million with a market revenue of € 630 billion [5]. This gives a taste of the urge of making hydrogen a truly sustainable alternative to fossil fuels.

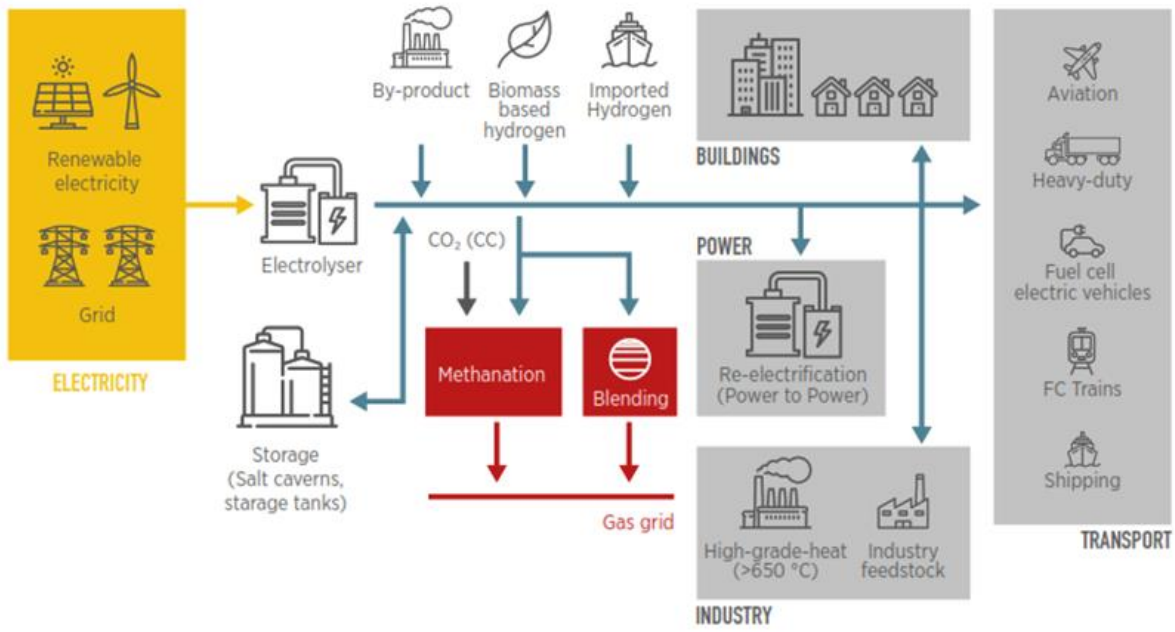

Figure 2: Sector coupling by means of sustainable hydrogen production. Blue lines represent H_2 flow across the different sectors from production to storage and utilization. Reference [4].

1.2 Solar-powered Water Splitting

At the current state, the most exploited renewable sources which can be coupled with hydrogen production systems are wind and solar. While wind power plants often require a dedicated infrastructure and can be located only in specific geographical locations, solar farms offer an unmatched flexibility. This is true both when considering their size and their location, as the main constraint is a suitable exposition to sunlight. As for their size, they can be modulated to operate both at the domestic and industrial scale.

Harvesting solar radiation opens up to two possible routes to produce hydrogen. The first, more exploited, works by coupling the standard PV module to a water electrolysis system. A second, more challenging approach, aims at combining these two technologies into a single photoelectrochemical/photocatalytic device. Here, photons harvested from the photoactive elements are directly employed to drive the water splitting reaction as the devices are directly immersed in an electrochemical cell. While this poses additional constraints for the devices to work efficiently, it offers several advantages connected to the lower system complexity which ultimately would lead to a lower final cost of the produced hydrogen.

1.2.1 Water Electrolysis

Hydrogen production from water electrolysis, from a pure electrochemical reaction point of view, can be discussed independently on the origin of source which powers it. The process itself is straightforward: two electrodes immersed in a solution can dissociate water into molecular hydrogen and oxygen provided that a sufficient potential is applied. The magnitude of this potential is highly dependent on the nature of the materials employed as electrodes. A material is said to catalyse efficiently the reaction occurring on one of the two electrodes if the required potential is close to the theoretical value. This value shall be treated taking into account each of the half reaction occurring at the electrode – electrolyte interface. Indeed, the full water splitting process comprises a cathodic reduction of protons into molecular hydrogen and an anodic oxidation of water to oxygen molecules.

This can be treated in detail writing down the overall process and their thermodynamic potential:

Overall Reaction	$2\,H_2O\,(l) \rightarrow 2\,H_2\,(g) + O_2\,(g)$	
Reduction	$2\,H^+(aq) + 2\,e^- \rightarrow H_2\,(g)$	$E^0_{red} = 0.00\,V_{NHE}$
Oxidation	$2\,H_2O\,(l) \rightarrow O_2\,(g) + 4\,H^+(aq) + 4\,e^-$	$E^0_{red} = 1.23\,V_{NHE}$

For the whole reaction to occur, both the anodic and cathodic reactions must occur simultaneously. The minimum potential requirement for the water splitting reaction to occur is of 1.23 V. This is identified by the potential difference between the cathodic and anodic reaction. The first occurs at 0 V_{NHE}, while the latter at 1.23 V_{NHE}. This holds true when only the electric energy supply is considered in the thermodynamic balance, being it equal to 237.2 kJ/mol. If also the heat energy is taken into account (48.6 kJ/mol), the overall voltage rises to 1.48 V, which is identified as the thermoneutral voltage.

Once the potential requirement is met, electrons can be transferred from the cathode to H^+ ions dissolved in the electrolyte and adsorbed on the surface to yield H_2 molecules, while electrons from the solution reach the anode and are transferred across the interface to give O_2 molecules. If this process occurs with no parasitic losses (Faradaic Efficiency = 1), two moles of hydrogen are produced for every mole of oxygen and the recorded current is proportional to the electrochemical reaction occurring at the electrode/electrolyte interface.

1.2.2 PV-Biased Electrolysis

Splitting water into its constitutive components is achieved at the expenses of a given applied potential. To obtain a truly carbon-neutral hydrogen, this potential needs to come from the exploitation of a renewable source. This is the rationale behind the coupling of electrolysis systems with the PV grid. These two technologies, when treated separately, are at a maturity level which allows to envisage a promising scenario for sustainable hydrogen production. This flexible approach allows to switch from direct electricity utilization to storage when the demand of the grid decreases. In this latter case, the excess electricity is employed to power the electrolysis system, thus converting it into hydrogen which can be stored, dispatched and utilized when needed. The drawbacks of this approach are tied to the complexity of the system and the unavoidable downtimes of the hydrogen generation unit, which must be turned on/off according to the grid demand. Furthermore, coupling these two systems holds some unavoidable losses which occur as power is transferred from the PV unit to the electrolysis module.

However, the translation of this concept to commercial applications is not straightforward. Indeed, by coupling a multijunction GaInP/GaAs/Ge solar cell to a PEM electrolyser STH efficiency of 24.4% was achieved [6]. However, multijunction solar cells of this type allowed to obtain a PCE of above 47% under concentrated illumination[7]. Thus, there is a significant gap when translating the performance of the PV component to hydrogen production through electrolysis. This can be explained recalling the thermodynamic potential requirement of the water splitting process. As previously discussed, the thermoneutral voltage for the reaction is of around 1.48 V. When it comes to real life operating conditions, this value can increase up to 1.9 V when all overpotentials all considered[8,9]. A multi-junction solar cell has a maximum power point potential between 2 and 3.5 V, depending on the type of architecture employed and the magnitude of solar concentration factor. Since no increase in STH is obtained beyond the thermodynamic requirement for the water splitting reaction, all the additional power coming from the solar cell is not effectively exploited. To overcome this issue, detailed optimization of the PV and electrolysis components is required in order to match the optimal working points of the two systems. Following this approach, Jia et al[10] demonstrated that STH efficiency as high as 30% can be obtained through PV-biased electrolysis.

This technology will become ever more appealing as the price of renewable electricity will drop in the short-term, as it will accommodate the sub-optimal performances of the system. Nevertheless, the pursuit of Green Hydrogen production will require a complete change in paradigm in which the development of integrated photoelectrochemical systems will play a fundamental role.

1.2.3 Photocatalytic and Photoelectrochemical Water Splitting

This alternative approach can be employed to aid the transition toward a Green Economy, as defined from the EU guidelines[3,5,11,12]. The first experimental evidence of the photocatalytic activity of a semiconductor was reported by Fujishima et al. in 1972[13] . In their work, a TiO_2 (photo)electrode was immersed in a water-based solution and, upon illumination, the formation of gas bubbles on its surface occurred. This effect arises when a semiconductor with a suitable bandgap absorbs photons, which leads to the promotion of an electron in its conduction band while leaving an unoccupied hole in its valence band. If these charges have enough potential, they can interact with the electrolyte to drive the oxygen and hydrogen evolution reactions.

The magnitude of the semiconductor band gap and the alignment of its conduction and valence band with respect to the hydrogen and oxygen evolution potential will ultimately define if a given material can drive the photocatalytic water splitting process. As previously described, a minimum amount of potential is required for the water splitting reaction to occur. This potential needs to be harnessed by photons absorption. Thus, a material which bandgap is larger than the minimum enthalpy requirement is needed as it allows to absorb photons with enough energy. Upon absorption, photon energy will be converted according to the level which will be occupied by the photoexcited electron. If the photoexcited electron in the conduction band lies higher in energy than the hydrogen evolution potential, it can participate in reducing protons to molecular hydrogen. Similarly, if the photoexcited hole in the valence band lies lower in energy than the oxygen evolution potential, it can contribute in oxidize water to molecular oxygen.

An optimal value of bandgap is in the order of 1.6 - 2 eV. If it exceeds this value, less photons will be absorbed and thus few charges are available to drive the overall reaction. By contrast, narrower band gap material would allow to photogenerate an higher amount of charges, but their potential could not be sufficient to provide enough thermodynamic driving force.

By coupling the knowledge of the photocatalytic process with electrochemical working principle of an electrolyser, a photoelectrochemical water splitting system can be designed. Here, two electrodes immersed in a solution are biased by the absorbed photons rather than from an external power supply. According to the nature of the employed materials, three different configurations can be adopted. Two of them rely on coupling a photoactive electrode with a catalytic one. If the photoactive electrode takes care of the HER, it shall be denoted as photocathode. If it is employed to catalyse the OER, it is defined as photoanode. These first two cases require that the photoactive component has to provide all the potential required to bias the overall water splitting reaction, matching the energetic requirements previously discussed in the case of photocatalytic water splitting. A third approach couples two photoactive material, obtaining a photoanode-photocathode system. Here, the potential requirement is split among the two photoelectrodes, as each of them need to separately address the requirement to bias the anodic/cathodic half reaction. Thus, for the photocathode to drive the HER it will be sufficient that its conduction band lies higher in energy than hydrogen evolution potential while for the photoanode to drive the OER its valence band must lie lower in energy than the oxygen evolution potential. This comes handy when selecting suitable semiconductors to be employed in the two photoelectrodes, as it further erases the minimum band-gap energy constraint.

As two photoactive materials are employed, it is crucial that both of them receive enough solar radiation. This opens up to two different system designs. The first, is

to place the two photoelectrodes in a side-by-side configuration. This allows both the devices to be reached by the same photon flux. Yet, it requires a higher surface area to realize a full system thus making this approach less appealing from a technical point of view. The most investigated approach aims at designing back-to-back configurations in which the photoactive layers are optically in series. The compactness of the system comes at the expenses of a more delicate material selection. Indeed, in order to avoid excessive shadowing effect, the bandgaps of the two materials must be complementary so that the performance of the system are preserved.

A noticeable example of this latter configuration allowed recently to realize the first metal oxide based full PEC system with substantial solar-to-hydrogen efficiency. In this work, Pan et al.[14] achieved 3% STH efficiency employing a Cu_2O based photocathode and a $BiVO_4$-based photoanode. This result, achieved through careful material selection and architecture optimization, renewed the interest in full PEC tandem system as a viable technology for clean hydrogen production.

1.2.4 PEC-PV Tandem Systems

A hybrid approach which sets as a compromise between the PEC and PV-biased water splitting is the PEC-PV configuration. In this case a PV cell is employed to provide the missing bias to a photoelectrode and catalytic electrode. The photoelectrode can be either a photoanode or a photocathode, while the other electrode is chosen to address the other half reaction. This is currently one of the most investigated approaches as it offers the opportunity of assessing the STH efficiency of PEC system by decoupling the influence of the anodic and cathodic reaction. Indeed, when a high performing photoelectrode is obtained it can be conveniently coupled with a catalyst and a PV biasing source and investigate its performance in a prototypical water splitting environment.

Lots of different systems have been realized following this approach and they are periodically gathered in several reviews of the field[15–18]. In this section some relevant examples of the broader literature on the topic will be highlighted. Monolithic devices have been realized, obtaining 19% STH[19] while integrated systems which also included thermal management strategies obtained similar efficiency (above 15%)[20]. Both these examples took advantage of the high performances of III-V solar cells, InGaP/InGaAs the first and a InGaP/InGaAs/Ge for the latter case. The catalytic reaction at the electrode/electrolyte interface was carried out employing high efficiency catalysts. These systems however required a careful encapsulation of the PEC components which would otherwise be subjected to heavy degradation. When considering unprotected photoelectrodes, STH

efficiency in the range of 5 – 8% can be achieved when metal oxide based devices are coupled with an external PV source [21–23]. Indeed, considering a system employing a PV biasing cell similar to the ones discussed for the monolithic and integrated case (InGaAsP/GaAs), 8.1% STH was obtained when coupled to a WO_3/$BiVO_4$/CoPi photoanode and a Pt cathode[23]. In this latter case, the high bandgap of the PEC component lowered the operating current density of the device and consequently the achievable STH.

A promising class of devices which allowed to replace the III-V PV component are Perovskite Solar cells (PSC). Thanks to their high photovoltage, PCE, easily tuneable bandgap and convenient fabrication techniques these devices allowed to minimize the number of employed components still obtaining PEC-PV systems with efficiency comparable with those achieved employing the more expensive III-V semiconductors. Indeed, STH as high as 7.9% have been obtained by coupling a $BaSnO_3$ based photoanode to a $(Cs_{0.05}(FA_{0.83}MA_{0.17})_{0.95}Pb(I_{0.83}Br_{0.17})_3)$ PSC and a Pt catalytic cathode[24]. Remarkably, this approach allowed to obtain this result without the need of employing a multijunction solar cell to reach the necessary bias. This further suggests that PSC can efficiently participate in sustainable hydrogen production when suitably coupled with a photoelectrode in a PEC-PV water splitting cell.

Overall, the flexibility provided by the PEC-PV approach offers an intriguing opportunity to validate the performances of a given component whether it is PEC, EC or PV.

1.3 Techno-Economic analysis

The main characteristic that will determine if a given technology is feasible for large scale deployment is the final cost of the produced hydrogen expressed as $\$/kgH_2$. Several techno economic analysis addressed this topic to quantify how the properties of a given system determine this final value. A comprehensive description carried out by Pinaud et al. [25] highlighted the correlation of the overall module cost, efficiency and lifetime on the cost of the final product. The analysis took as a reference scenario the target cost which is required to make PEC-hydrogen competitive with currently established technologies which was identified to be 10.4 $\$/kgH_2$. Once this constraint has been set, the corresponding required module cost, efficiency and lifetime have been calculated based on the available technical information. In the base case, this target can be met once systems will reach a 10% STH at a module cost of 153 $\$/m^2$ with a service life of 10 years (Figure 3).

While the first requirement has already been met, as highlighted in the previous section, the realization of systems which could match the cost and lifetime target can hardly be met relying on the materials employed so far. Reducing the fabrication cost of the PEC module could yield an appreciable decrease of the final price of produced H_2. To this extent, it would be meaningful to investigate how earth abundant materials which could benefit of low energy-intensive fabrication processes can be integrated in PEC-WS systems.

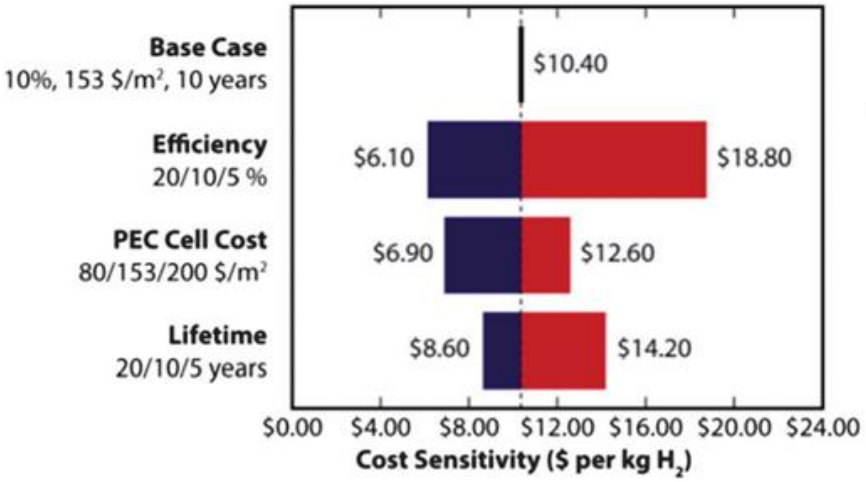

Figure 3: Sensitivity analysis for PEC systems. Here, the cost of H_2 with respect to the base case is evaluated as a function of the module efficiency, cost and lifetime. Reference [25].

1.4 Hybrid Organic Photoelectrochemical Water Splitting

An alternative approach which could allow to bridge appreciable efficiency and convenient fabrication techniques aims at replacing inorganic semiconductors with organic based materials. This is the rationale which paved the way for investigating the world of Hybrid Organic PEC-WS (HOPEC -WS). The idea of employing organic semiconductors in place of their inorganic counterpart follows the path which led to the development of organic photovoltaic (OPV) cells. Semiconducting polymers hold several distinctive features which allow to easily scale up their production through solution-processing techniques. Furthermore, they display a superior flexibility in terms of optoelectronic properties which can be tuned acting on the molecular composition of the polymer backbone.

The first attempts of assessing the photoelectrochemical performances of semiconducting polymers dates back to the 80', where the photoresponse of polythiophenes film and the subsequent hydrogen production was first demonstrated in aqueous environment[26]. The rate of performance increase of these seminal attempts followed the same trend of the akin field of OPV and shared

similar milestones, from the introduction of the bulk heterojunction to the use of charge selective contacts[27]. A more detailed description of the working principle of the mentioned components will be provided in Chapter 2.

The increasing understanding of charge generation dynamics in organic semiconductors lead to the development of hybrid photocathodes (HPC) which took advantage of a potential gradient within the device to enhance the charge collection efficiency and hydrogen production rate[28]. This concept further evolved in the employment of charge selective contacts which, when place in contact with a photoactive layer, allowed a 5-fold increase in performances[29]. This specific architecture employed a poly(3,4-ethylenedioxythiophene) polystyrene sulfonate (PEDOT:PSS) and an Al selective contacts which extracted photogenerated charges from a poly(3-hexylthiophene-2,5-diyl) (P3HT): phenyl-C61-butyric acid methyl ester (PCBM) bulk-heterojunction. The two materials selectively allowed holes to be collected at the PEDOT:PSS side and electrons at the aluminium side.

The field of HOPEC-WS gained momentum fuelled by these encouraging outcomes, resulting in several publications which contributed to gain awareness of the working principle of these devices[29–36]. Ultimately, a consolidated configuration for this kind of architectures employs several layers. The device is grown on a transparent conductive oxide (TCO) which serves as a back contact. The first layer in contact with the TCO is the hole selective layer (HSL) on top of which the organic photoactive material is deposited. This element is a blend of a donor polymer (D) and an electron acceptor (A), intimately intermixed to give a bulk-heterojunction (BHJ). Photogenerated electrons are extracted from this material through an electron selective layer (ESL) which makes the pair with the HSL. The architecture is finalized by depositing a catalytic layer which minimized the overpotential for the HER to occur.

Based on this optimized configuration, several milestone results have been obtained. Firstly, it was possible to demonstrate that organic semiconductors are intrinsically stable in the framework of an electrochemical cell, provided that no molecular oxygen is dissolved is the solution. The evidence of this was obtained by assessing the molecular structure of the organic photoactive layer before and after being exposed to the EC-environment. In this case, the Raman signature of the material did not show any modification in the wavenumber region of the C=C vibrations, as shown in Figure 4, while the main source of degradation arose from the electrochemical degradation of the SLs [27].

This result was also corroborated from a recent work which assessed the influence of charge accumulation within the BHJ on the full device performances. Here, Yao

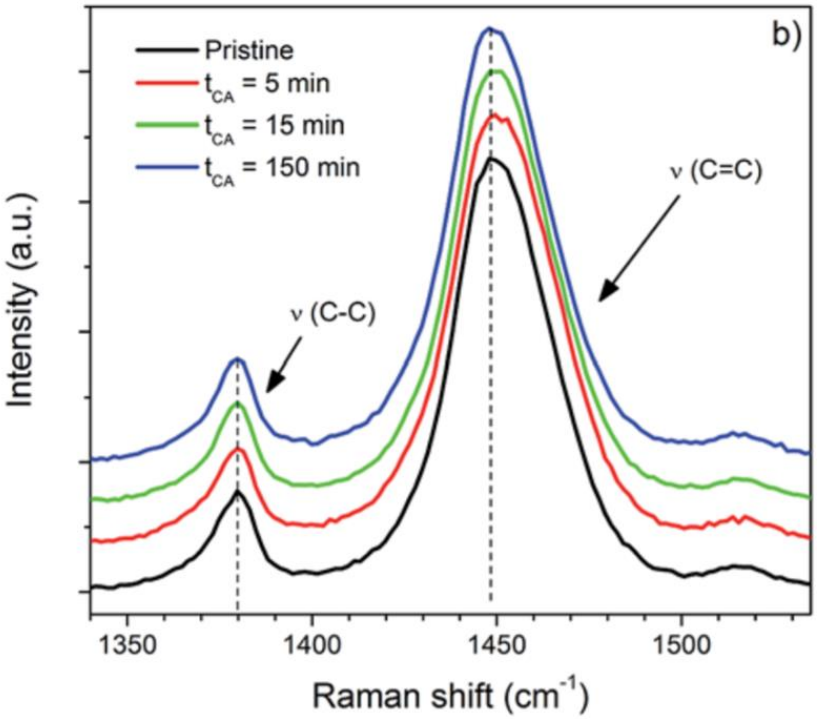

Figure 4: Raman spectra of the P3HT:PCBM bulk heterojunction of a hybrid photocathode at different moments of a chronoamperometry. The C=C and C-C vibrations frequencies are not affected, suggesting that no degradation is occurring on the photoactive layer. Ref [27].

et al.[36] demonstrated that when SL efficiently extract charges from the photoactive layer, the stability of the device could be extended up to 20 hours. By contrast, if charges accumulate (in particular in the fullerene-based acceptors) an irreversible degradation occurs after few minutes of operation. Additionally, several works demonstrated that organic-based HPC can operate at pH others than the acidic one with appreciable efficiency[34,35]. Yet, when outside from the optimal pH range, a remarkable loss in performance occurs[34].

Several reviews recently gathered the efforts of the HOPEC field and set the ground for future investigations [37–39]. The shared idea is that the necessary step toward enabling a new efficiency regime needs to address the upgrade of the photoactive layer and a careful selection of the selective layer materials. The first shall be obtained by looking up to the field of OPV, where high performing solar cells have been obtained employing both novel semiconducting polymers and non-fullerene acceptors. Thus, an extensive investigation of this novel materials is highly desired in order to boost the photovoltage and photocurrent contribution of HPCs. Similarly, optimization of the charge selective layer is paramount to increase the charge collection efficiency and to grant the electrochemical stability of the full HPC architecture.

1.5 Aim of This Work

Solar conversion technologies are a key enabling factor to meet the sustainability targets set by the EU Community. To mitigate the intrinsic fluctuations of the energy source, H_2 produced via direct conversion of sunlight, e.g. through photoelectrochemical water splitting, is regarded to be the most viable approach to obtain a clean energy vector which can shift the solar production peak.

While solar and electrochemical systems based on inorganic materials currently offer good reliability and efficiency, their overall cost is still hampering their large-scale deployment. The emerging field of organic based devices offers an intriguing perspective from the cost reduction point of view. Still, some effort is needed to fill the gap in terms of lifetime and performances which requires a detailed investigation and understanding of the physics which determines their behaviour. This applies both to the material- and device-related point of view.

Encouraged by the positive trend coming from the world of HOPEC-WS, and in a broader sense from the world of organic-based solar conversion technologies, this thesis will consist of three main parts, each treated in a dedicated chapter. The first (Chapter 3) aims at benchmarking the current development status of HPCs, highlighting the most promising approaches to improve their efficiency and stability. The outcome of this analysis will be used in Chapter 4 to successfully design a novel hybrid photocathode in which each layer will be engineered to maximize the overall device performances. Eventually in Chapter 5, the relevance of pursuing a synergistic approach to promote the development of organic-based systems will be presented through the realization of a HSL capable of imparting moisture resistance to PSCs through the addition of water splitting active species.

Through the years many works have been published on the development and optimization of novel hybrid organic photoelectrodes. So far, a full tandem system based on organic photoelectrodes has never been realized mainly due to the lack of availability of photoanodes which could efficiently bias the anodic half reaction. This somehow prevented to put the spotlight on the progress made on the cathodic counterpart which, indeed, achieved remarkable performances. Thus, Chapter 3 will focus on the realization of a HPC-PSC tandem where an optimized version of the HPC developed by Comas et al.[40] will be coupled with a high performing PSC. This system not only allowed to obtain the very first demonstration of unbiased water splitting from hybrid-organic systems but it also prompted the realization of a model which efficiently represented the behaviour of each employed component on the basis of several device-related parameters. From here, a sensitivity analysis will be performed with the goal of highlighting the HPC-related properties which need to be improved in order to increase the overall solar-to-hydrogen efficiency.

This further allowed to set two goals, for the near- and long-term perspective of these systems looking up to the akin field of organic photovoltaic.

In Chapter 4, the parameters highlighted in Chapter 3 will prompt the development of a novel HPC in which the materials employed in each layer will be specifically optimized to meet the target of the near-term perspective with a specific focus on granting the overall device electrochemical stability. The main focus will be set on identifying a suitable HSL and replacing the actual BHJ. The first represents the major bottleneck which often forces to set a trade-off between photoelectrochemical performances and stability. The latter is currently outdated by newly developed organic semiconductors which in the field of OPV allowed to obtain higher photovoltages and photocurrents. This reasoned approach eventually allowed to realize a HPC with remarkable performances and superior electrochemical stability. This result can be ascribed to the synergistic work of the highly tuneable HSL based on WSe_2, a p-type transition metal dichalcogenide (TMD) with excellent electrochemical stability and charge transport properties, and the novel BHJ based on the *push-pull* copolymer PCDTBT with enhanced photogeneration properties. Additionally, the performances are preserved both in acid and neutral environment, setting this newly developed device as a promising element for the realization of stable and high performing water splitting systems.

The relevance of selective contact engineering, highlighted in Chapter 4, will be further extended to the field of PSC in Chapter 5. Here, a synergistic effort across the worlds of HOPEC-WS and PV will offer an intriguing insight on the development of novel stabilization strategies for this promising class of solar cells. In particular, remarkable moisture resistance has been imparted to a PSC through the addition of water splitting active species to a P3HT based hole transport layer. This final section thus offers a novel perspective, hoping to foster the mutual interaction across these two fields.

Chapter 2
Device Architecture: Working Principle & Design Criteria

Hybrid Organic Inorganic Photocathode (HPC)

In the introductory chapter the highlights of how organic based photoelectrodes can participate in allowing the transition toward a sustainable energy scenario have been discussed. Here, the means to understand how this promising type of devices can meet this goal will be provided. To this extent, a detailed explanation of their working mechanisms is offered with an eye on the relevance of each layer on the whole system efficiency. By these means, the most relevant design criteria will be discussed which have to be considered while designing an efficient hybrid organic-inorganic photocathode for efficient and stable hydrogen production.

2.1 Organic Photoactive Layer

Being closely related to organic solar cells, the core of the HPC is a polymer-based photoactive layer. The relevance and opportunities offered by exploiting the properties of organic semiconductors have been discussed in the introductory chapter, herein the photogeneration process occurring within the BHJ will be discussed, together which what is the current understanding of the physics of this class of materials and which are the specific requirements which have to be met in order for them to work in the environment of an electrochemical cell.

From a molecular point of view, organic semiconductors are built upon an intricate network of sp^2 hybridized carbon atoms arranged in chains. This ultimately determines the electronic structure of these materials, as the sharing of π-orbitals between adjacent unities allows to create a cloud of delocalized electrons which can move freely across the network. As the conjugation increases, the energy required to promote an electron in the excited state is reduced. This determines the transition from insulating to semiconducting behaviour of the material, in which

the energy bandgap (E_G) is dictated by the difference in energy of the Highest Occupied Molecular Orbital (HOMO) and the Lowest Unoccupied Molecular Orbital (LUMO). These are indeed the organic equivalent of the Valence Band (VB) and Conduction Band (CB) of the inorganic counterpart. In the case of organic semiconductors, photons with enough energy can lead to the promotion of electron to the LUMO, leaving an unoccupied hole in the HOMO. However, due to the low dielectric constant of these materials ($\varepsilon_r \approx 2 - 4$) the interaction between the photogenerated electron-hole pair is poorly screened, leading to a short diffusion length and lifetime. In this case, tightly bound electron-hole pairs can be treated as excitons which are delocalized over adjacent chain segments. Being highly interacting, the fractions of photoexcited species which can be extracted prior recombination from this material is quite low. To overcome this issue, the OPV community designed a specific strategy which relied on the formation of an intimately intermixed network of a semiconducting polymer with an electron acceptor. This defined the concept of bulk heterojunction, in which high-electron affinity acceptor moieties were added to the π -conjugated donor polymer in order to provide a driving force which locally withdraws electrons from the tightly bound excitons. Efficient exciton dissociation was achieved when the characteristic dimensions of the two phases blended were in the order of 10 nm, comparable to the exciton diffusion length in the neat donor polymer [41,42].

Following this approach, semiconducting donor polymers and acceptor units blended in a BHJ allowed to achieve a remarkable increase in efficiency during the early rise of the world of OPV. A well-known example of this approach is the development of solar cells based on the archetypical donor homopolymer poly(3-hexylthiophene) (P3HT) blended with the fullerene derivative phenyl-C61-butyric acid methyl ester (PCBM) acceptor. Power conversion efficiency as higher than 4% have been achieved with this blend[43] which is remarkably higher than the values obtained on the very first demonstrations of OPV[44].

A further step toward high efficiency organic cells has been achieved by optimizing the molecular structure of the donor polymer. Indeed, through dedicated chemical engineering it was possible to realize high efficiency organic semiconductors in which the polymer backbone itself was made of repeating units where donor and acceptors moieties were simultaneously present. These materials, defined as push-pull copolymers, have enhanced dissociation efficiency of the photogenerated excitons as the sub-units with different electron affinity allowed to spatially delocalize quasi-free charge carriers, decreasing the recombination probability. Several works employing this novel class of polymers obtained PCE close and above 9%[45–51].

Additionally, the role of the acceptor material within the BHJ has been further clarified. Recent studies[47,49,51–55] demonstrated that by replacing fullerene-based

acceptor with specifically designed small molecules several beneficial effects can be achieved. First, by tuning their molecular structure, it is possible to determine the optical absorption properties of the material. This can be chosen to be complementary with the absorption profile of the donor polymer, allowing to harvest a larger fraction of incoming photons. This simultaneously allows to increase the achievable photocurrent and photovoltage of the cell, as undesired voltage losses are reduced and more charges are photogenerated. Recently, by exploiting the just described strategies, it was possible to boost the performance of OPV reaching record PCE as high as 15.6% for single junction cells[47].

2.1.1 Selection Criteria

Organic semiconductors, like their inorganic counterpart, need to fulfil several stringent requirements both from an energetic and structural point of view.

In order to drive hydrogen evolution, photogenerated charges need to have enough potential to bias this reaction. This condition can be met only if the LUMO level of BHJ lies higher in energy than the hydrogen evolution potential. This value is located at -4.4 V vs Vacuum (or 0 V vs RHE). Thus, if photogenerated electron are excited in a level which energy is higher (i.e. lies closer to the vacuum level) than -4.4 V vs Vacuum, these charges can theoretically bias the reaction.

If the first requirement is met, the employed material is also required to be electrochemically stable in the operating pH and potential range. Here, chemical degradation adds up to the already known topic of photodegradation due to the aggressive environment of the electrolytic solution. Nevertheless, the issue of degradation under illumination connected to air exposure is tied to the formation of oxygen radicals or exposure to high energy photons in the UV wavelength region. Both these degradation sources lead to a photochemical chain scission which reduce the conjugation of the polymer backbone, with detrimental effect on its charge transport properties[56,57].

It has to be taken into account that, as described in the dedicated Methods section, the solution employed for the electrochemical characterization undergoes a degassing step to remove dissolved molecular oxygen. Thus, working in cathodic de-aerated conditions should not harm the chemical integrity of the organic components, as pointed out in the work of Fumagalli et al.[27]. Since this analysis cannot be extended arbitrarily to all the available organic semiconductors, each case will be investigated in detail before integrating it into a full HPC architecture.

2.2 Charge Selective Contacts

By making use of charge selective contacts, it was possible increase the value of photocurrent of HPCs from few microamps to several milliamps. This gives a clear indication of the relevance of these layers on the overall device efficiency. The discussion of how these layers can contribute to the enhancement of the stability of the full device will be postponed to the following section. Indeed, while it surely represents a crucial point to address when selecting materials for this application, the fundamental aspect which determine the proper functioning of these layers is their electronic structure.

The rationale which leads to the development of a multi-layered structure employing suitably designed charge selective contacts comes from the knowledge of the working principle of a-Si PV modules. Efficient charge collection in this kind of solar cells is achieved thanks to two heavily doped regions of Si. Each of this region is doped to obtain a prevailing n- or p- type character. This induces an asymmetry in the electrostatic potential with respect to the pristine material. An intrinsic Si region is placed in between the p- and n- doped material. This defines the concept of p-i-n junction. The asymmetry felt by the intrinsic region leads to a preferential extraction/flow of photogenerated charges. This translates to a measurable current flowing across the cell.

When it comes to OPV and HOPEC, the necessity of having an additional driving force which prevents photogenerated charges to recombine is a direct consequence of the short exciton diffusion length. Here, establishing a built-in potential difference at the two opposites ends of the BHJ ensures that quasi-free charges which are split at the donor/acceptor interface flow in a preferential direction.

A parameter which can be useful to understand how a given material can induce this potential asymmetry is its work function (WF or Φ). This parameter defines the thermodynamic work (W) which needs to be spent in order to move an electron from the outer shell of a material to a point at an infinite distance away from it:

$$W = -e\Phi - E_F$$

As described from the equation, it is directly related to the position of the Fermi Energy (E_F) of the material. This latter value, combined with the knowledge of the position of the conduction band minimum and valence band maximum gives an indication of the p- or n- type nature of a material. A material which E_F lies close to the conduction band can be defined as n-type and conversely a material which E_F lies closer to the valence band can be defined as p-type.

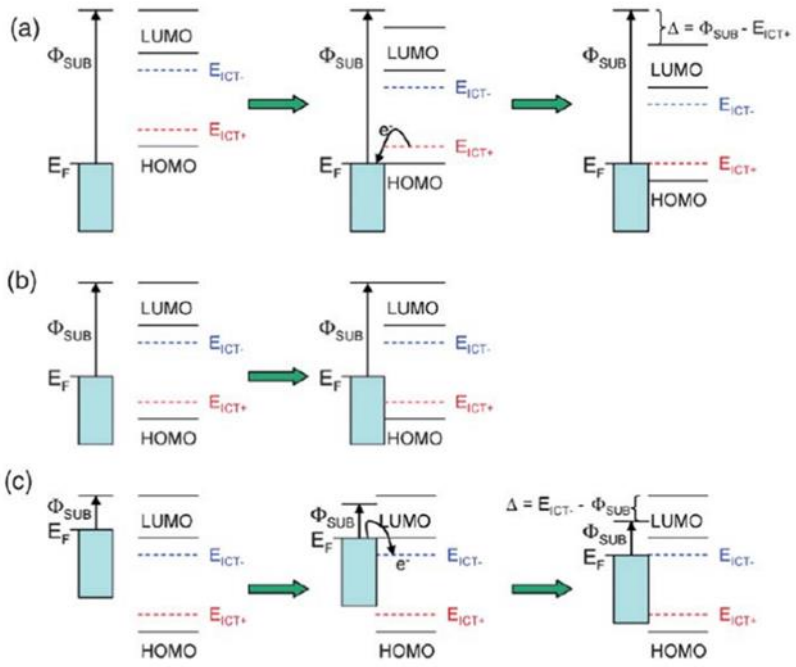

Figure 5: Illustration of the different possible scenarios occurring when a π conjugated organic molecule or polymer is physisorbed on a substrate surface. a) Øsub>EICT+: Fermi-level pinning to a positive integer charge-transfer state, b) EICT-<Øsub<EICT+: vacuum level alignment, and c) Øsub<EICT-: Fermi-level pinning to a negative integer charge transfer state. The charge-transfer-induced shift in vacuum level, Δ, is shown where applicable. Ref [58].

Whether a material behaves as n- or p-type gives an indication on how to couple it with BHJ, allowing to selectively extract holes through the p-type selective contact (hole selective contact – HSL) and electrons at the n-type selective contact (electron selective contact – ESL). The properties of the SC-BHJ interface exert a strong influence on the charge collection efficiency of the device. Also, the open circuit potential (V_{OC}) will be determined by the energy at which photogenerated charges are extracted from the BHJ. To understand how this coupling determines the extraction energy of the photogenerated charges it is useful to make use of the Integer Charge Transfer (ICT) model[58]. In the field of OPV, the ICT model allows to describe how charges flow across the interface between a semiconducting polymer and a conductive interfacial layer.

A semiconducting polymer energetic structure will be determined by the HOMO-LUMO levels position. If an electron is added to this polymer, the energy gained from the system through this process will be labelled as E_{ICT-}. By contrast, removing an electron can be done by providing to the system with an energy value equal to E_{ICT+}. These two states correspond to the quasi-Fermi levels of photogenerated electrons and holes respectively. To extract these charges without energy loss, the work function of the ESL should lie lower in energy (closer to the vacuum level) than the E_{ICT-} while the work function of the HSL should lie higher in energy (deeper with respect to the vacuum level) than E_{ICT+}. If these conditions are not met, a fraction of the energy will be lost as the charges are transferred across the interface, thus lowering the achievable V_{OC}. These conditions are

schematically summarized in Figure 5. The latter ($E_{ICT-} < \Phi < E_{ICT+}$) represents a more realistic scenario, thus it is reasonable to foresee that the measured open circuit potential will not match the theoretical value and it will be strongly dependant on the work function of the selective contacts[59].

Despite the difficulty of accessing meaningful information about the occurrence of Fermi level pinning in a real case scenario, it can be inferred that the relative position of SC-WF with respect to the HOMO-LUMO level of the BHJ will ultimately determine the potential gradient felt by the photogenerated charges, thus providing an effective charge selectivity.

Looking from the perspective of device-related parameters, the optimization of the charge selective contacts has a fundamental influence on the series and shunt resistance (R_s and R_{Sh} respectively) which in the diode equation determine the device current-voltage characteristics. In particular, a homogeneous, defect-free SL will lead to a high shunt resistance. The higher its value, the lower the amount of charges that will be lost in high-recombination rate paths within the architecture (also defined as leakage current). Similarly, a thin, highly conductive SL will lead to a low series resistance, thus allowing charge collection with minimal losses[60].

2.2.1 Selection Criteria

The description of the working principle of the SL is not sufficient by itself to provide a comprehensive tool to perform a reasoned material selection. To this extent, it will be now highlighted how these building blocks have to be integrated to maximize the overall system efficiency.

The energetic requirement is the first necessary condition which needs to be satisfied. On the HSL side, a p-type material is required, which work function should closely match the HOMO level of the donor polymer. The closer the alignment, the lower will be the amount of photovoltage lost due to charge transfer across the interface. Same holds true for the ESL, which work function should be as close as possible to the LUMO level of the electron acceptor. By matching these conditions, it will be possible to induce a built-in field which will allow a preferential charge flow throughout the whole HPC.

The first condition is not sufficient to guarantee a seamless integration of a material in a HPC architecture. When on a scale, a favourable energetic structure weight as much as the material's electrochemical stability. Designing an architecture in which one of the building blocks can't withstand the working environment poses serious concerns to the overall device stability. For this reason, no compromise can be accepted when assessing this property. A useful tool which

can be employed to perform a preliminary screening is the Pourbaix Diagram. This diagram displays the chemical state of a given element as a function of the pH and applied potential. The main drawback is that this analysis can hardly be extended to multimaterial compounds, thus requiring dedicated screening when it comes to less investigated materials.

It must also be considered that, given the multi-layered architecture, one of the two SLs will be crossed by the incoming radiation before that it reaches the BHJ. It is therefore of paramount importance that the materials of choice would not give rise to parasitic optical absorption, as it would reduce the amount of photons that would reach the photoactive layer and consequently the available photocurrent. Furthermore, it is highly desired that both the SLs meet this condition. This would be highly relevant in light of future integration of this device in a tandem system, where the transmitted photons would reach the second photoactive element in the optical series. This can be achieved both selecting wide band gap materials or minimizing the thickness, and consequently the absorptance, of the selective layers.

2.3 Catalyst

The last element which concludes the architecture of the HPC is the catalyst layer. Ideally, the material employed should efficiently catalyse the hydrogen evolution reaction:

$$2\,H^+(aq) + 2e^- \rightarrow\ H_2(g)$$

Within the overall water splitting reaction, the cathodic reaction overpotential is only a fraction of the overall operating potential balance (E_{op}):

$$E_{op} = 1.23\,V + \eta_a + \eta_c + \eta_{other}$$

Where η_a, η_c and η_{other} are respectively the anodic, cathodic and additional external overpotentials. As for the cathodic HER, the attention shall be focussed on η_c only. The magnitude of this overpotential is directly connected to the kinetic of the three hydrogen evolution reaction steps:

$Volmer\ Step$	$H^+ + e^- \leftrightarrow H_{ads}$
$Heyrovsky\ Step$	$H_{ads} + (H^+ + e^-) \leftrightarrow H_2$
$Tafel\ Step$	$H_{ads} + H_{ads} \leftrightarrow H_2$

The first step (Volmer Step) is connected to the adsorption of the reactant species (protons in acidic environment or water molecules in neutral/alkaline environment) to the surface of the catalyst which exchanges and electron to yield an adsorbed hydrogen intermediate (H_{ads}). Heyrovsky or Tafel step then lead to the formation of molecular hydrogen when – respectively - a proton coupled electron transfer occurs on the H_{ads} specie or when two H_{ads} species interact. The energy spent for the Volmer step to occur (ΔG_H) represents a first descriptive parameter for the performances of a HER catalyst. The larger and positive this value is, the stronger the interaction between the H_{ads} and the surface. If conversely this value is large but negative, it means that H_{ads} species can be easily removed from the catalyst active site as the H_2 formation steps are favoured. Following the Sabatier principle, the optimal ΔG_H value is a compromise between these two extremes, as it ensures that none of the intermediate steps are limiting the kinetic of the reaction.

2.3.1 Selection Criteria

In several cases the catalyst layer has been employed as a barrier which effectively isolates the underlying materials from the electrolytic solution. This was the case where one of more of the other components were electrochemically unstable, thus preventing the solution to reach them was the only mean to ensure the integrity of the structure. Since the aim of this work is to realize an HPC architecture in which all the employed materials are electrochemically stable, the purpose of this layer will be discussed only from a catalytic point of view, thus neglecting any barrier-effect function.

By contrast, the material of choice should display enhanced catalytic efficiency also when minimum loading is employed. This constraint is fixed in order to ensure that the optical transparency of the device is preserved. A thick catalyst layer would unavoidably block the light propagation. While it may be useful in order to back-reflect the fraction of photons which have not been absorbed by the photoactive layer at the first light pass, it would prevent the integration of the HPC in a tandem cell. Additionally, since high efficiency catalysts often employ platinum group metals (PGM), a lower loading would have a positive impact when envisaging the large-scale deployment of this technology give the high cost of this component.

From an operational point of view, the stability of the device should not be affected by the HER catalyst layer. This is granted by the electrochemical stability of materials such as Pt or RuO_2 based catalyst which are known to perform efficiently in the electrochemical environment with no degradation. Attention must be paid

when it comes to the mechanical adhesion of catalyst to the ESL supporting layer. Due to the intense hydrogen evolution on its surface, the catalyst should be strongly bound to the ESL. If this condition is not met, the mechanical erosion taking place at the electrolyte/catalyst interface may lead to a detachment of this latter element, eventually reducing the overall device efficiency.

While it is true that non-PGM catalyst are currently returning promising results, rivalling the PGM family[61,62], their reaction chemistry and material synthesis is not completely understood yet. Thus, in order to avoid additional degrees of uncertainty on the electrochemical characterization of the HPC, in this work the investigation of the performances will be limited to HPC employing only Pt or RuO_2 as catalyst. Once a solid understanding of the behaviour of the HPC itself will be obtained, it will be meaningful to move forward to integrating high efficiency non-PGM catalyst on these devices.

2.4 Perovskite Solar Cells

While this work mainly revolves around materials and devices for sustainable hydrogen production, several touchpoints with the world of perovskite solar cells are going to be discussed in the following chapters. As an example, in Chapter 3 a fully organic-based tandem system will be presented, in which a high V_{OC} PSC is coupled to a HPC to provide the missing voltage for the water splitting reaction to occur. Also, engineered selective contacts which enabled to obtain moisture resistant PSCs are also going to be discussed in Chapter 5. Given the cross disciplinarity of this work, is therefore useful to provide some tools to understand the world of PSC. Since a detailed description of the physics of these systems is beyond the scope of this work, the discussion will be focussed on the most relevant features and the common traits with the world of OPV and HOPEC-WS.

The main features that determine the high efficiency of solar cells based on this type of materials are tied to its electronic and structural properties. Hybrid organic perovskites have a chemical formula of ABX_3, where A is a cation coordinated to 12 X anions, while the B cation has an octahedral geometry with coordination number 6. This closely packed structure imparts some peculiar properties to its photogenerated carriers. In particular, in iodine-based perovskites photoexcited species can move as free charges due to the relatively low exciton binding energy of the structure (few meV)[63,64]. Furthermore, this allow to obtain long carrier lifetimes e long diffusion length, as photogenerated charges can be easily separated and subsequently extracted prior recombination. These materials also have high extinction coefficients which allow them to absorb a high amount of photons with relatively low thickness. These materials also display an indirect

bandgap which, combined to the suitable exciton binding energy, allow to convert a large fraction of above-band gap photons into free charges. What further contributes to the excellent performance of PSCs is the low non-radiative recombination rate of the photoactive layer and high external radiative recombination efficiency[65]. This translates to V_{OC} values close to the theoretical ones as expected from their bandgap. This is particularly interesting when envisaging the integration of PSCs in tandem systems.

To fully exploit the potential of this promising class of materials, the solar cell architecture underwent several modifications through the years. The very first demonstration of PSCs with substantial PCE employed a mesoscopic adsorbed configuration, in which photoactive perovskite nanocrystals were adsorbed onto a porous scaffold which served also as electron transport material[66]. As years passed, planar architectures have been employed to reach PCE as high as 25.2%[67]. This configuration is similar to the one just described for the HPC and, similarly, for OPV solar cells. Here, a planar photoactive layer is sandwiched between two charge transport layers, one for the holes and one for the electrons (See Figure 6 for an easier comparison). The same requirements mentioned before hold true here, as these layers are fundamental in order to extract efficiently photogenerated charges from the perovskite layer. Indeed, many materials which have found application in OPV (and HPC) as charge transport layers have been successfully employed in PSCs too. To mention a few: TiO_2 as ESL[68], CuI [66], MoO_x[69]

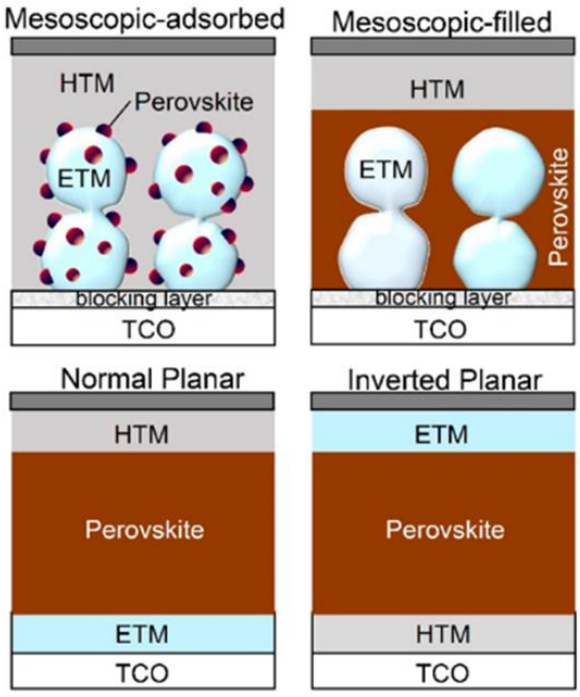

Figure 6: Evolution of the PSC architecture through the years. Starting from the very first examples (Mesoscopic) to the most recent ones (Planar). Ref [66].

as HSL. This further confirms how these fields are closely related, allowing a beneficial "cross-contamination" of expertise and knowledge.

Having adopted a planar architecture further eased the processing of these devices, as this multi-layered structure can be easily achieved through solution processing techniques like spin coating (at a lab scale) or roll-to-roll/screen printing (at further stage of development).

An additional common trait which hybrid-organic perovskites share with organic semiconductors is the ease of tuneability of their optical bandgap. For PSCs, this is achieved through molecular engineering of the ABX_3 structure and in particular acting on the X anion. This element deeply affected the optoelectronic properties of the material as it induces a deformation of the bond length of the lattice. In particular, the band gap is found to increase as the ionic radius of the halide anion decreases. This has been ascribed to an enhanced atomic orbital coupling[70]. Consequently, when the X anion is replaced in a methylammonium lead-X_3 perovskite, the measured band gap increases from 1.58 eV, to 2.28 eV and 2.88 eV when iodine was replaced with bromine and chlorine respectively[71,72]. Also mixed structures have been realized, in which a combination of halides ions lead to a superior band gap tuneability on an almost continuous range[73], as shown in Figure 7.

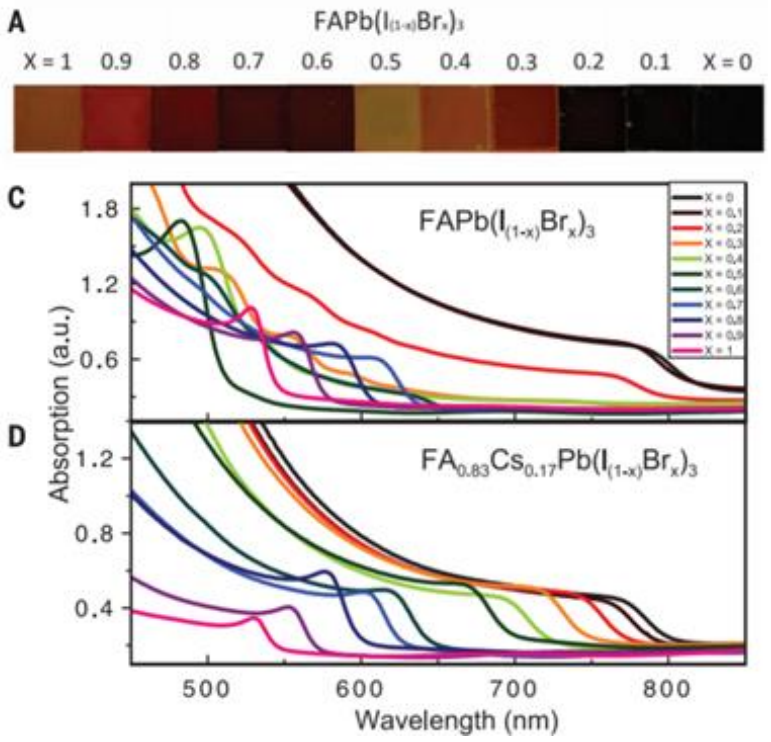

Figure 7: Example of the band-gap tuning achievable for perovskite based photoabsorbers. Acting on its chemical structure, a precise control over the absorption onset can be exerted. Ref [73].

Aside from environmental concerns due to the present of toxic elements such as Pb, the main bottleneck which is preventing PSCs to be deployed on a large scale is their relatively poor environmental stability. The photoactive layer of these devices is prone to suffer heavy degradation when exposed to oxygen and environmental humidity. In particular, as water reaches the perovskite layer, it leads to an irreversible chemical degradation of its structure in which the organic matrix is deprotonated and leads to the release of toxic by-products. The overall effect leads to a complete disruption of the crystal symmetry of the materials which degrades its optoelectronic properties. Several strategies are currently being investigated in order to solve or at least mitigate this issue. They range from functional molecules which impart hydroscopic character to the surface of the material to encapsulation methods which completely isolate the cell from the environment. As it will be seen later on this work, novel intriguing opportunities can arise from the combined effort of the world of HOPEC-WS and PSCs, allowing to design an efficient stabilization strategy which imparts moisture resistance to the cell through engineered charge transport materials[74].

Chapter 3
HPC-PSC Tandem

3.1 Introduction

In the framework of identifying suitable technological approaches to exploit renewables and store them by means of viable energy vectors, systems which couple photoelectrodes and an external biasing source are those which return the most promising results. As discussed in the introduction, many examples employing inorganic photoelectrodes already exist in literature.

These systems rely on technologies which are already extensively studied and which are often already commercially available. This is particularly true when it comes to inorganic solar cells, such as Si-based ones, which are typically the device of choice for PEC-PV tandem cells. Within this context, systems employing multiple PV-biasing elements are often employed. This, together with the high intrinsic cost of the raw materials, the low defect tolerance and the energy intensive fabrication process tend to increase the final cost of produced hydrogen making these system less appealing for a large scale deployment[37–39]. On the other hand, the efficiency of organic based photovoltaic and perovskite solar cells is steadily increasing and several technoeconomic analysis pointed out that for large scale production capability the production cost (€/m^2) could be in the order of 7 €/m^2 [75] and 27 €/m^2 [76] for OPV and PSC respectively. In addition, both HPC and OPV/PSC modules in principle share the same manufacturing processes thus easing the realization of integrated modules. Furthermore, thanks to their high V_{OC}, PSC could allow to minimize the number of components providing more than 1 V of bias to the reaction from one single photoactive element.

For these reasons and thanks to their superior performances and flexibility in terms of molecular engineering, PSC are an excellent candidate to realize the very first demonstration of an organic-based tandem device when coupled with high performing HPC.

Thus, herein the advancements made in realizing fully organic-based tandem devices will be discussed, with the final aim of developing systems capable of closing the cost-efficiency gap of produced hydrogen.

From a methodological point of view, the following work assesses of technological maturity of this organic based PEC-PV system. The technological concept will be discussed and presented for tandem PEC/PV systems. In this chapter will firstly be addressed the proof of the technological concept on a laboratory scale. This will involve the study and characterization of the individual components, their dedicated optimization and the development of an analytical model to rationalize their performances in a proof-of-concept working system. Once this framework is set, the technology validation will be presented and discussed with an eye to the potential future development.

The content of the following chapter can also be found in the recently published paper[77].

3.2 HPC-PSC Tandem overview

The three building blocks of this system are two photoactive elements and an electrocatalyst. This three-element tandem is schematically depicted in Figure 8, in which the illumination direction and the interconnection between the elements is shown. The hydrogen evolving hybrid organic photocathode, which working principle and functional design rules have been presented in Chapter 2, is herein coupled with a methylammonium lead iodide (MAPI) perovskite solar cell and a

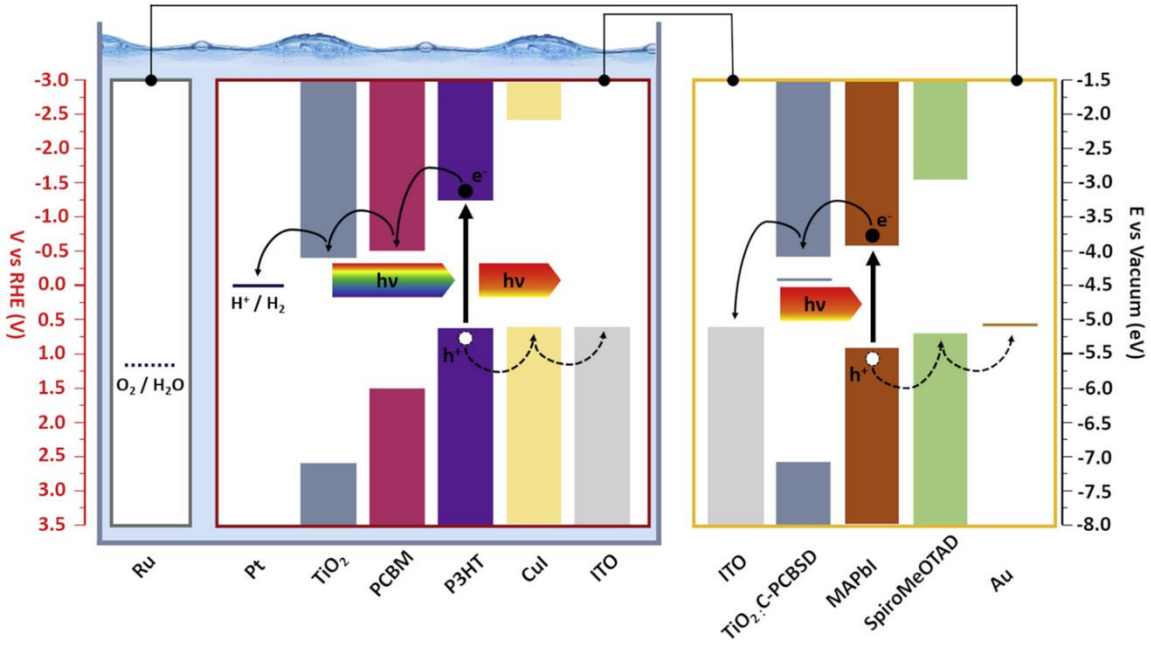

Figure 8: Schematic description of the three-element tandem. The Ru OER catalyst and the HPC are immersed in the electrochemical cell while the PSC is placed in close proximity. This figure provides also an indication of the energetic structure of the system and the charge transfer steps occurring across the multi-layered devices.

Ru-based OER catalyst. The integration of the first two elements is performed with an eye on the overall tandem working principle, which details have been discussed in Section 1.2.4.

As the topic of this work is the realization of an efficient HPC, here will be briefly recalled the most relevant aspects which have led to the optimization of this specific element for this application. The PSC, on the other hand, did not undergo any tailored optimization and was used *as-is* from the work of Tao et al.[68]. The first, crucial point, which must be addressed while realizing a tandem system in which the photoactive elements are optically in series is, indeed, the transparency of at least one of the two devices. This calls to focus both on the absorption profile of the photoabsorber itself and on the additional contributions coming from the adjacent layers.

Furthermore, to enhance the performance of the whole system, each element needs to provide the highest possible photovoltage and a high photocurrent density, ideally with a steep increase as close as possible to the open circuit potential. This concept, in the field PV, is expressed through the fill-factor of the solar cell[74]. For HPC, its counterpart is the ratiometric power saved[78] (φ_{Saved}) which definition is provided in Section VII.I of the Appendix. Overall, this parameter is highly sensitive to the performances of the charge extracting layers, as they ultimately determine the charge collection efficiency of the full device. Provided that the HPC can be optimized in this fashion, its coupling with the PSC should return enough photovoltage to overcome the potential requirement for the overall water splitting reaction to occur when the two elements are connected with OER catalyst. The OER catalyst will also be presented, and its performances discussed, as they ultimately contribute to the balance of overpotential requested.

The tools summarized so far are meant to provide an overview of the process which will bring us from the benchmark architecture realized by Comas et al.[40] to the new, improved HPC and its integration within the tandem stack. These concepts will be recalled and specifically discussed whenever the discussion will prompt them.

3.3 HPC Tandem Oriented Optimization

The HPC architecture, schematically depicted in Figure 8, comprises 4 components: a Copper Iodide HSL, a P3HT:PCBM BHJ, a TiO_2 ESL and a Pt catalyst layer. While the materials employed will remain unchanged with respect to the previously published results, a systematic optimization will be performed on each of them.

The first crucial point will be to minimize undesired photon losses due to parasitic reflections/absorptions. These could arise mainly from the Pt metallic layer and, eventually, from the TiO_2 nanostructured ESL onto which the catalyst is deposited. The catalyst layer of the benchmark architecture was developed to serve solely the purpose of catalysing efficiently the HER. Additionally, the high reflectivity of Pt allowed further to collect additional photons which at the first pass had not been absorbed by the BHJ. For this specific application, however, this would dramatically reduce the amount of radiation reaching the second element in the optical series, i.e. - the perovskite solar cell.

To this extent, a parametric optimization was performed aimed at identifying the minimum Pt loading which allowed to retain the catalytic performances of the device. Adjusting the amount of deposited Platinum required to tune the deposition process. The technique employed to deposit the thin catalyst layer was p-DC magnetron sputtering. Thus, once a suitable calibration curve was obtained, multiple HPCs were realized in which the deposition time was set to obtain a target thickness of 16, 8 and 4 nm.

On par, the TiO_2 ESL which also worked as catalyst support has been optimized to maximize the available surface area. Nanostructuration of this layer has been achieved through Pulsed Laser Deposition (PLD). The main parameters involved are the background gas pressure and the laser pulse energy. Increasing the surface area required to work toward a less dense structure. This can be achieved by increasing the background gas pressure and/or reducing the laser pulse energy, as they determine the kinetic energy of the species which from the gas phase condense on the target. The higher the pressure, the higher the amount of kinetic energy transfer events between the nanoclusters emitted from the target and the gas molecules. A transition regime can be identified in which the deposited film grows in nano-trees like structures with an intermediate porosity between a compact film (achieved at low pressure) and an aerogel (achieved at high pressure). Furthermore, this peculiar structure exhibits a highly directional growth perpendicular to the substrate, which favours charge transfer from the adjacent layers i.e. – from the BHJ to the catalyst.

To provide a comparison between the starting condition and the optimized one, the process parameters have been summarized in Table 1. The newly achieved TiO_2 layer is shown in Figure 9, where the effect of the nanostructuration can be appreciated through the high density of nanoclusters on the surface of the film which efficiently work as binding sites for the subsequently deposited Pt species.

Table 1: Comparison of the TiO_2 deposition parameters for the benchmark [Comas et al] and optimized HPC architectures.

Deposition Parameter	**Comas et al.**	**Optimized**
Thickness [nm]	100	100
Background Gas	Ar/H_2 3.1% mol	Ar/H_2 3.1% mol
Background Gas Pressure [Pa]	15	45
Pulse Energy [mJ]	400	300
Repetitio Rate [Hz]	20	20
Fluence [J cm^{-2}]	2.5	2

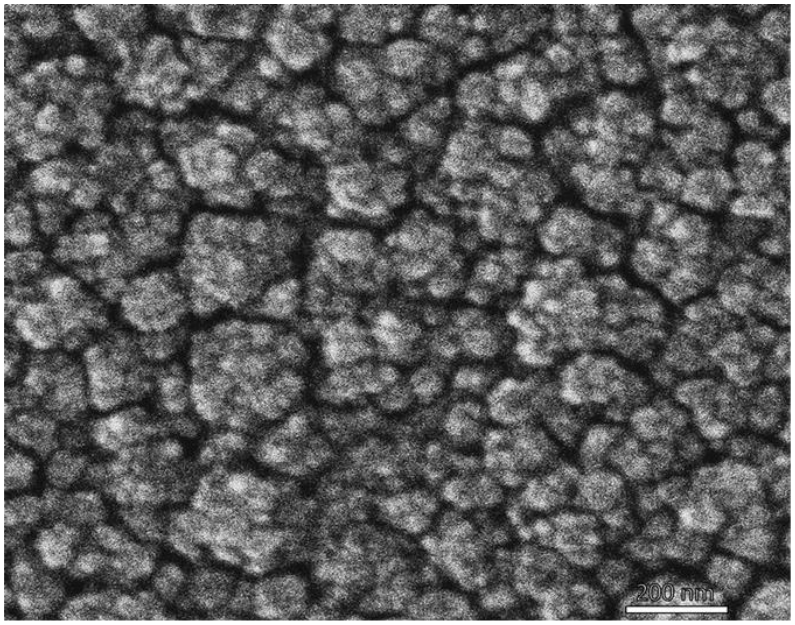

Figure 9: SEM image of the surface of the optimized TiO_2 displaying the features of the nanostructuration.

The result of this optimization step can be appreciated from the polarization curve shown in Figure 10.a, in which each curve represents the average behaviour of a set of HPCs with different thickness of deposited Pt. Remarkably, the low loading condition (4nm nominal Pt thickness) exhibits the best performances even when compared to the highest tested loading (16 nm). This is true both in terms of current density at 0 V_{RHE} and steepness of the curve, in which the photocurrent profile is anticipated of around 30 mV in the region between 0.5 and 0.25 V_{RHE}. This has a twofold relevance, as it demonstrates that the catalytic efficiency of this layer is not tied to the amount of deposited platinum but rather on the surface coverage on top of the nanostructured scaffold. Thus, a lower amount of catalyst enables to fully exploit the high active area of the surface which on the other hand results to be flattened beyond a certain thickness threshold.

To further address the optical absorption of the HPC, it is meaningful to investigate the contribution arising from the organic bulk heterojunction which in this case

consists of a blend of P3HT:PCBM. Provided that this layer is the one responsible of harvesting photons and photogenerating electron-hole pairs, a careful optimization of the components is mandatory. As discussed, the BHJ is realized upon blending a donor polymer and an electron acceptor. The first being responsible of the photogeneration process, while the latter is added with the aim of enhancing the exciton dissociation efficiency prior recombination within the BHJ itself. The relative ratio between the donor and acceptor components has to be balanced so that the resulting interconnected network consists of a matrix with finely interspersed domains of donor and acceptor material respectively. The average exciton diffusion length in organic BHJ is in the order of tens of nanometres. This ultimately affects also the final thickness of the BHJ itself. Indeed, an excessively thick BHJ may lead to lose a fraction of photogenerated charges which happen to be in a fraction of volume too far away from the selective contact interfaces. The spin coating protocol has been thus modified, reducing the final thickness to 160 +- 10 nm (vs 200 nm of the starting architecture).

As from the OPV literature, an higher amount of donor material with respect to the acceptor allowed to increase the overall device performances[79]. Thus, an investigation to discover if similar results could be achieved also on the current HPC was set up. The benchmark architecture employed a 1:1 ratio of D:A materials. It has been found that by reducing the ratio to 1:0.7 the overall

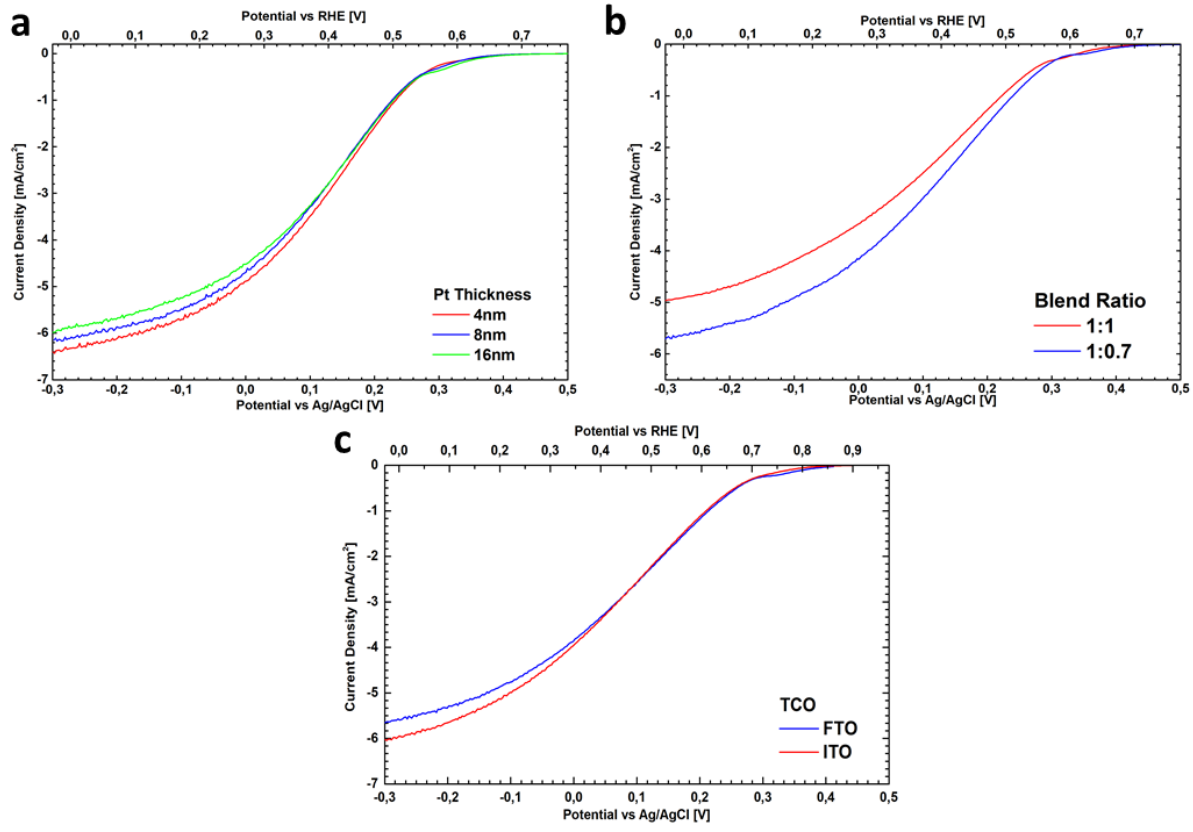

Figure 10: Polarization curves from V_{OC} to 0 V_{RHE} representative of the HPCs optimization blocks. Panel a) Pt thickness optimization; panel b) Blend ratio optimization and panel c) TCO optimization.

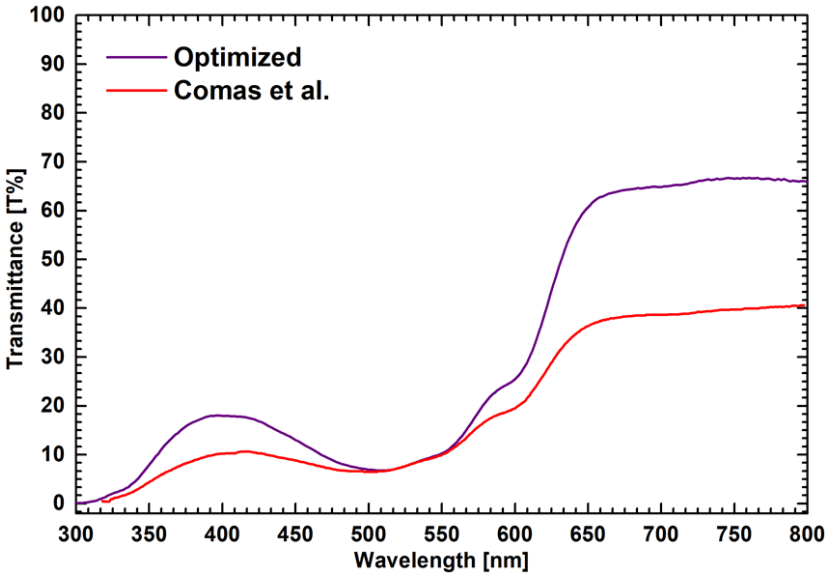

Figure 11: Transmittance spectra of the reference and optimized HPCs. The increased transmittance of the optimized architecture (purple line) can be easily appreciated.

performances of the device improved, as shown in Figure 10.b. Indeed, the polarization curve of photocathodes employing the optimized BHJ formulation allowed to achieve better performances with respect to the initial one.

An additional slight improvement has been achieved replacing the F:SnO_2 TCO with an In:SnO_2. The lower in plane resistance of the latter (15 Ω/sq vs 10 Ω/sq) allowed to slightly increase the saturation current density at 0 V_{RHE} (Figure 10.c). Similarly, by processing the CuI HSL in N_2 atmosphere glovebox, it was possible to obtain a more homogeneous surface coverage with reduced intra-batch variability. This issue was reported due to the high RH sensitivity of the spin coating step of CuI, which often resulted in island-like domains which failed to completely cover the TCO surface, leading to a lower shunt resistance and increased charge carrier recombination probability.

Overall, this target optimization succeeded in reaching the desired results. Firstly, the tandem-optimized architecture allowed to sensitively increase the fraction of transmitted light which falls outside of the absorption profile of the BHJ. As depicted in Figure 11, in both the architectures the absorption peak of P3HT (centred at 520 nm) in highly pronounced and almost coincident. The reduced amount of PCBM in the optimized device is responsible of the increased transmittance between 320 and 500 nm, as it coincides with its excitonic absorption peak. On the other hand, the remarkable transmittance increases in the region between 600nm – 800 nm is directly correlated to the reduction of the amount of Pt, as less light is reflected from this layer. Thus, from the point of view of the optical coupling, this newly design architecture greatly fits for the integration in a tandem system.

For what concerns the photoelectrochemical performances, the most interesting outcome is to be found in the improved charge extraction as a result of the optimization of the charge selective contacts. This, as the polarization curve of the benchmark and optimized architecture shows (Figure 12.a), is reflected in the anticipated and steeper photocurrent onset in the potential region closer to the V_{OC}. This is a direct indication of the fact that photogenerated charge carriers experience a lower resistance while flowing throughout the multi-layered architecture. Furthermore, the increase in magnitude of the photocurrent points out to a more efficient photogeneration and lower recombination of charge carriers within the BHJ, as expected from its formulation optimization.

To give some key figure, it is worth to compare the ratiometric power saved of the initial and final condition and their MPP. The current density and potential at the maximum power point is 3.98 mA/cm^2 – 0.303 V_{RHE} and 4.6 mA/cm^2 – 0.33 V_{RHE} respectively. This (assuming the faradaic efficiency to be 100%) translates to an increase in φ_{saved} from 1.21% to 1.51% (Figure 12.b). Even more interestingly, the anodic shift of the MPP is of paramount importance when considering the integration of this HPC in the tandem system with the PSC, as it further reduces the overall photovoltage contribution required for the whole water splitting reaction to occur.

3.4 HPC - PSC Preliminary Assessment

Provided that the optimized HPC displayed improved photoelectrochemical performances and increased optical transparency, the following step prior assembly of the three-element tandem cell is to evaluate the coupling of the two photoactive elements. This requires measuring from an optical point of view the

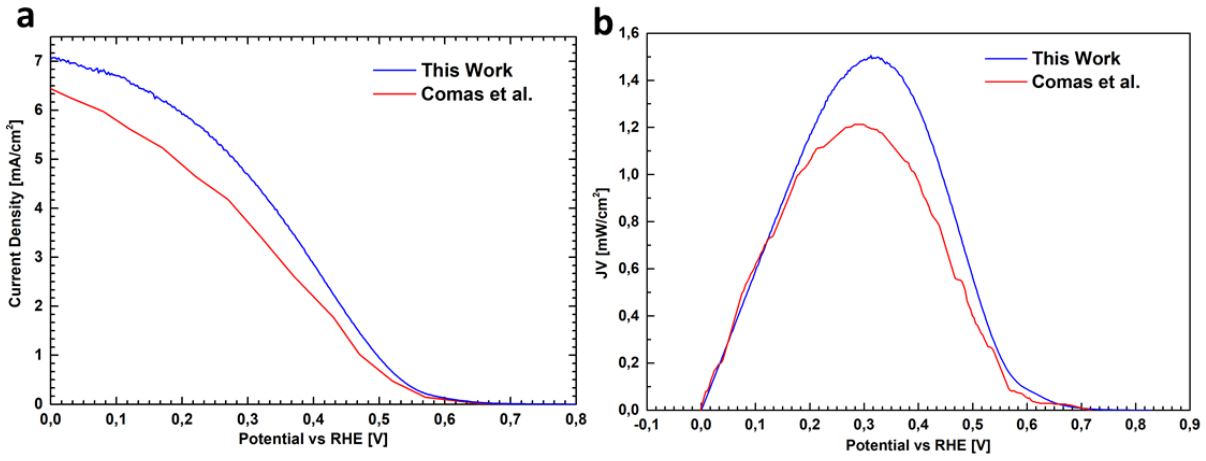

Figure 12: Polarization curves (a) and ratiometric power saved (b) of the reference and optimized HPCs. Please note: the sign of current density in panel (a) has been reversed for an easier comparison with panel (b).

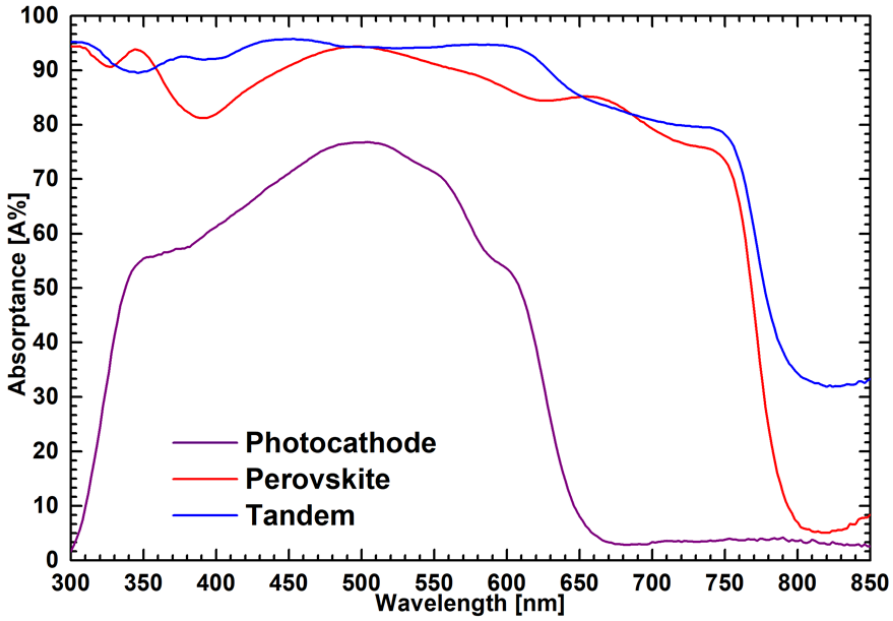

Figure 13: Absorptance spectra of the HPC and PSC in a stand alone configuration (Purple and Red curves) and assembled in the Tandem stack (blue line).

absorption profile of the two combined devices. Additionally, it will be necessary to assess the performances of the PSC under full and attenuated light intensity, the latter corresponding to the condition in which the HPC shadowing effect reduces the amount of photons which can be converted by the PSC.

Transmittance and reflectance data have been collected for each device separately and for the tandem configuration. Absorptance was calculated as $Abs = 100 - T_{Meas} - R_{Meas}$, being T_{Meas} and R_{Meas} the measured values of total transmittance and total reflectance respectively. This allows to have a clear picture of the effective photon absorption of each device, thus giving a direct indication of the spectral coverage of the photoactive layers both in the separate devices and upon coupling.

The spectra in Figure 13 show the individual contribution of the HPC and PSC (purple and red line respectively) and of their optical coupling (blue line). The sharp optical absorption edge of the MAPI perovskite at 800 nm is consistent with the literature data[80,81], allowing to estimate an optical bandgap of 1.55 eV. This further highlights the relevance of the previous optimization performed on the HPC. Indeed, the wavelength range between 800 nm and 650 nm would not have been accessible to the PSC otherwise, thus hindering the performances of the full tandem. On the HPC side, the P3HT:PCBM absorption band turns out to be the only appreciable contribution. Outside of this region of interest, less of 10% of the incoming photons are absorbed. Upon coupling, the HPC-PSC stack exhibits and extended absorption range which covers the entire visible spectrum, as desired for a dual absorber tandem system.

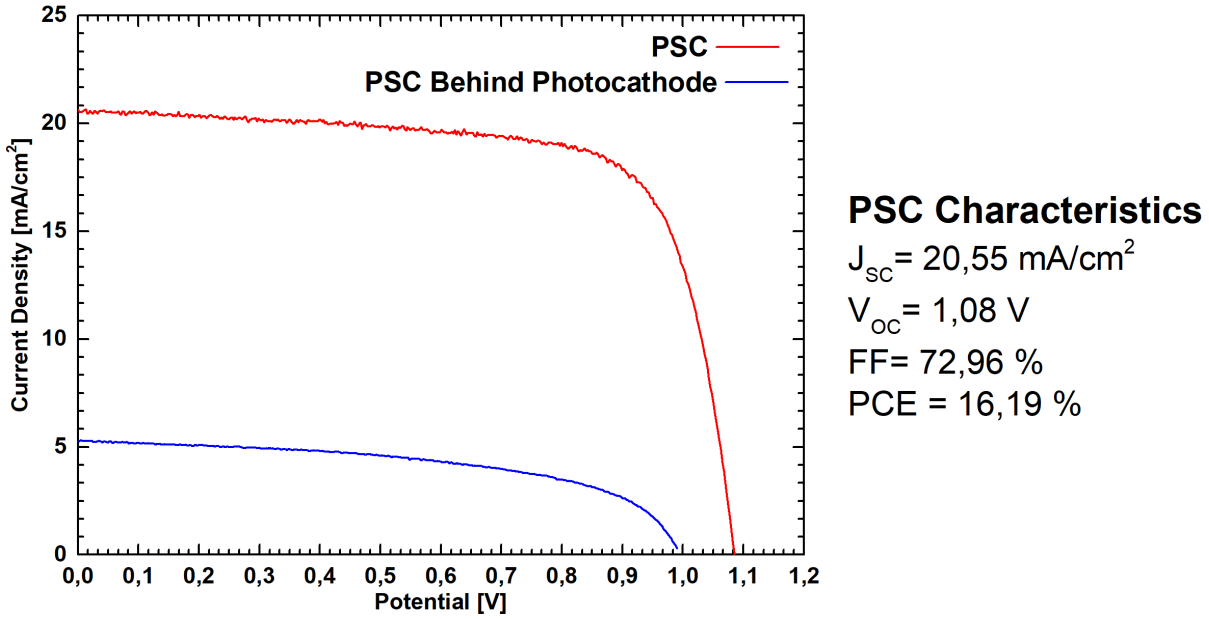

Figure 14: J-V curves of the PSC with full light (red line) and under the shadowing effect of the HPC (blue line). The PSC parameters reported aside refer to the full light J-V characteristic.

Given the partial absorption spectra overlap of the two photoactive layers, the current-voltage output of the Perovskite cell, being the second element in optical series, is expected to be curtailed. This is a common phenomenon which happens frequently when coupling two devices in a tandem configuration. To evaluate the extent of this effect, the PSC output has been characterized both under full light and under the shadowing effect of the photocathode. Furthermore, the electrochemical cell and the electrolyte have also been placed along the light path. This allowed to take into account additional photon losses which may arise from parasitic reflections occurring while light propagates in the full-tandem system.

In Figure 14 the PSC solar cell characteristics are shown for the aforementioned conditions. Under full light, the cell delivers an open circuit potential of 1.08 V and a short circuit current density of 20.55 mA/cm^2 with a Fill Factor of 72.96%. The effect of the attenuated light intensity and partial reduction of photons available in the range of wavelength between 650 nm and 350 nm is shown on the blue curve of the graph. As expected from literature[82], the dependence of the V_{OC} and J_{SC} on light intensity follows different trends. J_{SC} decreases linearly with the light intensity (20.55 mA/cm^2 vs 5.5 mA/cm^2). V_{OC} on the other hand has a logarithmic dependence and therefore suffers less the shadowing effect (1.08 V vs 0.98 V).

From the perspective of integrating this device in a tandem system, the relevance of retaining a high open circuit potential counterbalances the severe current density reduction. Indeed, a high photovoltage contribution is fundamental in order to overcome the potential requirement to allow water splitting to occur. If the potential of the two photoactive elements combined (i.e., the HPC and the PSC) is

not sufficient, the water splitting reaction would not occur, irrespective of their delivered current density.

3.5 Ru-Based OER catalyst

The third and final element which participates to the hybrid-organic based tandem system is the anodic electrocatalyst responsible of promoting the oxygen evolution reaction. The material selection of this electrode has been carried out so that it could guarantee the highest possible efficiency, not limiting the performance of the overall tandem stack.

Catalytic materials which are used for this purpose are often engineered to work at neutral or basic pH, that is the condition in which the OER kinetic is favoured. Provided that this tandem system will work at acidic pH, the most promising candidates were ruthenium or iridium. Electrodeposition of a nanostructured Ru catalyst has been performed starting from known literature[83], which details are reported in Section II of the Appendix.

The SEM image of the electrocatalyst optimized for this application is shown in Figure 15. The obtained morphology is a direct result of the templating effect performed by the hydrogen bubbles which evolve on the surface of the substrate

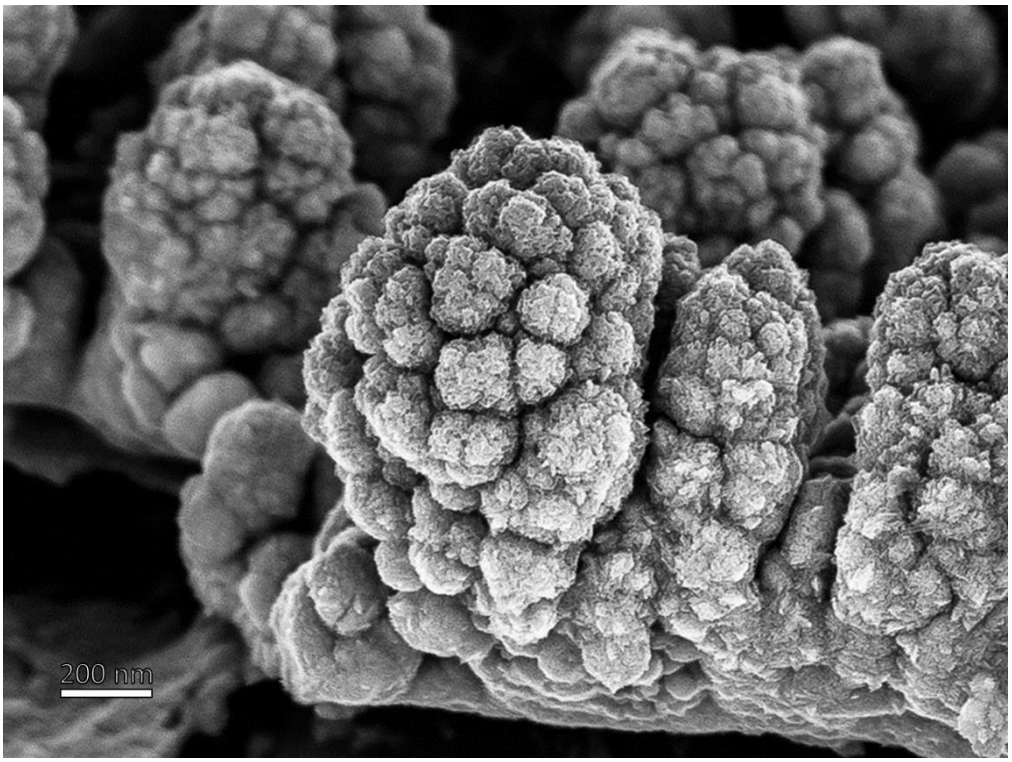

Figure 15: SEM micrograph of the nanostructured Ru OER catalyst. The raspberry-like morphology is obtained thanks to the dynamic templating effect of H_2 bubbles during the electrodeposition.

during the electrodeposition process. During this step, which is performed at highly cathodic potentials (-5 V_{RHE}), Ru-deposition is indeed a concomitant process which occurs with low faradaic efficiency as compared with the HER. This combined effect allows to achieve a nanostructured film with tree-like dendritic branches with high surface area and an estimated roughness factor of 340[83].

To probe the structure of this catalyst, XRD data have been collected and compared with the known reference peaks of metallic ruthenium (Figure 16), confirming that the film does not undergo oxidation when removed from the electrolytic environment and retains its metallic form. Peaks other than Ru match those of metallic titanium, which signal comes from the underlying substrate. The average crystalline domain size, as measured from Scherrer analysis, is in the order of 6 nm.

The catalytic performances of the OER catalyst are on par of the best reported in literature[84], as demonstrated by its low overpotential η_{10} of 255 mV and Tafel slope of 48.3 mV/dec (Figure 17.a). This low overpotential plays a fundamental role when integrating this electrode in the tandem stack, as it further narrows the potential required to perform the water splitting reaction by minimizing the potential barrier for the OER at the lowest attainable values.

To further confirm that this material does not introduce unforeseen electrochemical instability issues to the assembly, its stability was assessed evaluating the overpotential drift over a window of time of 1 hour (Figure 17.b). This allows to rule out that the catalyst itself does not degrade in the electrolytic environment,

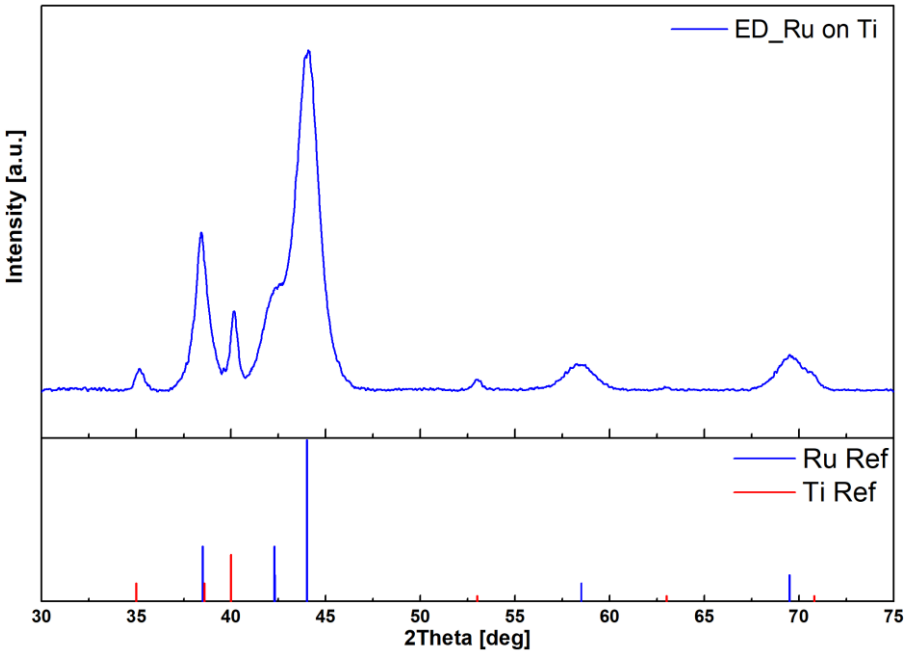

Figure 16: Grazing Incidence X-Ray Diffraction of the electrodeposited Ru on Ti sheet (upper panel) compared with the reference peaks for crystalline Ru and Ti (lower panel).

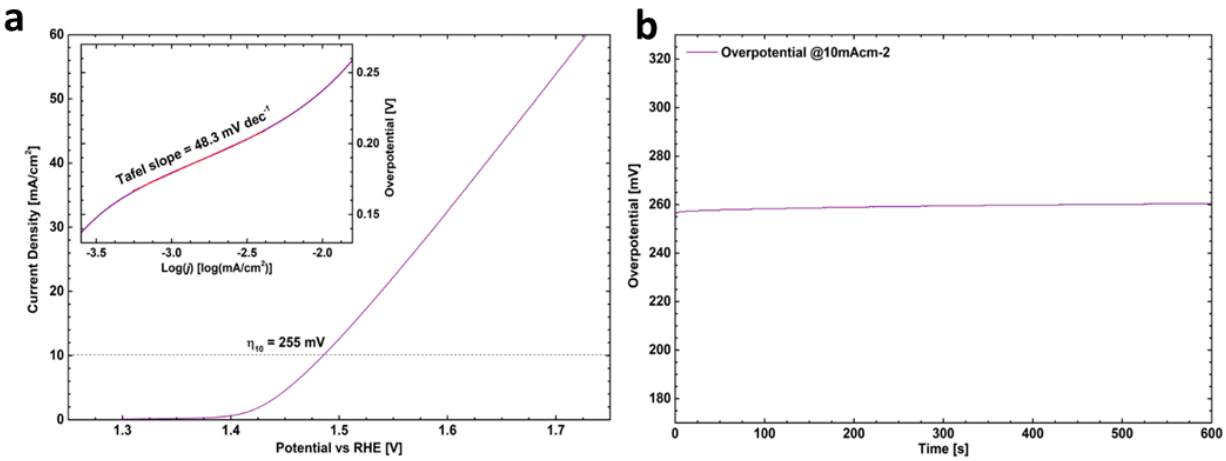

Figure 17: Polarization curve (a) and Tafel slope (a.inset) of the Ru OER catalyst. Overpotential as a function of time (panel b) at a fixed current density of 10 mA/cm^2.

as reported in literature for metallic Ru catalyst[85]. The catalyst instability is indeed connected to metal leaching which takes place during extended OER measurements, which often leads to opt in favour of the more stable but less performing ruthenium oxide. Nevertheless, the chronopotentiometry shown in Figure 17.b highlights that the stability of this electrode in the selected time frame is close to 100%, with a potential drift of only 5 mV during the initial minutes of the measurements.

This ensures that the anodic electrocatalyst operates at steady state when placed in the tandem system. Thus, any time dependent phenomenon recorded shall be investigated focusing only on the other two elements.

3.6 HPC-PSC Tandem Characterization

Once the components that will build the tandem stack have been presented in their stand-alone configuration, it will be now discussed how they blend together when connected in the three-element system. This will address the practical description of the home-made set up itself, the depiction of the working principle from the charge flow point of view and the analysis of the electrochemical behaviour of the stack. From this analysis the most promising outcomes of this new approach will be retrieved, highlight the efficiency-limiting factors and use this information to shed light to the path which could allow these systems to reach higher solar-to-hydrogen efficiency, targeting the highly anticipated 10% and picturing the long-term scenario with an eye on the latest development of the akin field of OPV.

3.6.1 Set up and interconnection description

To perform the photoelectrochemical characterization of the three-element tandem, a custom set up has been realized which allowed a precise alignment of the photoactive elements.

The already existing photoelectrochemical characterization test bench consists of a potentiostat, a solar simulator and the electrochemical cell, which details are provided in the Appendix. To control the alignment of the photoactive elements, two additional stages have been introduced. The first one is a stage which allowed to adjust the height of the HPC and the electrochemical cell with respect to the light source. The second one was a manually controlled x-y-z micrometric stage onto which the PSC has been mounted by means of a 3D-printed support. This fine adjustment was necessary to properly align the active area of the photoactive elements, as the light propagation was allowed only through the aperture of the vinyl mask applied on the photocathode. To record the photocurrent proportional to the water splitting reaction, the three elements have been connected to the potentiostat setting the OER catalyst as working electrode and the HPC-PSC connected in series as counter electrode.

As for the photoactive elements, the P3HT:PCBM BHJ and the MAPI perovskite are the layers where photogeneration takes place. In the HPC, photogenerated electrons, which already possess enough potential energy to drive the HER reaction, are extracted through the TiO_2 electron selective layer and, once reached the Pt layer, reduce protons to H_2 molecules. Photogenerated holes on the other hand are extracted via the CuI hole selective layer and, once extracted via the ITO back contact. In the PSC, similar charge transfer process occurs. Photogenerated electrons in the MAPI layer are here extracted through the TiO_2 C-PCBSD layer and then reach the HPC, while holes extracted through the SpiroMeOTAD layer and Au back contact pass first trough the potentiostat and then reach the OER catalyst. At the interface with the electrolyte, OER occurs on the Ru surface.

Photogenerated holes which from the HPC flow to the PSC do not have enough energy to drive the OER. However, once these charge carriers reach the PSC, its photovoltage adds up to their initial one allowing them to gain the missing potential, overcoming the barrier and biasing the water splitting reaction. Since the PSC role is to provide this additional driving force, it is not necessary for the valence band of the photoactive layer to lie below the oxygen evolution potential.

3.6.2 Artificial Leaf – HPC|PSC Tandem

Once the separate components and the tandem working principle have been discussed, the experimental performances of the stack have been investigated. As a first step, the coupling of the (photo)electrochemical characteristic of the elements will be commented. This will allow to have an estimate of the expected efficiency of the stack prior recording its actual current-voltage response. Figure 18.a reports the polarization curves of the HPC (green line), the PSC (magenta line) and the OER catalyst (purple line).

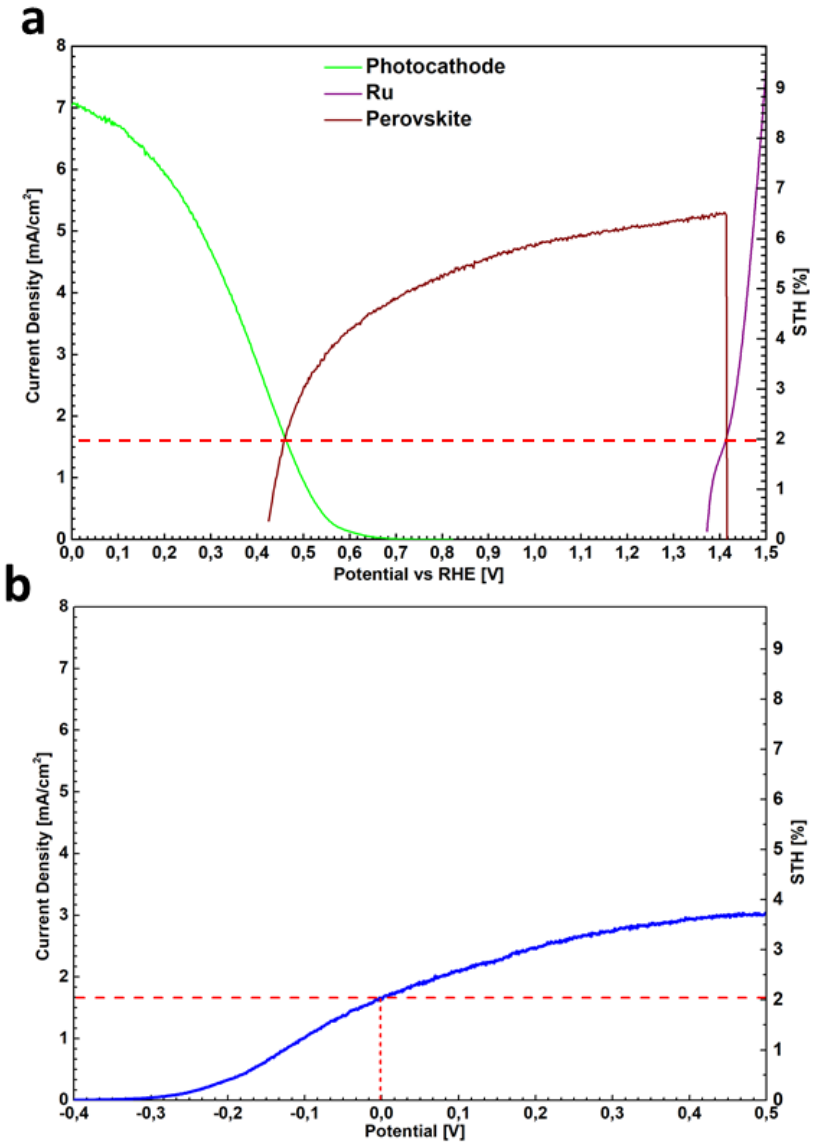

Figure 18: (a) Curve matching of the polarization curves of three components acquired in a stand-alone configuration. The red line identifies the expected matching point of the three elements, the operating current density (left Y-axis) and the corresponding expected STH (right Y-axis). (b) Polarization curve of the three-element tandem. The point at 0 V identifies the condition of unbiased operation and the corresponding STH (right Y-axis).

The onset potential for the HPC (0.72 V_{RHE}) determines the extent of the anodic shift of the HER onset arising from the photovoltage provided by this device. On the anodic side, the OER electrocatalyst starts to bias the reaction at 1.38 V_{RHE}. The voltage gap between these two elements is expected to be around 0.66 V. The external PV bias, taking into account the shadowing effect, should deliver *circa* 1 V, thus almost 0.3 V more than the minimum requirement. This additional bias allows to "match" (as depicted in Figure 18.a) the two electrochemical devices where the water splitting half reactions occur, identifying a point in this potential region where the current density of each of the three elements are equal. This point corresponds, indeed, to the situation when the tree elements perform the water splitting reaction relying only on photovoltage contribution of the photoactive elements (no external applied bias). This current-matched condition is indeed imposed by the fact that the three elements are electrically in series. Thus, the current circulating in the system must be equal across all the devices and it is determined by the lower value of current provided by one of the elements.

The expected matching point identified in this condition (red dotted line in Figure 18.a) corresponds to a current density of 1.6 mA/cm^2, which translates to 1.97% STH efficiency. In order not to over/underestimate this value, a conservative approach has been adopted. For this reason, the characteristic curves employed to estimate the matching point have been chosen to be representative of the average behaviour of the components.

To validate this analysis, the three-element tandem system has been assembled and characterized. In Figure 18.b, the polarization curve measured on the full stack is reported. This behaviour reflects the overlap of the J-V characteristics of the separate components. Its potential dependence is therefore a result of how the electrical working point of the stack modifies as a function of the applied voltage. At negative applied potential, the photocurrent density decreases as a result of the lower available voltage. That visually corresponds to "pulling away" from each other the individual polarization curves of the electrochemical devices shown in Figure 18.a. By contrast, at positive applied potential the additional voltage raises the current density matching point as the polarization curve are drawn closer.

Where no additional bias is provided to the system, identified by the red dotted line on the graph, it corresponds to the un-biased performance of the stack. Here, the measured current density value, proportional to the water splitting reaction, is 1.65 mA/cm^2, which is in close agreement with the conservative estimate just described. Provided that the Faradaic Efficiency of the photocathode has already been measured[40] (FE=100%), assuming this value to be consistent for this system as well. Under this assumption, the STH of this HPC-PSC tandem is 2.03%. To date, this is the very first demonstration of a working tandem system which achieves substantial water splitting relying on organic based devices. Furthermore,

given the high photovoltage contribution of the PSC, it was possible to keep the number of photoactive elements to the lowest possible number. By contrast, systems employing inorganic photoelectrodes or PV-biasing cells often employ 3 or more devices. The consequent increase in achievable STH is, however, more related to how the tandem is built rather than to the performances of the individual components.

Under un-biased condition, the photocurrent density has been recorded to get insight on the time-dependent phenomena occurring on the stack. The chronoamperometry is shown in Figure 19.a. Two distinct regions, characterized by different dynamics, can be identified. For short times, the photocurrent undergoes an abrupt decrease. This is addressed to the formation of bubbles which fail to release from the catalyst surface (both anodic and cathodic) hence reducing the effective active in contact with the electrolyte. This effect is also enhanced by a shift in the working point of the tandem stack, which modifies the matching current density of the elements.

To gain further insight on this latter phenomenon, the analysis will focus on the HPC time-dependent behaviour. This because the PSC is not expected to suffer such sharp decrease in efficiency in this window of time[68] and the OER has been proven to stable in the dedicated section. Since the effect shown on the tandem stack is expected to be highly potential-dependent, the photocurrent of the HPC alone at two different conditions has been recorded. The first corresponds to the voltage expressed in V_{RHE} where the matching point of the tandem is expected to take place. It is labelled as Tandem Working Point (TWP) and it is equal to 0,45 V_{RHE}. The second one is the maximum power point (MPP) of the photocathode itself, as identified in the dedicated section, being equal to 0,33 V_{RHE}. The photocurrents corresponding to these two conditions are plotted in Figure 19.b alongside with the chronoamperometry of the full tandem stack.

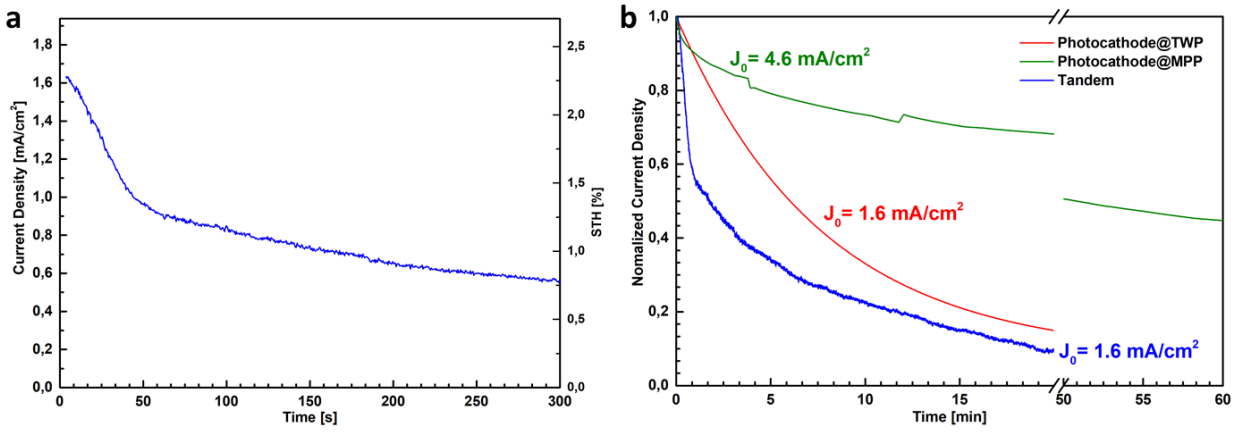

Figure 19: (a) chronoamperometry of the tandem under unbiased condition. (b) Comparison of the tandem time-dependent photocurrent decrease with the behaviour of the HPC alone polarized at its V_{MPP} (green curve) and at the V_{TWP} (red curve). The initial value of current density for each condition is reported as J_0 following the same colour coding of the curves.

From the direct comparison, it can be seen that the time dynamic of the tandem and that of the photocathode operated at the TWP fall in the same range. Indeed, after 10 minutes the HPC polarized at its MPP retains 73% of its initial photocurrent value while at the TWP this value drops to the 33%, close to the one of the tandem. It is therefore meaningful to infer that they are correlated by the same phenomenon. Taking under consideration the polarization curve of the photocathode alone, the TWP lies in a potential region closer to the open circuit potential where a substantial amount of photogenerated charges is not extracted and undergo recombination. Several works form the field of OPV investigated in detail degradation phenomena occurring within the BHJ[86–89]. Their findings highlighted that charge accumulation which takes place close to the open circuit potential condition leads to an increase in bimolecular recombination and trap-induced losses in the BHJ amorphous mixed phase are more pronounced. This ultimately leads to a fill factor reduction and accelerated degradation of the solar cell.

By contrast, the performance of the HPC operated at its maximum power point exhibits a much slower time decay. Under this applied potential, minimal charge accumulation is expected to take place, thus the performance loss has to be addressed to a different phenomenon. This can be explained on the intrinsic electrochemical instability of the CuI hole selective layer. As the electrolyte diffuses through the layers, it slowly starts to dissociate the HSL into Cu^{2+} and I^- ions.

Nevertheless, this insight offers an intriguing point of view on the potential development of HPC-PSC tandem. This reflects both on the perspective increase in efficiency and extended operational stability. Indeed, if the TWP were to coincide with the MPP of the hybrid photocathode, the overall system would benefit simultaneously from an increase in operating current density (from 1.65 mA/cm^2 to 4.6 mA/cm^2) and, provided that no unforeseen degradation phenomena shall arise, and a suppression of the abrupt voltage loss which, at the current state, causes the severe photocurrent decrease at the very beginning of the measurement. Particularly, this increase in operating current density would lead to a forecasted STH efficiency of 5.67%, a three-fold increase with respect to the current value.

To give a qualitative estimate of how far this situation is from the current scenario, it is meaningful to consider the expected operating potential which should be delivered to match the MPP of the HPC. The difference between the two condition is of only 120 mV. This opens up to the possibility of shaping the future optimization of these architectures, with particular emphasis on the HPC, with a focus on closing this potential gap. Therefore, taking this result as starting point, a model which could describe the actual scenario will be defined, identifying the

most sensitive parameters which affect the performances of each element and forecast how and where to act in order to improve the performances of this system.

3.7 Perspective for Tandem Optimization - Introduction

The discussion on the future improvements achievable with hybrid-organic PEC-PV systems, which employ devices similar to the ones presented, will lie its foundation on extensive work already existing in literature. Since the early rise of tandem PEC-WS, and similarly throughout the development of tandem PV systems, lots of work have been dedicated to assessing the current maturity of each technology and identify its development both on a near term and long-term scenario. These models share some common features, yet a dedicated declination which addresses each specific field is necessary. Therefore, taking as a reference the existing literature[90–93], a model which takes into account the peculiar characteristics of organic system will be designed, correlating the performances of PEC systems and envisaging their future development. A description of how the model is structured is provided in the Section IX of the Appendix. Herein the discussion will be limited to the most relevant outcomes and the key messages which serve as guideline for optimizing these devices.

3.7.1 Tandem Simulation – Current State

The model employed to describe this system allows, given as input several device-related parameters, to return the forecasted STH efficiency both for a specific combination of top and bottom absorber bandgap (the HPC and the PSC respectively) and for an extended range of combinations. These parameters (other than the bandgap of the photoabsorber) account for the series and shunt resistance (R_S and R_{Sh} respectively) the Incident Photon to Current Efficiency (IPCE), the External Radiative Efficiency (ERE), the BHJ-related voltage losses (V_{LOSS}) and the anodic and cathodic catalytic overpotentials ($V_{cat,a}(j)$ and $V_{cat,c}(j)$ respectively). Once these parameters are known, the J-V curve of each element can be obtained as output under a solar irradiance equal to the AM1.5G reference. The matching point is then calculated and similarly the STH efficiency (under the assumption of FE=100%).

To obtain the current-state scenario, the input-output order has been reversed. This allowed to extrapolate the aforementioned parameters for the HPC, PSC and Ru OER catalyst starting from their experimental polarization curves – i.e. those shown in Figure 18.a. Where missing, additional data have been taken from previously published articles concerning those architectures. The parameters obtained from this fitting are summarized in Table 2.

Table 2: Parameters obtained from the fitting of the J-V characteristics of the components and employed to obtain Figure 20.

Fitting Parameter	**HPC**	**PSC**
Normalized R_S	0.15	0.05
Normalized R_{Sh}	10^2	10^2
V_{Loss}*[V]*	0.41	-
IPCE	0.55	0.8
ERE	10^{-7}	10^{-5}
$J_{cat,c}$*[mA/cm²]*	0.25	-
$J_{cat,a}$*[mA/cm²]*	0.01	

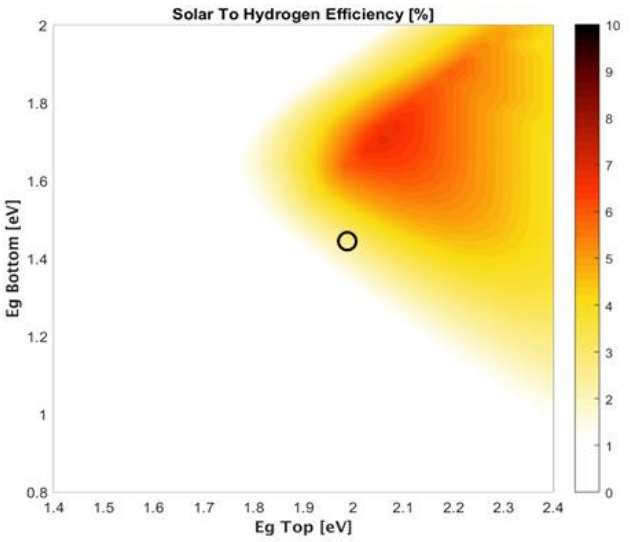

Figure 20: Contour plot of the STH efficiency as a function of the bandgap of the top absorber (HPC) and bottom absorber (PSC) describing the current state scenario. The parameters employed to model this behaviour are reported in Table 2. The black circle identifies the band gap combination of this HPC-PSC.

The result obtained from the model, with the parameters fitted from the devices, returns a STH efficiency of around 2%. This value is in excellent agreement with the experimental results, thus confirming the validity of the model in describing the system. Taking this condition as starting point, the analysis can be extended to a wider range of possible band gap combinations, assuming that devices with comparable performances shall be realized irrespective of the bandgap of the photoactive layer. This is visually represented by the contour plot shown in Figure 20. Here, the colour gradient identifies the calculated STH value for PEC-PV tandem systems as a function of the top and bottom absorber bandgap. The point which corresponds to the current combination is marked on the plot with a black dot (Top/Bottom E_G: 2 eV/1.5 eV).

The shape of this contour plot highlights several interesting topics. As a first consideration, it can be noticed that due to high amount of losses coming mainly from the catalysts and the HPC itself, a large fraction on the plot falls below the voltage threshold required to bias the water splitting reaction, thus returning STH= 0%. Only large bandgap materials provide enough photovoltage to withstand these losses, indeed the region with appreciable STH efficiency lies mainly in the top-

right quadrant of the plot. However, there is always a trade-off between photovoltage and photocurrent: a higher bandgap will lead to a larger photovoltage but at the expenses of a lower achievable photocurrent. This can be seen from the gradual STH decrease for larger bandgap combinations. Under these conditions the photocurrent turns out to be the main limiting factor, which thus limits the achievable STH.

This is further confirmed by the fact that the optimal combination at the current state requires to use a bandgap combination of 2.16 eV/1.8 eV. Provided that device with similar performances can be realized employing photoactive materials with these bandgaps, it would be possible to achieve STH as high as 5.85% with no further optimization.

3.7.2 Tandem Simulation – Short Term Perspective

Once the ground has been set and the model has been validated, it will be now investigated how the HPC-PSC tandem can be optimized to reach the highly anticipated 10% STH target[25]. To this extent, the adopted approach aims at performing a sensitivity analysis on the parameters employed to shape the current-state scenario. This will highlight which of these parameters exerts the strongest influence on the performances of the tandem stack. Also, it will point out where to act in order to gain the most in terms of STH efficiency without having to perform intensive optimization or completely redesign the devices architecture.

The intent is to limit the attention on the optimization of the HPC parameters alone, allowing to convey a meaningful message which provides a new perspective on the field. Furthermore, including the PSC would add many degrees of freedom to the sensitivity analysis, thus causing the final result to revolve around too many assumptions. Additionally, by plugging into the models the parameters of the current best performing PSC[94] the expected STH efficiency of the tandem stack would be of 2.4%. This marginal increase with respect to the current situation highlights how enabling a new efficiency regime requires to focus on optimizing the HPC first.

To perform the sensitivity analysis, the partial derivatives of the STH efficiency have been computed with respect to each HPC optoelectronic parameter (P_i – R_s, R_{Sh}, IPCE, V_{LOSS}, $J_{cat,c}$) through the Newton's difference quotient method with a 0.5% differential. According to the magnitude of each partial derivative ($|\partial STH/\partial P_i|$) it is possible to have a clear picture of which parameter leads to the higher variation on STH through its slight modification. This allows to shape the fastest path toward the 10% STH target.

Table 3: Parameters employed to model the optimized scenario (Figure 21) as a result of the sensitivity analysis.

Fitting Parameter	**HPC**	**PSC**
Normalized R_S	0.05	0.05
Normalized R_{Sh}	10^2	10^2
V_{Loss} [V]	0.3	-
IPCE	0.695	0.8
ERE	10^{-6}	10^{-5}
$J_{cat,c}$ [mA/cm^2]	0.5	-
$J_{cat,a}$ [mA/cm^2]	0.05	

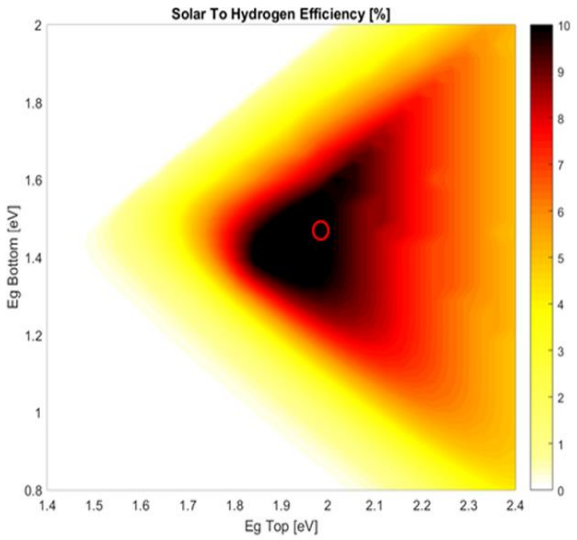

Figure 21: STH efficiency achievable in the short-term scenario if the performance of the HPC can be improved according to the results of the sensitivity analysis. The red dot identifies the combination of band gap of this HPC and PSC.

Among the aforementioned variables, those who exerted the strongest influence on the achievable STH have found to be the normalized series resistance R_S, the voltage loss V_{LOSS} and the incident photon to current efficiency IPCE. The initial set of parameters is then modified stepwise until the system reaches the targeted STH efficiency. This in turn allowed to build a new set of values (summarized in Table 3), which describes the optimized HPC.

The new STH efficiency scenario, depicted in the contour plot of Figure 21, now opens up to a much wider number of possible combinations which could return close to optimal STH efficiency. Once it translates to the materials selection step, it greatly eases the device design process as it allows more freedom to pick a suitable bandgap combination. As the extent to which potential losses contribute to hinder the performances has been reduced, the high efficiency area is now shifted toward narrower band gap combinations which are no longer current-density limited. Particularly, the best combination is now set at 1.88 eV/1.43 eV. From the HPC point of view, organic semiconductors which can match this E_G requirement are already being investigated. An example, published by Francàs et al.[35], employed a narrow-band gap push-pull copolymer (Poly[N-9'-heptadecanyl-2,7-carbazole-alt-5,5-(4',7'-di-2-thienyl-2',1',3'-benzothiadiazole)]) (PCDTBT) with a bandgap of 1.9 eV which allowed to reduce voltage losses and boost the photovoltage of their HPC. Similar examples in the OPV community demonstrated that by suppressing non-radiative recombination, V_{LOSS} could be reduced down to 0.2 – 0.3 V[51,95] with beneficial impact also on the IPCE, in accordance to the findings from the sensitivity analysis.

To tackle the issue of reducing the device series resistance, attention must be paid to perform reasoned material selection and integration in the final architecture. To

this extent, the charge selective contacts are those who ultimately affect the Rs value, eventually determining the final efficiency of the device. Lots of effort are currently being dedicated to identifying and optimizing materials which energetic structure and charge transport properties facilitate electrons/holes extraction from the photoactive layer. Additionally, materials employed in the field of HOPEC-WS should fulfil the additional requirement of electrochemical stability. This unavoidably narrows down the number of candidates which could be borrowed from the field of OPV, calling out to dedicated research.

3.7.3 Tandem Simulation – Long Term Perspective

Given the fact that the results recently obtained both in the field of OPV and HOPEC are well aligned with what has been identified as a promising route to reach the 10% STH target, it is meaningful to evaluate what could be the long-term goal achievable with this technology. To this extent, the current state-of-the-art will be set as a reference to forecast how would an HPC-PSC tandem perform if the same performances obtained for the PV cell could be translated into a high-performing hybrid organic photocathode.

Recently, OPV cells received renewed interest as record-breaking devices have been realized, obtaining PCE values above 15% employing newly designed organic semiconductors[47]. As for the current-state scenario, the input into the model were the J-V curve of this benchmark solar cell, obtaining its optoelectronic parameters which are also reported in Table 4. The so-obtained electrical characteristic was then superimposed to the polarization curve of a HER catalyst, obtaining a HPC-like behaviour. Upon coupling it to a PSC, the long-term STH efficiency has been obtained hypothesizing that HOPEC-WS could match the performances of OPV. The new STH landscape, shown in Figure 22, reaches a maximum of 19% STH when the HPC is coupled to a PSC which bandgap are 1.6 eV and 1.1 eV respectively. As for PSC, that the current lower bandgap limit is around 1.15 eV when Pb is replaced with Sn as a cation[96–99]. Furthermore, multiple examples already demonstrated the exceptional flexibility in terms of molecular engineering of organic semiconductors, which allows to freely tune the optical absorption profile of these materials targeting the desired bandgap[49,51,55].

Table 4: Parameters employed to model the tandem long term perspective (Figure 22) based on the OPV world.

Fitting Parameter	HPC	PSC
Normalized R_S	0.045	0.05
Normalized R_{Sh}	10^2	10^2
V_{Loss} *[V]*	0.1	-
IPCE	0.83	0.8
ERE	10^{-4}	10^{-5}
$J_{cat,c}$ *[mA/cm²]*	1	-
$J_{cat,a}$ *[mA/cm²]*	0.05	

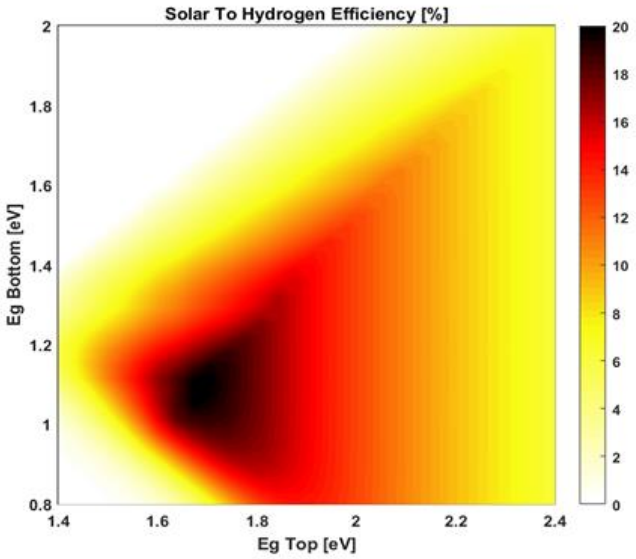

Figure 22: Long term perspective of the STH efficiency achievable with HPCs which match the performance of the current state of the art OPV devices.

This forecasted scenario is clearly not as likely as the short term one is, and surely the 19% STH estimated which almost doubles the 10% target is a goal which will require a lot of effort. Its main purpose is to highlight how dedicated material research and device optimization play a fundamental role in achieving breakthrough results, as demonstrated in the akin fields of OPV e PSC. While there is still a long road to go, having a clear scenario of what can be achieved with this technology will surely fuel the interest in this field.

Despite the difficulties tied to the harsh working environment, in next chapters the information gathered from the modelling of this system will be used to design novel architectures and identify new materials which will take steps forward to realize efficient and stable tandem systems based on organic materials, aiming at enabling a new efficiency scenario.

3.8 Conclusions

To summarize the results discussed in this chapter, a HPC was successfully optimized in a tandem oriented way, ultimately achieving the very first demonstration of a working HPC-PSC tandem which delivered substantial solar-to-hydrogen conversion with an efficiency of 2.03% from organic based systems.

Taking this result as a starting point, a model which efficiently describes these types of system has been designed and used to set the path to reach the highly anticipated target of 10% STH through a sensitivity analysis which highlighted the

most sensitive HPC-related parameter onto which attention shall be focussed in order to have a rapid return in terms of overall performances improvement.

Eventually, by looking up to the akin field of OPV, the long-term horizon was set by estimating how a record-OPV-like photocathode shall perform, if and when the field of HOPEC will reach the performances of its closely related solar cell counterpart.

All in all, the two main take-home-messages are that organic semiconductors based solar conversion technologies can play a fundamental role in storing renewables both in the form of electricity and the so-called solar fuels, where hydrogen is the most noticeable example. Eventually, this ambitious goal shall be reached only through dedicated materials research and designing architectures where the potential of semiconducting polymers shall be harnessed thanks to suitably selected charge extracting layers.

Chapter 4

Efficient and Stable HPC

Realizing a hybrid photocathode architecture which can couple efficiency and stability calls for complete change of paradigm with respect to the previous efforts. Most of all, the materials employed have to be electrochemically stable. This must be a requirement on which no compromises are accepted. Alternative approaches such as protective coatings have been proven to be inefficient to this extent, further leading to sudden failure of the device once a defect arises.

This chapter will address the development of a novel hybrid organic photocathode architecture in which all of its layers will be rethought almost from scratch, starting from its foundations (i.e. from the hole selective layer).

While doing this, the guidelines identified in the previous chapter will be kept in mind. The first task will be identifying and optimizing materials which can minimize the R_S of the device. This will require to optimize their energetic structure in terms of conduction and valence band position, work function and charge transport properties. Then the integration of a novel organic semiconductor will be performed, aimed at boosting the photon conversion efficiency, minimizing voltage losses and increasing the achievable photocurrent. Eventually, side issues connected to the mechanical instability of the catalyst interface will be solved, further extending the stability of the whole device.

As this optimization will be proven successful, some useful insights on the charge transfer processes occurring across the multilayered architecture will be gained. To this extent, impedance spectroscopy techniques will be employed, and the results discussed with an eye on the possible improvements.

Eventually, long term stability tests will be performed, proving the efficacy of this approach. Additionally, the performances of such devices will be assessed also in neutral pH, setting these results as a cornerstone for the realization of tandem system operating outside of the acid region of pH, with a substantial benefit on the overall kinetic of the water splitting reaction.

4.1 WSe_2 HSL – Initial Assessment and Thin Film deposition

The remarkable efficiency obtained with the previous architecture came at the expense of the device stability. Indeed, the cuprous iodide hole selective layer displayed excellent charge selectivity, but its intrinsic electrochemical instability severely hindered the lifetime of the HPC. To solve this issue, the performance of tungsten diselenide for this peculiar application will be investigated.

This material belongs to the class of TMDs compounds, which hold peculiar features in terms of charge transport properties which are mainly determined by their crystalline structure. Furthermore, they are widely exploited in electrochemical applications due to their superior stability[100]. According to available literature data, WSe_2 is the only one (at least among the most studied) which displays an intrinsic p-type behaviour[101]. Based on these premises, this material can be a prosing candidate as hole selective layer.

TMDs are widely investigated materials which drawn a lot of attention as atoms in their crystalline lattice are organized in layers, as for graphene. Thus, they are often investigated in the form of 2D materials in mono/few-layers. These are highly ordered structure which often require energy intensive synthesis methods to exert high control on the material's properties. This often comes at the expenses of the large area processing. To this extent, Pulsed Laser Deposition was employed to obtain thin films of WSe_2 with high control on the achievable morphology and thickness.

Their narrow optical bandgap translates in a high ablation rate in PLD, thus optimizing the process to fully exert control on the deposited film required a careful parametric optimization. This deposition technique allows to span over a broad range of achievable morphology, starting from compact thin films to nanostructured ones. Nanostructured thin films offer a large surface area and suitable through-plane charge transport properties thanks to the highly oriented growth perpendicular to the substrate. However, such nanostructuration properly develops only above a certain thickness threshold. While aiming at employing this material as hole selective layer, the final thickness should be kept as low as possible to minimize the through-plane resistance.

To combine the benefits of nanostructured thin films without introducing excessive resistive contributions, the aim was to terminate the deposition as soon as a seed-layer is formed. The seed-layer identifies the region of film which grows in close proximity to the substrate and it is formed by an aggregation of closely packed

nanoclusters with clearly defined boundaries both on the direction perpendicular to the substrate and in plane. For an easier understanding, in Figure 23 this region has been highlighted in blue on a SEM cross-sectional image of a PLD-deposited WSe_2 film. As it can be seen, the effect of self-assembled nanostructured growth is clearly evident above the first 100 nm. At the very basal region, the seed-layer serves as a nucleation centre for the subsequent growth of the nano-tree structure. These clusters can be closely approximated to nanocrystalline domains which should facilitate charge flow through the layer.

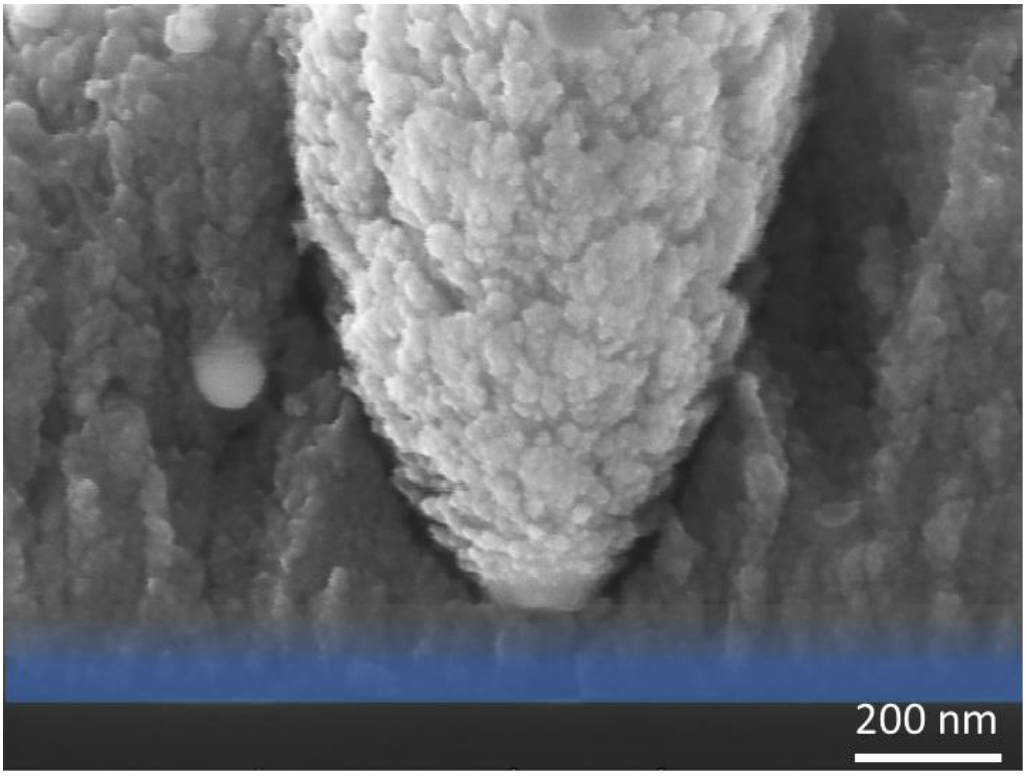

Figure 23: SEM cross section of a WSe_2 calibration film. The highlighted region identifies the seed layer in contact with the substrate while the nanostructured growth develops in the upper region.

To have a seed-layer terminated film, it is necessary to tune the process parameters so that the growth regime is slow enough to have a homogenous coverage with a target thickness lower than 50 nm. This can be achieved acting on the background gas pressure and laser fluence. Given the high ablation rate of this material, the optimal laser fluence has been set below 1.5 J/cm^2. Similarly, to ensure that the morphology of the film is not excessively compact, the background pressure has been tuned in the range 10 - 30 Pa. To avoid oxidation of the film, argon has been selected as background gas. This allows to tune the kinetic energy of the emitted species without inducing chemical modifications, thus preserving the stoichiometry of the target material.

Preforming a parametric optimization on these parameters allowed to adjust the quality of the film surface. Indeed, one of the main shortcomings of narrow-bandgap materials deposited via PLD is the occurrence of droplet-like defects.

These defects originate on the target material surface. When the laser radiation is absorbed from the target, the spatial energy distribution will determine whether the material will sublimate or just melt. Typically, the centre of the spot will sublimate while the adjacent region will melt. It is from this molten region that portions of liquified material are carried away along with the gas phase. As they travel toward the substrate, the outer shell solidifies and prevents the material to reorganize onto the substrate surface. As a result, these defects retain their droplet shape and cause discontinuities in the field. This leads to several major drawbacks. Firstly, given the poorer mechanical adhesion of these species, they tend to detach easily. This may happen both while the other layers are processed or during device operation. Additionally, these defects can work as trap sites where photogenerated charges can recombine causing a loss in performances for the HPC architecture. Their surface concentration has been minimized, allowing to reach a concentration as low as few droplets over an area of 50 μm^2.

As a result of this optimization, it was possible to achieve high quality films with minimal number of defects and suitable morphology. In Figure 24, a cross sectional image of the thin film is shown. The measured thickness is around 30 nm and it shows the onset of the desired columnar structure.

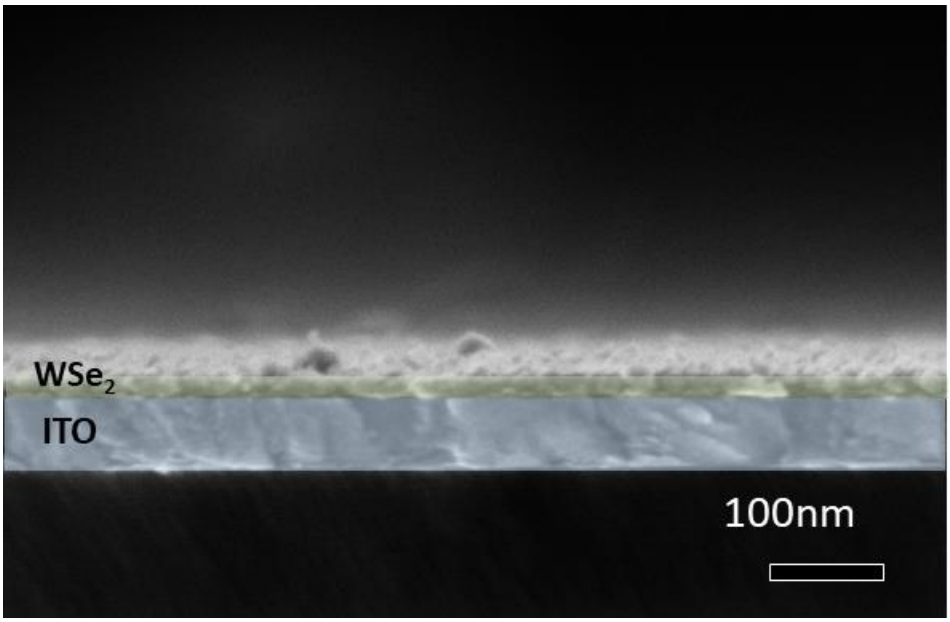

Figure 24: SEM cross sectional image of a 30-nm thick WSe_2 film growth on an ITO substrate.

The homogeneous coverage of the surface has been assessed via AFM for a thin film deposited on top of an ITO coated substrate. As shown in Figure 25.c, the topography image is characterized by a homogeneous distribution of clusters which follow the surface topography of the substrate (Figure 25.a). The phase contrast map shown aside (Figure 25.b for the bare ITO and 25.d for the WSe_2 film)

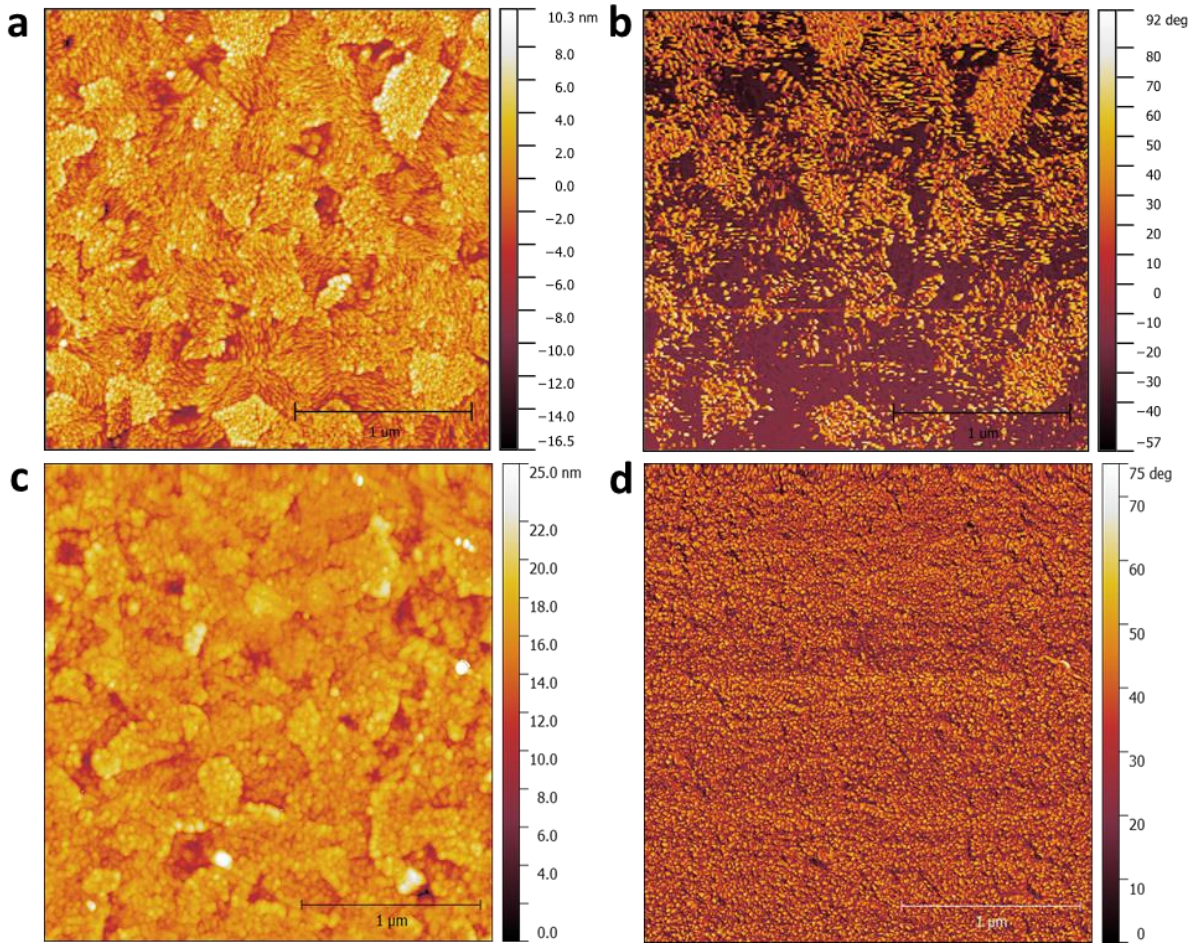

Figure 25: AFM topography (a and c) and phase contrast (b and d) images of the bare ITO substrate (a and b) and of the surface of the WSe_2 film.

corroborates the idea that the topography image is connected to the WSe_2 surface and no ITO is left uncovered. Indeed, being the phase contrast highly sensitive to difference in materials properties[102,103], if WSe_2/ITO interface would have been exposed a sharp discontinuity would appear on the phase contrast map.

The outcome of this optimization allowed to obtain a WSe_2 film with thickness of around 30 nm which successfully achieves a homogeneous coverage of the ITO substrate. The low roughness should facilitate the coupling with the organic BHJ and an efficient charge extraction. Furthermore, the grain morphology with lateral size of 15-30 nm which span for the entire thickness of the layer have the potential of offering a low-resistance path for charges to flow toward the TCO. The low defectivity of the film is an additional advantage, opening up to the opportunity of combining large area processing with high quality films.

4.2 WSe_2 HSL – Pristine Film Characterization

Once a suitable morphology has been identified, the obtained thin film can be then characterized thoroughly. The aim of this analysis it to build a comprehensive data set which will allow to perform a reasoned integration of this material in a HPC architecture.

To this extent, it is worth recalling the most relevant features sought while investigating materials for charge selective contacts application. A highly desired property is the optical transparency. This would allow both to ensure that all incoming photons reach the photoactive layer and that, in light of a future integration in a tandem system, minimal shadowing falls on the next element in the optical series. Furthermore, a suitable charge selectivity is requested. This is often estimated taking into account the conduction and valence band position and the work function of the material. Additionally, the material must be electrochemically stable at the desired pH and in the applied potential region. Eventually, information about its chemical structure and crystalline phase allow to further clarify the material behaviour.

The as-deposited material, as from a naked eye observation, displayed an intense brownish colour despite the low film thickness. To quantify this, transmittance, reflectance and absorptance data have been acquired in the wavelength range between 250 and 800 nm. Transmittance and reflectance have been directly measured *via* a spectrophotometer equipped with an integrating Spectralon™

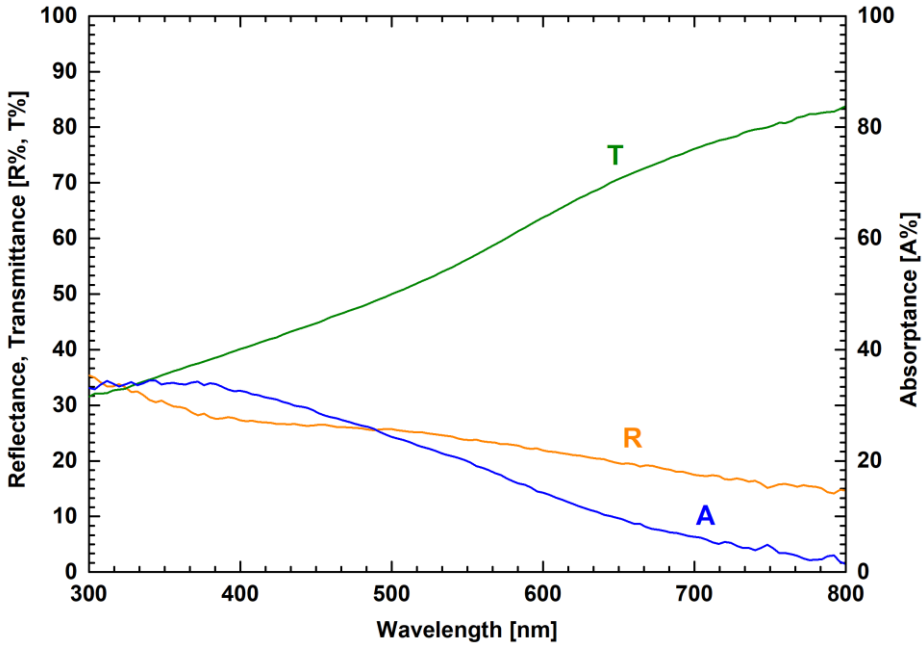

Figure 26: Reflectance, Transmittance (left Y-axis, green and orange lines respectively) and absorptance (right Y-axis, blue line) of the pristine WSe_2 film.

sphere. Absorptance was calculated from the knowledge of the two other components. The three components are shown in Figure 26. The intense and extended absorption profile suggests that the film is mainly amorphous with a high amount of defects in the structure. This is consistent with what expected from PLD films. Indeed, as-deposited materials are characterized by a large number of nanocrystalline domains. Recalling the AFM topography image (Figure 25.c), these nanocrystalline domains can represent a fraction of the clusters appearing on the surface. Furthermore, during the deposition process a segregation of the two elements can occur. This can lead to the formation of Se-rich zones and W clusters which can work as scattering centres, ultimately determining the absorption and optical appearance of the film. Thinking at the future integration of this material in the HPC architecture, its intense absorption may cause serious limitations to the performance of the BHJ. By taking as a reference the absorption profile of P3HT:PCBM, which main absorption peak is in the region between 400 nm and 550 nm, it suggests that a non-negligible fraction of photons may be lost prior reaching the BHJ. This issue can in principle be solved by reversing the illumination direction (i.e. shining the light from the catalyst side), but it would still represent an issue when envisaging the integration of the HPC in a tandem system.

the hypothesis of the film being mainly amorphous and with zones with excess unbound selenium has been further investigated. The acquired Raman spectrum (Figure 27) supports this argument. On the plot, reference vibrations known from literature have been labelled. Several contributions, some of which are likely to be

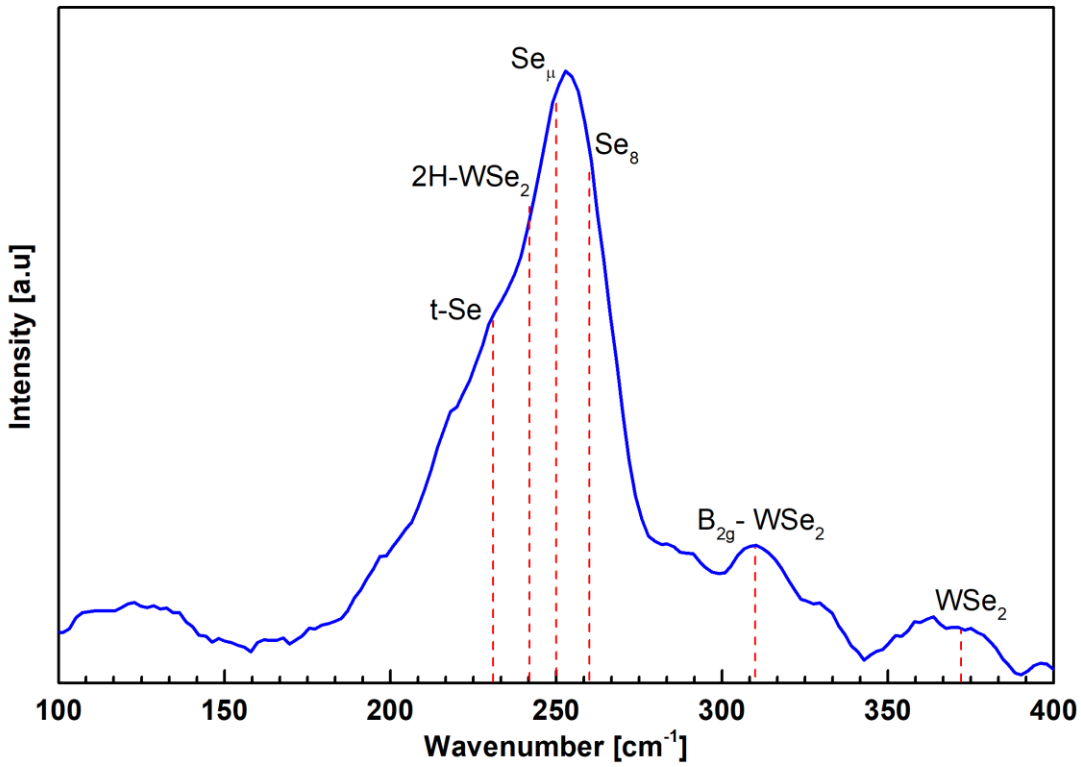

Figure 27: Raman spectra of the pristine WSe_2 film (blue line). The reference vibrations are reported on the plot.

convoluted in the acquired signal, can be identified. Given the narrow range of Raman shifts in which the main vibrations occur and due to their partial overlap, a peak fitting may return unreliable information. Nevertheless, the spectrum of the as-deposited material is likely to be a superimposition of the vibrations of pure selenium with a partial contribution coming from some clusters of crystalline WSe_2. Indeed, Raman analysis on non-crystalline selenium[104] highlighted three main bond-stretching vibrations in the region between 230 cm^{-1} and 260 $cm^{-1.}$ These are labelled on the plot as t-Se (231 cm^{-1}), Se_{μ} (250 cm^{-1}) and Se_8 (260 cm^{-1}). Following the increase in Raman shift, they are addressed to intrachain bond stretching vibrational modes of trigonal selenium (t-Se) and disordered Se chains (Se_{μ}) and intraring bond stretching (Se_8). Additionally, vibration at 372 cm^{-1} represent a clear signature of WSe_2 films while the B_{2g} mode peak at 310 cm^{-1} arises in WSe_2 films as soon as the translational symmetry of the lattice is broken, which is consistent with what expect from this film[104]. By contrast, the 2H-WSe_2 vibration at 242 cm^{-1} is partially covered by the other contributions[105,106]. The highly disordered structure, unfortunately, does not allow a straightforward comparison with literature. Indeed, several works report the Raman spectra of WSe_2 in mono/few-layers or crystals[105,107,108], while only few publications report on materials relatable to the one currently investigated[109,110].

Nevertheless, the Raman analysis on the pristine film supports the hypothesis suggested from the UV-Vis characterization. Indeed, few contributions from crystalline WSe_2 are present while the spectrum is mainly characterized by the vibrational features of selenium which can be thus addressed as responsible for the intense optical absorptance of the thin film. This Se segregation is expected to exert an influence also on the electronic properties of the film, as it may act as a p-type dopant[101]. The work function, measured through KP microscopy, is of 4.8 eV. While several values are reported in literature[111–114], the measured value lies in the lower end of the range (i.e. among the materials with the deepest work function with respect to the vacuum level). This value cannot give an indication of the p- or n-type behaviour of the material *per se,* as the knowledge of the CB and VB position would be necessary. Nevertheless, it bodes well for the integration of this material in the HPC architecture, as its WF is suitably aligned to extract holes from the HOMO level of several donor polymers.

To conclude the analysis on the pristine material, its electrochemical stability was assessed through cyclic voltammetry in the potential range between 0 V_{RHE} and 1 V_{RHE}. The data, shown in Figure 28, highlight that the material is overall stable throughout the whole measurement as no irreversible peaks occur in the potential range of interest. A slight asymmetry is shown at the reduction/oxidation limits of the scan. In the very first scans, a high oxidation current is recorded, which magnitude decreases in the following scans. This is consistent with an oxidation of excess Se[62]. This process has a transient behaviour which fades as all the unbound

Se clusters are oxidized and removed from the structure, thus leading to a less defective structure.

The complete picture, as a result of the information gathered, suggests that this material is already a good HSL candidate in its as-deposited condition. This conclusion is drawn according to its electrochemical stability and suitable work function alignment. Yet, it points out the fact that there is still plenty of room for improvements when it comes to the optical transparency and crystalline structure of the film, as suggested from the UV-Vis and Raman spectroscopic data. Based

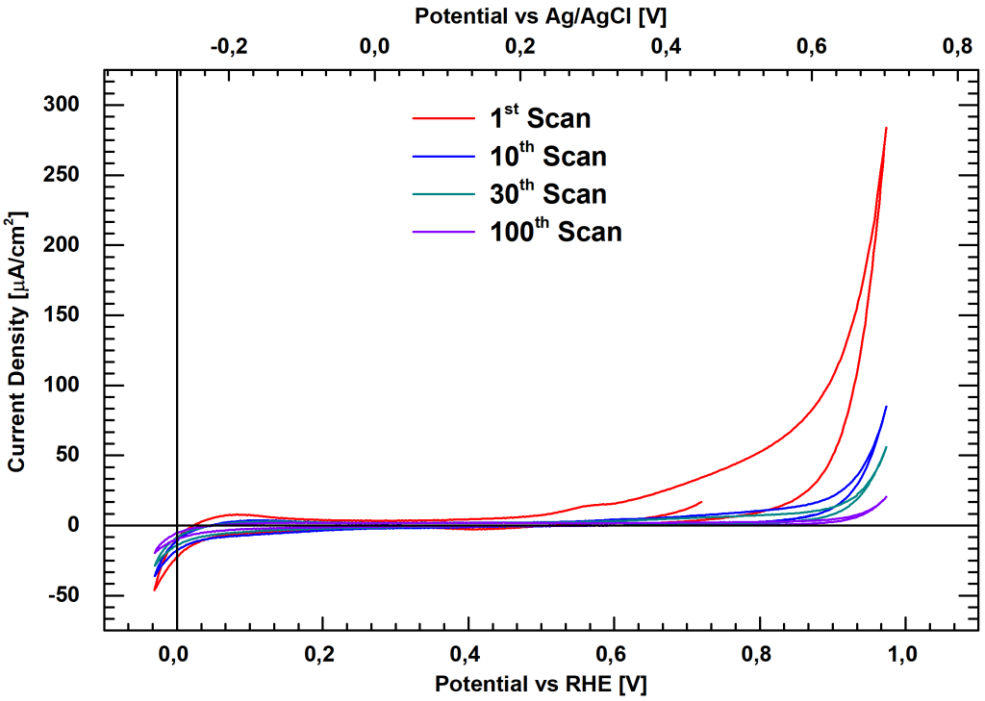

Figure 28: CV of the pristine WSe_2 film. The colour coding of each curve refers to a different scan number, as reported in the legend.

on these premises, a further optimization of this film is designed aiming at assessing its evolution as a function of post-deposition treatments.

4.3 WSe_2 HSL – Post-deposition Thermal Treatment

The characteristic features of the film in its as-deposited condition are the ultimate result of the physical processes which take place during the deposition. Nevertheless, acting on the deposition parameters themselves to improve the properties of the film would be insufficiently effective since the upper limit to achieve a defect free film has already been reached. To give an example, increasing the laser power would provide more energy to the emitted species which could then increase the size of the nanocrystalline domains once they reach the substrate. However, this would also lead to an increase in droplets concentration on the surface of the film, which effect would outplay the benefits of a more

ordered structure. The best way forward to tune the properties of the as-deposited material is to provide it with enough thermal energy so that the structure will spontaneously reorganize.

Post deposition thermal treatments are thus performed in a temperature range from 200°C to 450°C. In order to avoid oxidation of the film and phase segregation of the ITO substrate, the annealing is performed in vacuum ($3*10^{-3}$ Pa base pressure) in a resistively heated quartz tubular furnace. Eventually, the effect of the background gas will be discussed for the low range of annealing temperatures. This will allow to compare the behaviour of the material at 200°C in vacuum or in N_2 atmosphere, retrieving some useful insight on the reorganization dynamic of the film.

The upper and lower bound have been selected to grant the integrity of the glass substrate (at high T limit) and taking into account the expected melting temperature of Se (T_m^{Se} = 220°C, low T limit). The annealing time has been set to 2 hours for each condition. Heating and cooling ramp has been set to 4°C/min. To build a consistent data set, the annealed films will be characterized according to what discussed for the pristine film.

The evolution of the Raman spectra gives an indication of the reorganization of the film as a function of the annealing temperature. In Figure 29, the data collected from the 200°C to the 450°C annealed film are shown. Three regions which corresponds to three steps of the phase structure reorganization can be identified. The first one is indeed the one corresponding to the pristine film, as discussed in the previous section. Looking at the high temperature end of the annealing series (350°C – 400°C – 450°C), the Raman spectra of the film closely matches the one of the 2H phase of tungsten diselenide. Here, in the region between 200 – 300 cm^{-1}, the main peak is a convolution of the unresolved peaks corresponding to the in-plane E^1_{2g} and out-of-plane A_{1g} modes of 2H WSe_2 [115], which is in excellent agreement with literature data. This points out that, starting from temperatures as low as 350°C, the mainly amorphous films start to reorganize in the form of the semiconducting 2H phase. While this phase transition is complete for the higher annealing temperature (450°C), the process is not yet concluded for the two other temperatures. Due to the lower thermal energy available, it is reasonable to infer that in order for the structure to complete the phase transition, a longer annealing time would be necessary. In the temperature range between 200°C and 300°C, the Raman signal is remarkably weaker than in the other conditions. Yet, the onset of some peaks can be identified. Starting from the lower temperature (200°C), the spectra completely lose the prominent contribution shown in the pristine state. This corroborates the idea that that signal was indeed originated from an excess of unbound selenium in the structure. Due to the fact that selenium has a vapour pressure of around 200 Pa close to its melting point, which is higher than the actual

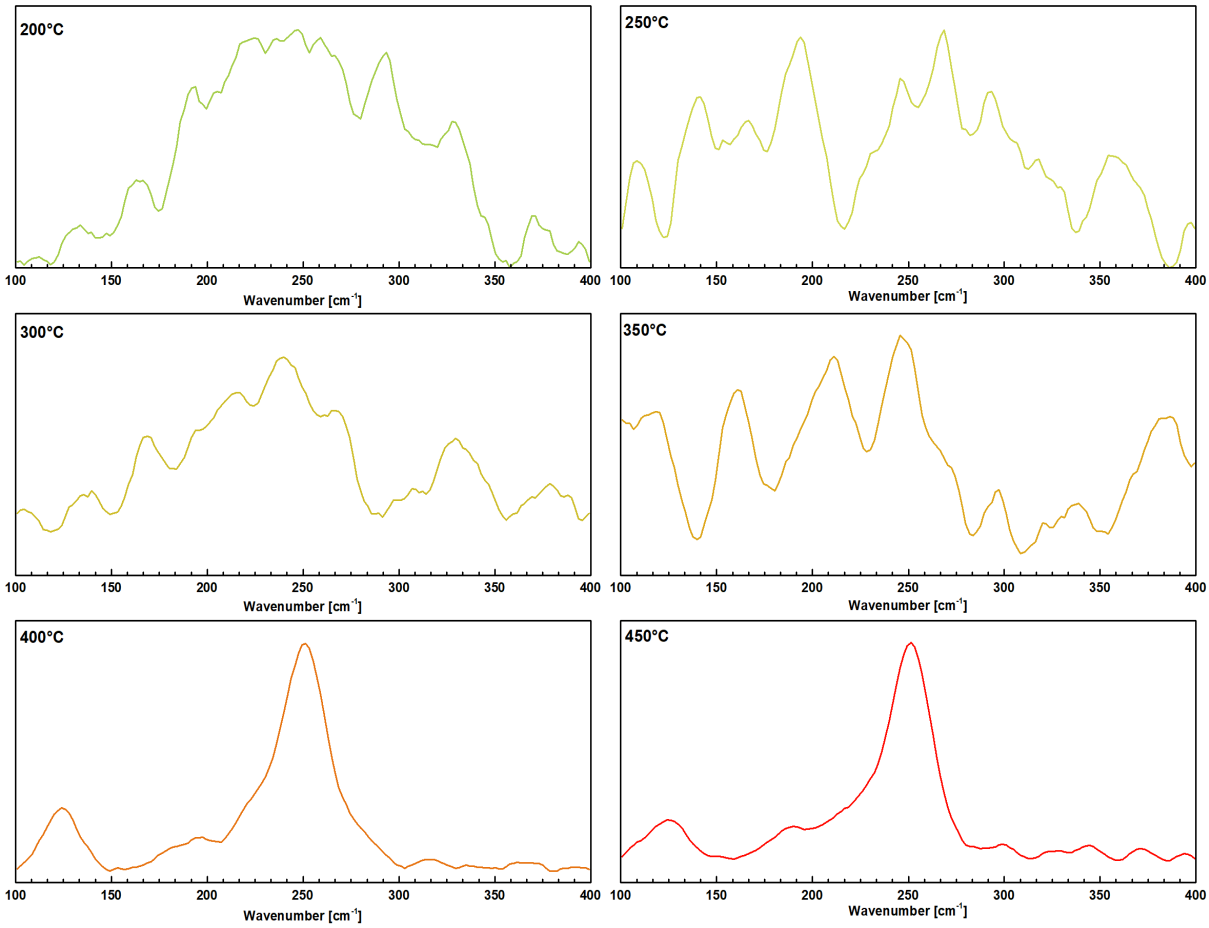

Figure 29: Raman spectra of the annealed WSe_2 film. The annealing temperature is reported in upper-left corner of each panel.

pressure in the furnace, it can be concluded that the thermal treatment effectively removed all the unbound selenium in the film. This suppressed its Raman signal in the 200°C annealed film.

As the film still has a substantial amorphous fraction, the intensity of the spectra is still extremely low. Furthermore, WSe_2 (like the other TMDs) can organize its structure in a metallic-like phase, the 1T. If this structure is distorted, it is usually labelled as 1T'. When atoms adopt this configuration, the material is capable of a poor interaction with light, which further justifies the low intensity. Nevertheless, as the annealing temperature increases (250°C – 300°C) a series of peaks can be identified. According to literature, they occur at 104.5, 149, 177, 218, 236.3 and 258 cm^{-1} but to date they have not been assigned to any specific vibrational mode[115]. A rigid shift to lower wavenumbers occurs for almost all the modes which is in the order of 5 -10 cm^{-1}. From this information, it can be inferred that the material in this range of temperatures is undergoing a phase transition from amorphous to 1T/1T', the latter being predominant. The extent to which this transition is occurring is highly dependent on the annealing temperature. Indeed, a more accurate match with literature data is found on the 300°C annealed film which is expected to have experienced a faster reorganization kinetic, thus bringing it closer to attain this metastable phase.

The electronic structure of the thin films is expected to reflect the modifications suggested from the Raman analysis. Ultimately, all the aforementioned effects such as the phase transition and Se removal have a strong influence on the material's work function. To this extent, KP microscopy has been performed on the annealing series. To clarify the influence of selenium removal, an additional annealing experiment was planned in which the treatment has been performed in N_2 atmosphere at ambient pressure at 200°C and 250°C. Provided that the pressure is higher than the vapour pressure of Se, it would be expected that the film incorporates it with a different kinetic with respect to what seen for the vacuum annealing.

In Figure 30, the series of acquired value is shown. The colour coding refers to the different annealing atmosphere (green for vacuum and red for N_2). As for the Raman spectra, three regions can be identified, which are consistent with the previous observations. The abrupt transition between 300°C and 350°C is in excellent agreement with the structural reorganization which brings the material from amorphous/1T to the semiconducting 2H phase. At this boundary, the WF shifts from 4.69 eV to 4.45 eV. This can be explained taking into account that upon switching from the 1T to the 2H phase, the band structure of the material reorganizes to give a more defined bandgap. As the transition is still incomplete at 350°C, the defective structure may lead to a disorder-induced upshift of the work

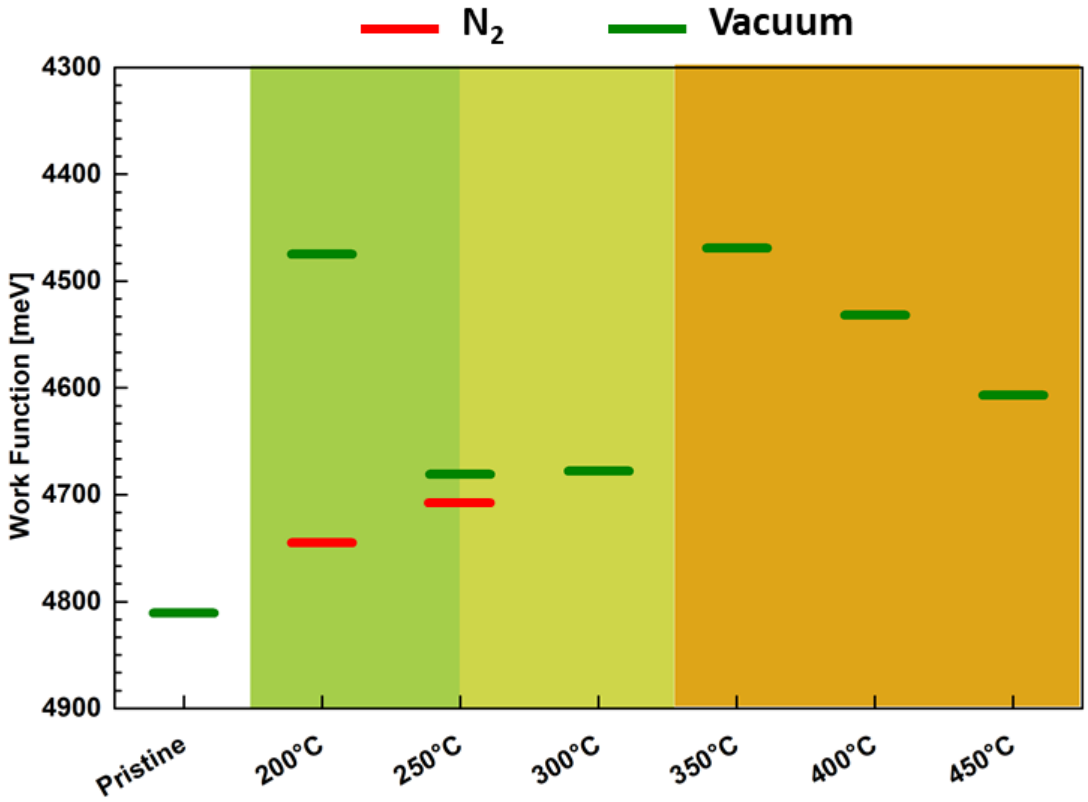

Figure 30: Average Work Function values of the WSe_2 films measured via KP. The red bar refers to the film annealed in N_2 atmosphere.

function[114]. For higher annealing temperatures, the work function decreases down to the value of 4.6 eV.

On the lower end of the annealing series, the influence of residual Se on the work function of the material while it reorganized into the 1T/1T' phase can be appreciated. A remarkable difference is found when the annealing is performed at 200°C, where the WF in vacuum and in N_2 are 4.46 eV and 4.74 eV respectively. This confirms that for temperatures as low as 200°C complete Se removal can be achieved by performing a vacuum annealing to the film. On the other hand, employing N_2 as a background gas allows to retain the initially unbound Se and provide it with enough energy for it to be included into the structure while it reorganizes. This leads to an appreciable p-doping effect, as suggested by the deeper work function and confirmed by literature[101]. This effect saturates for higher annealing temperatures, where the difference in work function @250°C is slightly appreciable.

To further confirm the suggested thermally controlled phase transition, one can take advantage of the different behaviour of the 1T / 2H phase in terms of light absorption. Indeed, the semiconducting behaviour or the latter should give a clear feedback of which phase is present in the material. In Figure 31, the absorptance spectra of the films annealed at different temperatures are shown (for sake of clarity, some temperatures which displayed not significant difference from the other plots have been omitted). As expected, upon Se removal the magnitude of

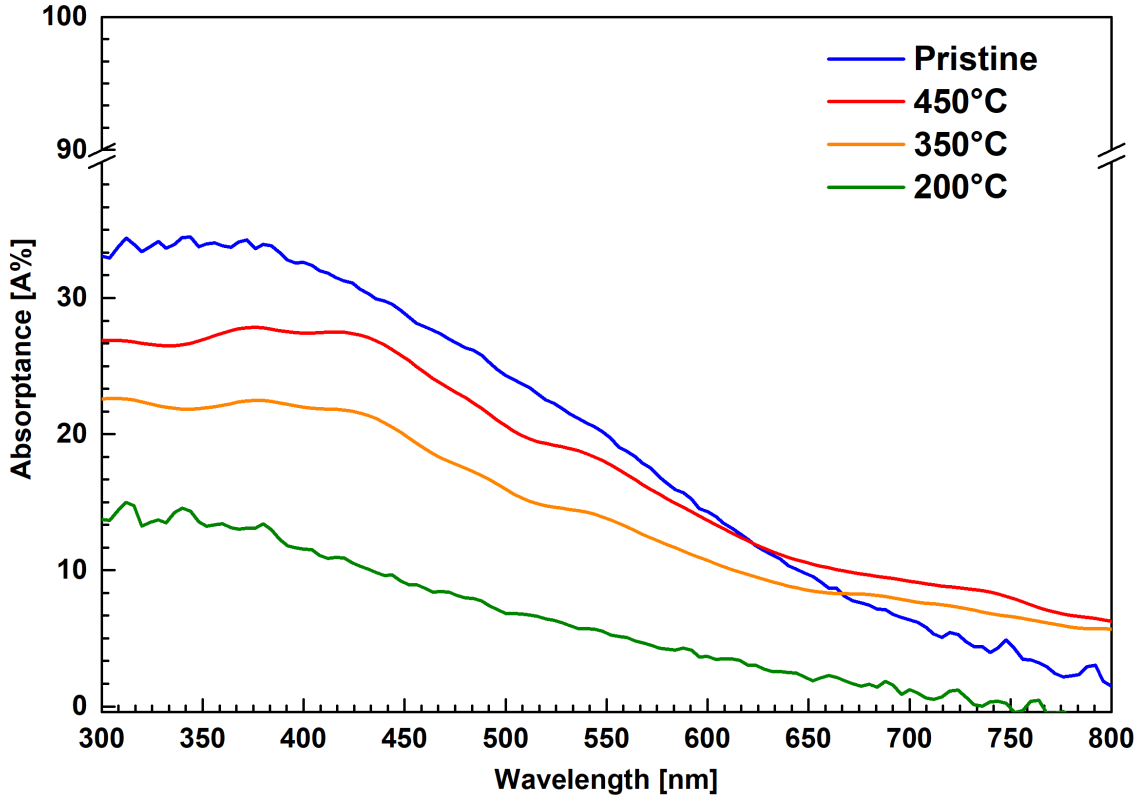

Figure 31: absorptance spectra of the WSe_2 films. The colour coding is reported in the legend. For an easier reading of the figure, 250°C -300°C and 400°C have been omitted as they did not display significant differences with respect to the 200°C and 350°C conditions respectively.

the absorptance decreases while the material starts to reorganize in the 1T/1T' phase as compared with the pristine film. Nevertheless, it is still not possible to identify a clear optical bandgap. This suggests that the material is, as expected, still mainly amorphous or in the metallic phase. By contrast, the absorptance of the higher end of the annealing series (450°C) increases with respect to the 200°C annealed film. Provided that the initial film was equal in thickness (prior annealing), this sharper absorption profile points out to the occurrence of the 2H phase where the electron promotion to the CB upon photon absorption happens with a more precise energy (i.e. the band gap energy) rather than occurring from defect states which typically have a random energy distribution and lead to a broad optical absorption.

From the 450°C annealed film, which displays a distinct semiconducting behaviour, it was possible to estimate its optical bandgap by means of the Tauc Plot. The measured value of 1.45 eV is slightly red-shifted with respect to literature data, suggesting that this material is closer to the bulk-properties rather than to the monolayer ones[116]. This is confirmed also by the absence of the excitonic peak at 760 nm, suggesting that the material has in indirect bandgap with a minimal influence of excitonic quantum confinement[117].

From a structural point of view, the information gathered through KP, Raman and UV-Vis spectroscopy already offer a comprehensive perspective on the evolution of this material. This analysis can be concluded by ensuring that the material retains its electrochemical stability through all the annealing temperatures. As shown by the CV in Figure 32 – Panels a to f, all the phases display a behaviour similar to the one of the pristine film (Figure 28). The only difference is the magnitude of the measured current at the reduction/oxidation limits of the scan as a function of the scan number. Also in this case, a partial explanation can be given according to the oxidation of some metallic clusters present in the film. On top of this, the different phases are expected to behave differently when it comes to their electrochemical activity. Provided that no hydrogen or oxygen evolution is expected to take place in this range of potential, the recorded current may be addressed to the adsorption/desorption of ionic species on the surface, where the different efficiency of the binding sites can determine the current density value.

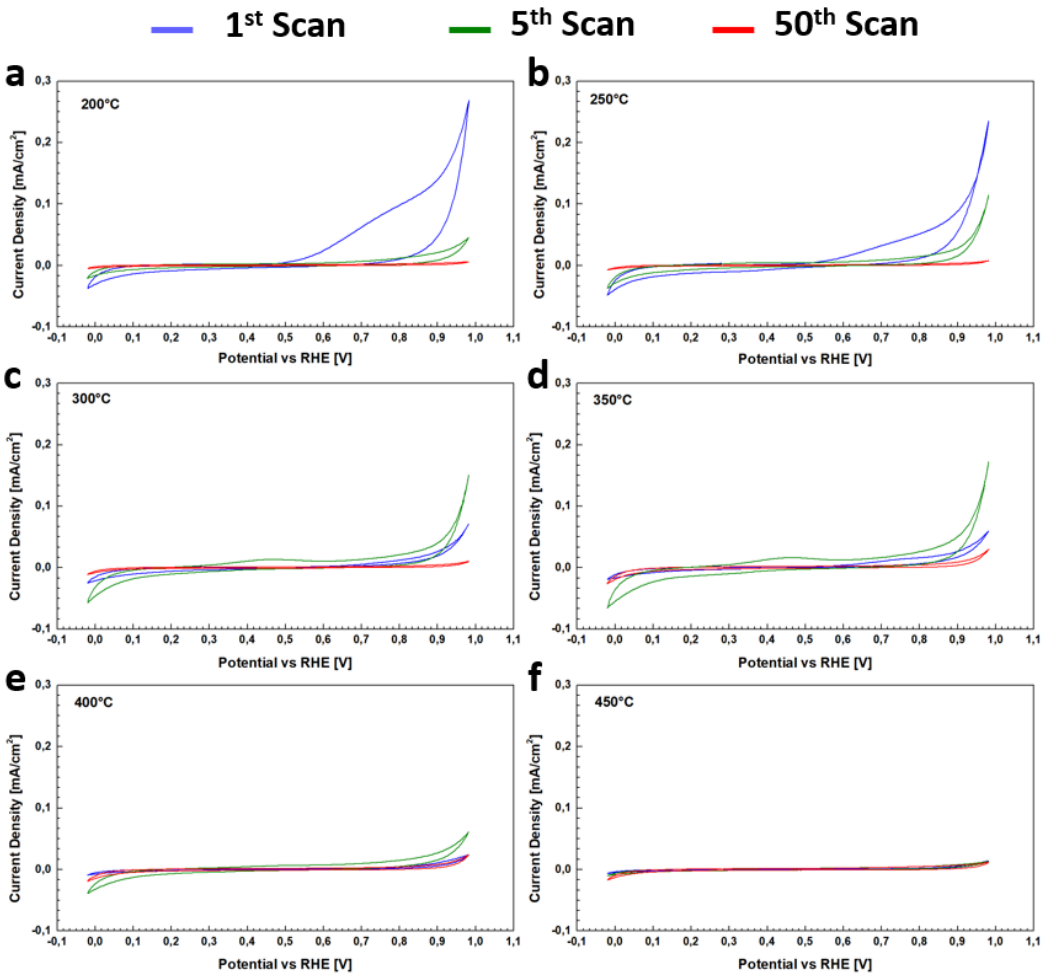

Figure 32: CV of the WSe_2 films annealed at different temperatures. The annealing temperature is reported in the upper-left corner of each panel. The colour coding of each curve is reported above the panels and refers to different scan numbers.

To provide a clearer explanation of the non-linear scan dependent behaviour, the current density at the cathodic (0 V_{RHE}) and anodic (1 V_{RHE}) limits has been plotted against the scan number (Figure 33.a and 33.b respectively). The behaviour at the two sides is symmetric, thus the attention shall be limited to the cathodic side for sake of brevity. The current density value has, on all the conditions, a peculiar dynamic which after the initial scan reaches a maximum value (in absolute value) and then decreases up to reaching a plateau. The scan at which the maximum value is reached increases linearly as a function of the annealing temperature. This behaviour can be seen as an electrochemical reorganization process, which dynamic is dependent on the starting phase. As an example, to more stable 2H phase (obtained with the 450°C anneal) reaches its maximum after 20 cycles while the one closer to the amorphous structure (200°C) coincides with the initial one. The suggested interpretation of this behaviour is that the material, being subjected to an alternated polarization, is forced to adsorb/desorb different species which, upon interaction with the surface, cause a structural reorganization. In particular, when it comes to H^+ ions, a fraction can be intercalated into the bulk thus

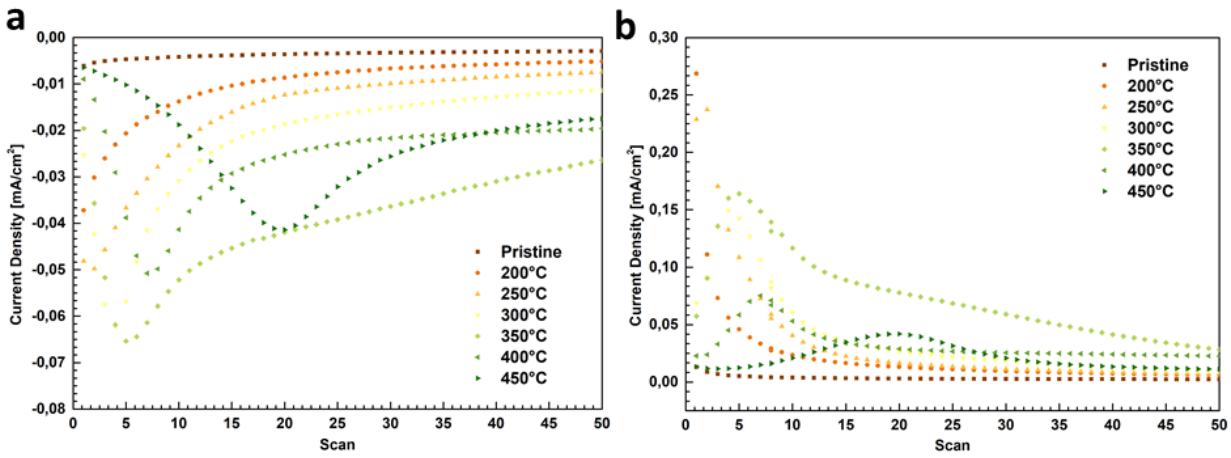

Figure 33: Current density at the cathodic (a) and anodic (b) limits of the CVs as a function of the scan number. The colour coding refers to the different annealing temperature and is reported in the Figures legend.

deforming the lattice. When it comes to not completely ordered structures, such as for the lower annealed temperature films, this process occurs with a faster dynamic as unsaturated sites are more prone to reorganize to minimize the lattice energy. While the process is thought to happen similarly on all the conditions, the different magnitude of the current at the 50th scan suggests that the reorganization does not lead to the formation of the same final phase but rather causes a deformation of the starting one.

As a result, it can be concluded that the designed post-deposition treatment has been proven to be phase-selective, allowing to finely tune the properties of the as-deposited material. Acting on the annealing temperature and atmosphere, successful switching across the 1T', 1T and 2H phases of tungsten diselenide was achieved, eventually tuning its optical and electronic properties. This knowledge will play a fundamental role when planning the integration of this material in a HPC architecture, as its properties can be adjusted to match the energetic levels of the organic photoactive layer. This is expected to play a fundamental role in maximizing the efficiency of the device. Furthermore, provided that the electrochemical stability of the material has been proven for each of the accessed phases, the integrity of the device will be granted irrespectively of the nature of this layer.

The interest of these findings spans beyond HOPEC-WS, as engineering this material may return interesting outcomes also for traditional PV cells[118,119], catalysis[18,62,107,120] and other fields in which TMDs are being investigated[109,121].

4.4 HPC integration of WSe_2 HSL

According to the dataset obtained from the characterization of WSe_2 thin films under various annealing conditions, the performance of this material in a Hybrid Organic Photocathode architecture can now be assessed. As a preliminary analysis, the available information will be combined with the aim of forecasting the experimental performances of the devices. This will serve both as a guideline to design an efficient architecture and to further validate the previous hypothesis.

A useful guide to perform this integration can be done according to the band structure of the material which can be then coupled to the other layers' one. A direct information could have been obtained from UPS analysis, retrieving the VB position and Fermi energy. Then, from the knowledge of the bandgap, the complete picture could have been built. Provided that these measurements could not be performed, a solid hypothesis based on the available data will be now provided. From the previous characterization a clear information on the work function, the phase and (at least for the 450°C annealed film) the optical bandgap was obtained. This can be further complemented with literature data.

The suggested band structure for the different phases is shown in Figure 34. A step-by-step explanation of how it has been obtained is herein discussed. The starting point will be matching the obtained data with the ones from literature regarding the most investigated phase – i.e. the 2H semiconducting one. The measured optical bandgap of this condition was 1.45 eV. From literature, the position of conduction band minimum and valence band maximum of WSe_2 films with similar bandgap are -3.75 eV vs Vacuum and -5.15 eV vs Vacuum respectively. This information can be complemented with the measured work function (dotted line in the graph). Literature shows that upon transitioning from the 1T to the 2H phase the bandgap increases. So, going backwards, the films annealed at lower temperature should have a narrower bandgap. Additionally, this transition is accompanied by a slight downshift of CB and an appreciable upshift of the VB[122–125]. Thus, the band structure of the other shown conditions is built according to the aforementioned information and completed with the measured work function value. In this picture, all the conditions show a predominant p-type character which is consistent with what expected from this material.

To evaluate the integration of this layer in the HPC it's necessary to estimate how it couples with the donor polymer. In particular, the position of the VB should lie higher in energy than the HOMO level of organic semiconductor. Since the aim of this work is to investigate novel materials to be employed in the organic BHJ, it was essential to identify a suitable candidate to replace P3HT. The most promising option was found to be the novel push-pull copolymer PCDTBT, which has also

been recently employed in HPC architectures by other groups[35]. This also provides the knowledge that this material is electrochemically stable, further simplifying its integration in the device under development.

The HOMO-LUMO energy of this donor polymer are -5.25 eV and -3.76 eV respectively. In principle, the HOMO level should be suitably aligned with all the suggested band structures. This should grant an efficient extraction of photogenerated holes. The main difference across all the conditions is expected to be the driving force generated by the energy offset at the interface, which is expected to be larger for the 200°C annealed film and almost negligible for the 450°C annealed film. A high driving force is desired as it prevents recombination of photogenerated charges within the BHJ.

Similarly, considering electron injection from the WSe_2 film to the PCDTBT film, suitable charge flow should occur on all the conditions except for the pristine film. In this case, the position of the CB of WSe_2 is expected to lie lower in energy than

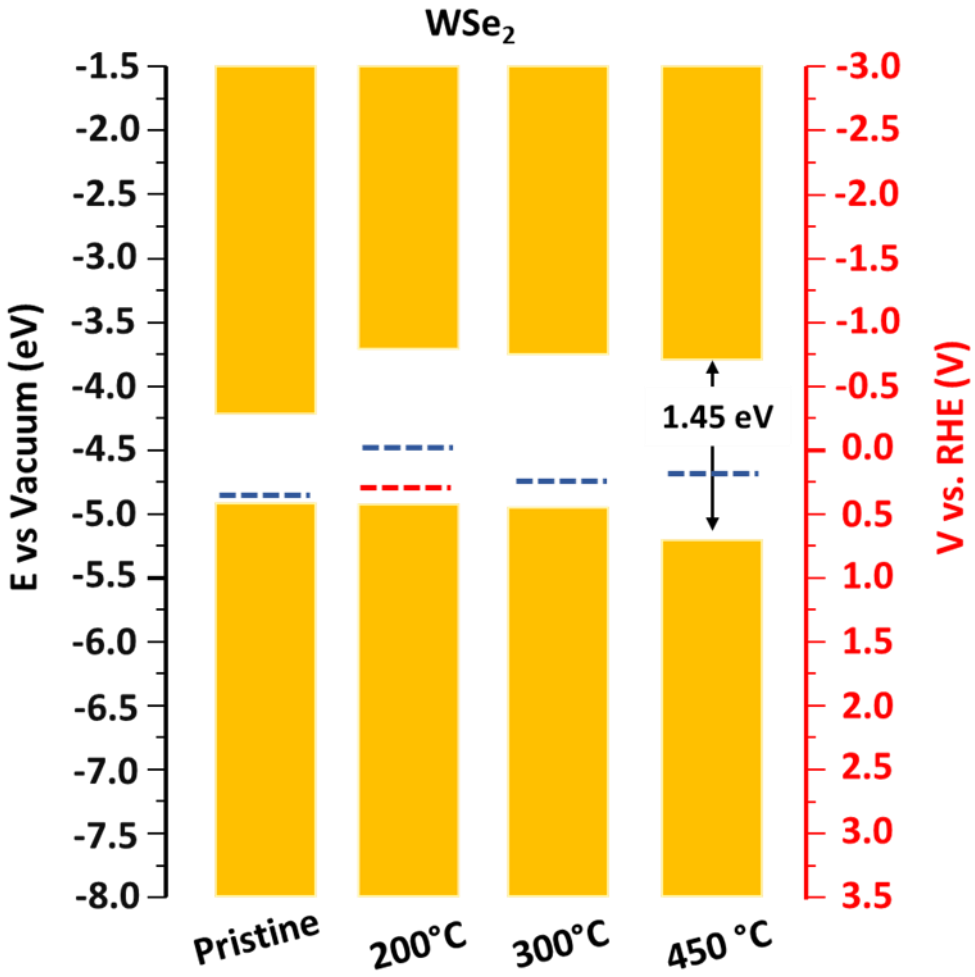

Figure 34: Suggested band structure of the most significant conditions, obtained from the combined knowledge of the previous characterizations and complemented from literature. The position of the VB, CB and E_F are reported vs Vacuum and vs RHE. The value of bandgap calculated for the 450°C annealed film is shown.

the LUMO of the polymer. This could cause photogenerated electrons to be competitively extracted toward this layer rather than to the fullerene acceptor. As a result, the photogenerated charges are very likely to recombine in this layer, leading to an overall performance reduction.

Based on these premises, WSe_2 should work efficiently as HSL when coupled with a BHJ employing PCDTBT as a donor polymer. While a difference in behaviour is expected according to the suggested energetic structure, additional insights shall be retrieved only once the full device has been realized. This will also shine light on the validity of the previous considerations.

4.4.1 HPC Photoelectrochemical characterization

This section will be focused on the performances of HPC realized with WSe_2 based HSL coupled with an organic bulk heterojunction which employs the push-pull copolymer PCDTBT and the fullerene acceptor $PC_{70}BM$. The full device architecture is ITO/WSe_2/PCDTBT:$PC_{70}BM$/TiO_2/Pt. The photoelectrochemical characterization will be performed in diluted H_2SO_4 aqueous solution (pH = 1.25) and under simulated sunlight illumination with spectral irradiance corresponding to the AM1.5G spectrum. For each device realized with WSe_2 annealed under different conditions, a minimum number of 4 identical replica samples have been measured to assess the reproducibility of the process.

In Figure 35 the polarization curves of the tested devices are reported. For each device, the sample has been illuminated until the open circuit potential reached a stable value. From that value, the potential was scanned down to 0 V_{RHE}. As expected, there is a remarkable difference in the photoelectrochemical behaviour as a function of the thermal treatment performed on the HSL.

As for the photocathode employing the pristine film, it is the one which returns the lower efficiency both in terms of photovoltage and photocurrent (0.45 V_{RHE} – 2.5 mA/cm^2). This may be explained according to the less suitable energetic alignment. In this configuration, a substantial amount of photogenerated charges is expected to undergo recombination prior that they can be extracted from the device. This translates to the lower value of photocurrent and poorer fill factor of the curve.

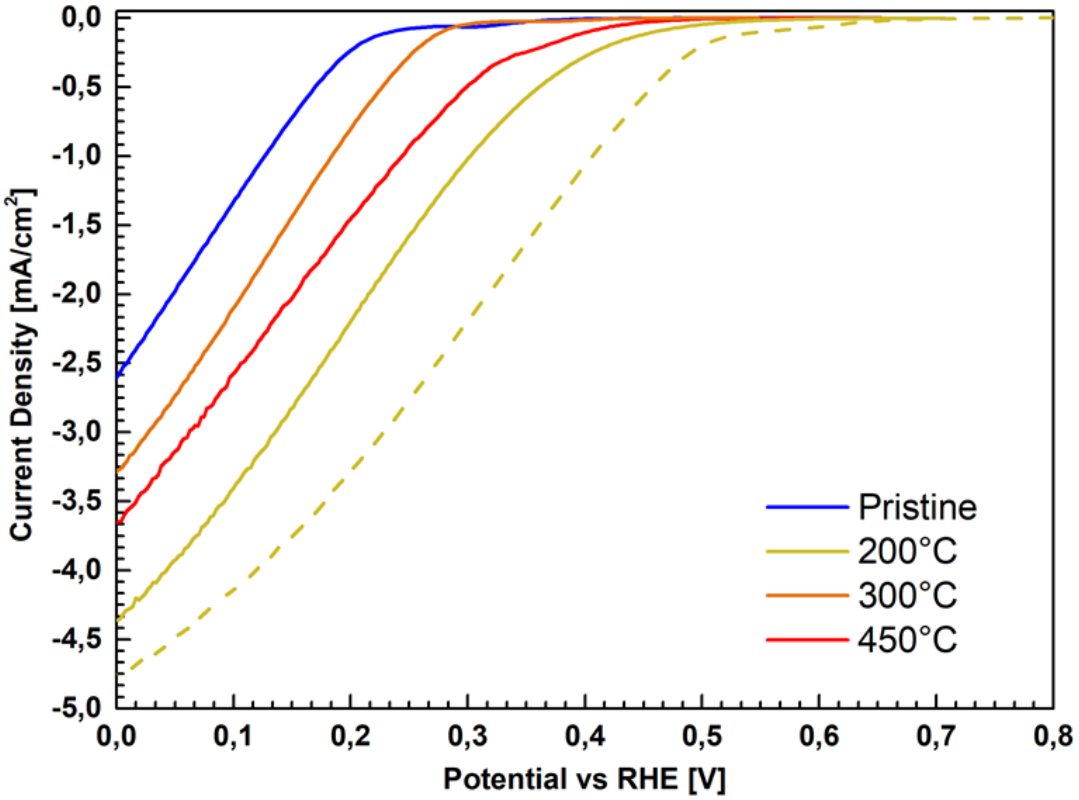

Figure 35: Polarization curves of the HPCs which employ WSe_2 pristine or annealed. The colour coding refers to the characteristics of the WSe_2 HSL as described in the legend. Solid lines are for vacuum annealed films, dashed line N_2 annealed film. The BHJ, ESL and catalyst are identical for each condition.

The behaviour of the architectures realized with annealed WSe_2 films exhibits a non-linear increasing trend. Nevertheless, they all perform better than the pristine condition, confirming the efficacy of the thermal treatment. First, I'll comment the performance of HPC realized with vacuum annealed HSL (solid lines), to then discuss the difference in performance between vacuum and N_2 annealed films (dashed line). From the most to the least effective architecture, the best performing is the one employing the 200°C, 450°C and 300°C annealed HSL. This partially confirm the hypothesis, as the best performances are achieved where the better energy offset between CB-VB of the HSL and HOMO-LUMO of the polymer is expected. The information gathered from the Raman spectroscopy will be used to clarify the difference in performances between the 450°C and 300°C HSL-based devices. The film annealed at 450°C is expected to have the reorganized in the 2H semiconducting phase, while the 300°C should exhibit an almost completely stabilized 1T metallic phase. The semiconducting phase band gap, as from the UV-Vis analysis, points out to a more ordered band structure. This could offer a lower-resistance path for the extraction of photogenerated charges, as less defects are present to cause undesired recombination. On the other hand, if partial amorphous/not completely crystallized clusters are present in the 300°C HSL they

will disrupt the periodicity of the crystal lattice leading to the formation of mid-gap states which can trap charges.

Provided that the best performing architecture is the one employing the 200°C annealed HSL, I'll now discuss the influence of the annealing atmosphere on the performances obtained on the full devices. As it can be seen, there is an appreciable improvement on the delivered photocurrent at 0 V_{RHE} (4.4 mA/cm^2 vs 4.75 mA/cm^2) when the annealing is performed in N_2 atmosphere (dashed line in Figure 35). More interestingly, the polarization curve shows an anodic shift of 100 mV (averaged on the whole potential range) which is even more pronounced close to the onset potential. Additionally, an increase in V_{OC} (0.72 V_{RHE} vs 0.79 V_{RHE}) is obtained for N_2 annealed films.

This effect can be closely correlated with the difference in measured work function of the material. Indeed, an appreciable difference is recorded between the two conditions (4.46 eV in vacuum and 4.74 eV in N_2). The deeper work function obtained under N_2 atmosphere suggests that the material is still heavily p-doped due to the presence of excess selenium, yet it has a remarkably more ordered structure due to the thermally induced reorganization when compared to the pristine film. The net effect is that the material displays an enhanced charge collection efficiency when it comes to holes extraction from the BHJ which arises from its p-type properties. The annealing is also thought to induce a structural reorganization which effectively reduces the series resistance (this effect is consistent on all the annealed films) allowing for a reduction of the voltage losses. This ultimately results in an anodic shift of the HPC polarization curve which, in the best case, is of 300 mV (when compared to the pristine condition). Similarly, almost a twofold increase in photocurrent has been achieved.

The results discussed so far have a twofold relevance. From the point of view of the WSe_2 itself, it confirms that starting from an amorphous thin film obtained via PLD it is possible to tune its properties freely in terms of desired phase, optical absorption and work function through an easily controllable thermal treatment. The photoelectrochemical characterization of the HPC highlighted the close correlation between the suggested HSL properties and the final device performances, confirming the hypothesis. Eventually, the newly designed architecture benefits of the electrochemical stability of the HSL and its tuneable charge selective properties. While the overall performances of this devices are lower when compared to the CuI-based HPC, they still represent a substantial improvement with respect to previous examples like the one obtained in the past where WO_3 was employed as HSL[126]. Provided that (quoting a famous commercial) "Power is nothing without control" [127] these results represent an efficient compromise which allows to realize an architecture in which all its components are

intrinsically stable and still capable of delivering high photoelectrochemical performances.

4.4.2 ESL/catalyst Mechanical stability optimization

Figure 36: Picture of a HPC during operation. On its surface, H_2 bubbles can be seen.

The polarization curves allowed to confirm that, at least from an energetic point of view, the device is working as it should. From a naked-eye observation, it is possible to further assess that when the HPC is polarized at 0 V_{RHE} vigorous H_2 evolution is occurring at the catalyst interface. This can be seen also from the picture (Figure 36) in which the HPC active area is covered in H_2 bubbles. Nevertheless, these hydrogen bubbles prompted the need to solve an additional problem which was severely affecting the stability of these devices.

While performing chronoamperometry at 0 V_{RHE} of applied potential, a sharp decrease in photocurrent was recorded in the initial 15 minutes of the measure. This is shown in Figure 37.a, where the time dependence of the normalized current density is shown (J_0 = 4.56 mA/cm^2). When the potential is applied, almost 40% of the initial value is lost after about 1 minute from the start of the measurement. The kinetic of this phenomenon decreases, eventually settling after 15 minutes. As previously suggested, this is tied to the evolution of H_2 bubbles. The hypothesis is that the initial photocurrent decrease is a convolution of two phenomena. The first is a temporary reduction of the active area due the H_2 bubbles accumulation on the surface. When bubbles fail to release from catalyst, they create an effective gap which separates the electrolyte from the surface of the device. On that area, no further H_2 evolution can take place until the bubble reaches a critical dimension and detaches from the surface. Thus, this causes a reduction of the effective active area which leads to the decrease in photocurrent with respect to the nominal active area. The second effect arises when bubbles are released from the surface. Provided that they reach an appreciable dimension (as shown in the picture), the cavitation force which is generated when they detach from the surface may locally overcome the mechanical resistance of the TiO_2/Pt interface. This leads to a Pt loss which in turn causes a permanent reduction of the effective active area.

To support these hypotheses, a series of pictures of the device surface at different times and on multiple samples was acquired. The images have been processed using ImageJ, evaluating the effective active area as the difference between the nominal active area (the one defined by the mask) minus the projected area of the H_2 bubbles at the time of the picture. These data are shown in the box-plot in Figure 37.b.

A close correlation between the photocurrent and effective active area decrease over time can be highlighted. Thus, the main reason which leads to the HPC performance loss is, indeed, the formation and release of H_2 bubbles.

This issue had also been reported in the publication of the HPC developed by Comas et al.[40]. Both the current architecture and the one presented in the publication share the same ESL/catalyst materials (TiO_2 and Pt) processed via PLD and Magnetron sputtering respectively. Through SEM imaging, they managed to

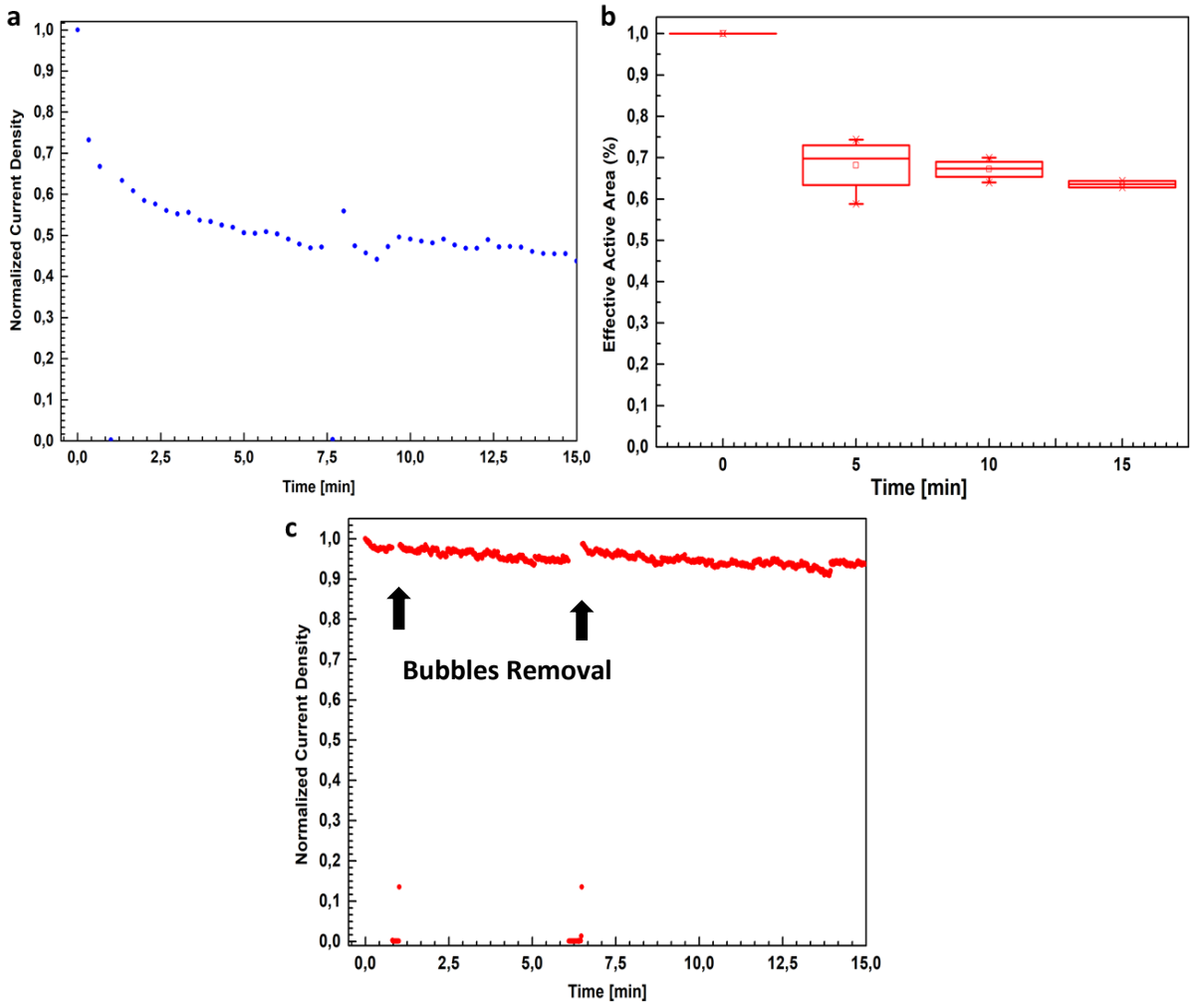

Figure 37: (a) CA of a HPC employing Pt as a catalyst displaying a sudden decrease at the very beginning of the measurement and its correlation with the reduction of effective active area due to bubbles formation (b). (c) suppression of this effect replacing Pt with RuO_2 shown in a CA measure. The sudden drops of current correspond to bubbles removal, granting the mechanical integrity of the ESL/catalyst interface.

resolve areas of the device surface in which, after the measurement, portions of the ESL were left uncovered due to Pt detachment.

Provided that the ESL has been engineered to achieve the highest possible active area, it was necessary to identify a new route which allows to deposit a thin catalyst layer with superior mechanical stability. After a careful literature review, it was decided to use photoassisted electrodeposition (PAED) and to replace Pt with RuO_2 as a catalyst. This approach has been used to deposit RuO_2 HER catalyst on inorganic photocathodes[128]. The pros of this method are firstly that it is possible to exert high control on the final thickness, which is controlled through the deposition time and voltage. Secondly, thanks to the high availability of binding sites offered by the nanostructured TiO_2 layer, a high mechanical adhesion between these two layers was expected.

The photoassisted electrodeposition process was tuned to obtain a 4 nm thick RuO_2 catalyst layer on top of the TiO_2 ESL. The details of the process are provided in Section 7.1.8. The results, shown in Figure 37.c, confirmed that by replacing p-DC MS Platinum with PAED ruthenium dioxide the sharp photocurrent loss at the very beginning of the measurements has been suppressed. Indeed, the normalized photocurrent value remained unchanged irrespective of H_2 bubbles formation, suggesting that this interface is also more prone to favour bubbles release. Eventually, the mechanical stability of the ESL/Catalyst interface has been confirmed, as demonstrated by the complete recovery of the initial photocurrent value after that the accumulated H_2 bubbles have been removed as highlighted on the plot.

Having suppressed the effective active area loss, which in turn lead to a not-steady-state behaviour of the HPC, not only confirms the intrinsic stability of the device but it additionally opens up to the possibility of performing in-depth spectroscopic analysis on this newly designed architecture.

4.5 Spectroscopic characterization

Several spectroscopic techniques can be employed to probe the charge carrier-related processes occurring throughout the multi-layered architecture. However, the stability of the system is a *sine qua non* condition to perform these analyses. Indeed, in order for these measurements to be reliable, the whole system must be at a steady state -i.e. the output signal (current or voltage) must be linearly dependent on the input signal. If the output accounts also for other processes (like a current related to an electrochemical degradation), the analysis cannot be considered consistent.

Provided that the carried-out optimization granted a stability window of at least 15 minutes, it is possible to move forward to perform this analysis. In the following sections, intensity modulated photocurrent/photovoltage spectroscopy (IMPS/IMVS) and electrochemical impedance spectroscopy (EIS) are going to be discussed. This will deepen further the knowledge of how the system behaves, also retrieving some useful insights to further optimize this structure.

4.5.1 IMPS – IMVS

The first two spectroscopic techniques that are going to be discussed are IMPS and IMVS. They are performed at short circuit condition and open circuit condition respectively. By means of an intensity modulated light source, the complex response is recorded from which it is possible to obtain the average characteristic time for charge carrier diffusion within the structure (τ_d from IMPS) and the average characteristic time of photogenerated charge recombination (τ_{rec} from IMVS).

Ideally, a highly efficient architecture should have a short τ_d and a long τ_{rec}. The first, meaning that charges can be rapidly extracted from the BHJ minimizing the chance of recombination. The second, meaning that the photogenerated charges lifetime before that they spontaneously recombine is enough for them to diffuse and be extracted from the selective contacts.

The light source (590 nm) has been selected to fall in the main absorption region of BHJ, ensuring that photogenerated carriers originate only from this layer.

The data corresponding to the IMPS and IMVS measurements are shown in Figure 38.a and Figure 38.b respectively. From this plot, the most straightforward

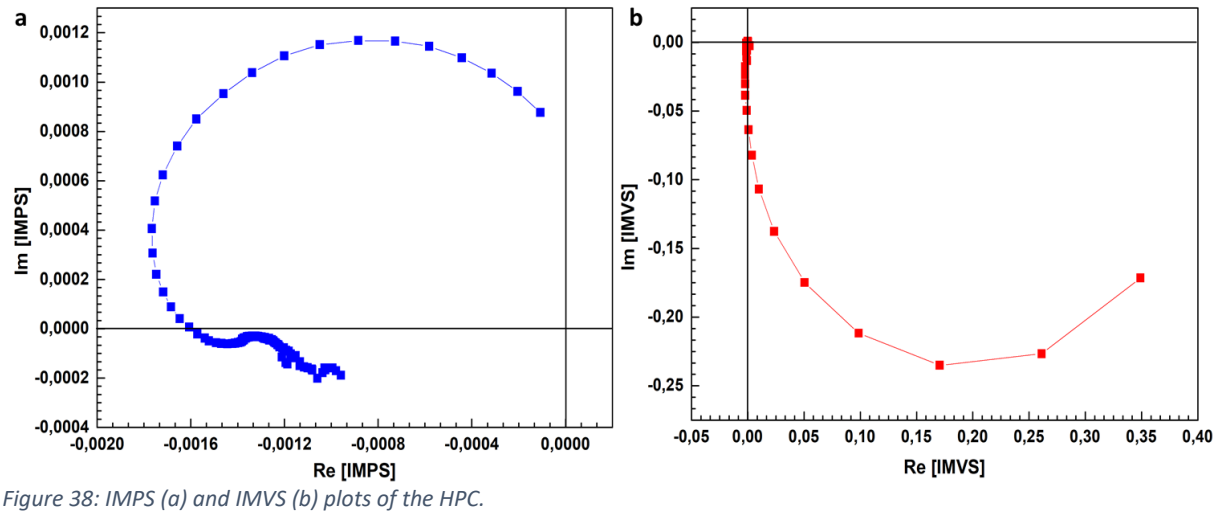

Figure 38: IMPS (a) and IMVS (b) plots of the HPC.

information can be obtained from the characteristic frequency at which the maximum of the plot occurs. They are 51.4 kHz and 20.6 kHz for IMPS and IMVS respectively. The corresponding τ_d and τ_{rec} are $3.09\,\mu s$ and $7.7\,\mu s$ respectively. These data can be compared with those obtained from the device realized by Comas et al. For that architecture, τ_d was 19 μs and τ_{rec} 167 μs. Ultimately, the charge collection efficiency ($\eta_{CC} = 1 - \frac{\tau_d}{\tau_{rec}}$) is 59.8% vs 88% for the current and previous architecture respectively.

As evident from a direct comparison of the data, the reason for the lower η_{CC} has to be addressed to the shorter recombination time. This means that photogenerated charges within the BHJ recombine faster in the new device rather than in the reference one. Thus, it can be inferred that, in order to extend τ_{rec}, a dedicated optimization of the BHJ formulation and processing is necessary. On the other hand, the diffusion time of the newly designed architecture is more than 6 times faster than the previous example. This corroborates the idea that this device has a suitable energetic structure which facilitates charge flow across the different layers. Additionally, the portion of data in the low frequency range of the IMPS plot suggests that a factor which is negatively affecting the performance of the devices is the formation of recombination centres[129]. These recombination centres are likely to be located or within the BHJ itself (as suggested also from the IMVS data) or in the ESL layer. The ESL, being a sub-stoichiometric oxide, may have unsaturated bonds which lead to the formation of trap sites, thus leading to photogenerated charges recombination.

An interesting outcome of this analysis is that, to boost the performances of the HPC, there is large room for improvement when it comes to replacing the current BHJ. This bodes well for the possibility of integrating novel organic semiconductors to design improved HPC.

4.5.2 EIS

Another powerful tool which allows to decouple frequency related processes is electrochemical impedance spectroscopy. This technique is also usually employed to study solar cells and understand how the minority carriers-related processes affect the overall device efficiency. In this section the behaviour of the newly developed HPC will be investigated trying to elucidate how the flow of photogenerated charge carriers takes place in the multi-layered architecture. However, the analysis of this kind of device is far from being trivial. To perform this task, it is necessary to identify the expected charge carrier related processes taking place in the architecture of interest under the specific experimental

conditions. Extensive work is this direction allowed to model and understand the behaviour of several photoelectrochemical systems, mainly based on metal oxides photoelectrodes both in single or multi-layered configuration [130–133]. Only recently some very first examples have seen the application of this technique to the world of organic based photoelectrodes[36] to understand how charge accumulation within the BHJ due to poor electron injection at the electrolyte interface could increase the degradation rate of the device. Here this analysis will be extended to the overall HPC behaviour following an approach recently adopted for multi-layered inorganic photoelectrodes[132].

Differently than the previously described spectroscopic techniques, here the modulated input signal is the potential or the current, whether it is in potentiostatic or galvanostaic mode. In this case, the response of the material was investigated as a function of the modulated potential at 0 V_{RHE}. This will allow to gain insights on the charge transfer processes occurring across the different layers and at the catalyst-electrolyte boundary. In order to access this information, the experimental data will be fitted employing an electrical equivalent circuit, which will be designed to represent the charge related processes occurring in the device.

The description of these processes has been discussed in detail in the previous chapters, herein they will be briefly recalled framing the employed equivalent circuit.

A first fundamental step is represented by the electron injection from the HPC to the electrolyte, which takes place across the catalyst-electrolyte interface and describes the H_2 evolution process. An additional element is needed to describe the photogeneration process within the BHJ, where charges experience a resistance which prevents them to recombine (thus, the higher the better). These photogenerated charges are extracted through the selective contacts. These steps thus require two additional elements to be included in the circuit. Overall, 4 elements are needed in order to represents the complete charge flow across the photocathode plus an additional one, representing the ohmic losses of the system. The 4 charge transfers occurring at the interfaces of the multi-layered architecture are represented through a resistance in parallel with a capacitor. The capacitor is often replaced with a constant phase element (CPE) which accounts for deviations from the ideal behaviour through an exponent which can take values between 0 and 1. An ideal capacitor is described by the value “1” while an ideal resistor by

the value "0". The resulting circuit is shown in Figure 39 alongside with the Nyquist Plot representing the experimental results (blue dots), while the result of the fitting is shown as the solid line which closely matches the experimental data ($\chi^2 \approx 0.01$; Error >2% only in the low frequency range due to noise in the measurement).

Recalling the previously mentioned processes, the first resistance accounts for the ohmic losses of the system. The second and the fourth elements describe the charge injection at the hole and electron selective layers, respectively. The third element models the BHJ recombination resistance, while the last element represents the charge transfer across the catalyst/electrolyte interface.

For each element, the normalized resistance and the apparent capacitance obtained from the fitting are shown in Table 5. As for the third element, it has as expected the highest value of resistance and a low value of capacitance, suggesting that minimal charge accumulation is taking place on this layer. On the charge injection side (second and fourth elements), a slight asymmetry can be highlighted. On the holes side, both a lower resistance and a much lower capacitance are measured when compared to the electron selective side. This suggests that while the WSe_2 hole selective layer is working efficiently to selectively extract charges, exhibiting a low resistance and minimal charge accumulation, the TiO_2 layer may be limiting the efficiency both in terms or resistance and charge accumulation, confirming what previously suggested from

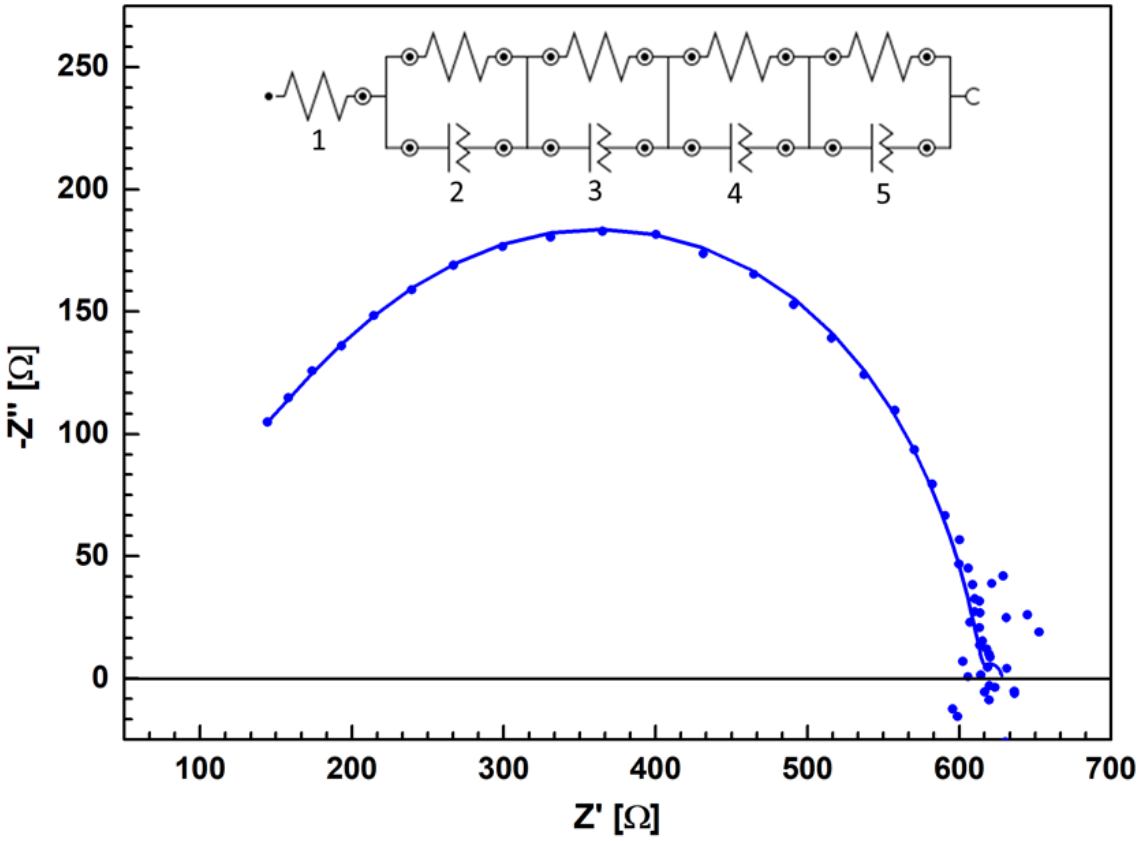

Figure 39: EIS Nyquist plot recorded at 0 V_{RHE} under illumination on the HPC. In the figure, the equivalent circuit employed is reported.

the IMPS analysis. Eventually, the fifth element has, as expected, the lower resistance of the series. This is strongly related to the high catalytic efficiency of the RuO_2 catalyst layer. Additionally, the high value of capacitance arises from the high amount of e^- that are attracted toward the surface by the reacting species accumulated at this interface which are participating to the hydrogen evolution reaction.

Table 5: Parameters obtained from fitting the EIS with the equivalent circuit reported in Figure 39.

Element	*1*	*2*	*3*	*4*	*5*
R [Ωcm^2]	**5.4**	**13.3**	**74.3**	**17.8**	**2**
C_{APP} [F/cm^2]		**$9*10^{-10}$**	**$2.6*10^{-9}$**	**$4.89*10^{-8}$**	**$3.1*10^{-4}$**

It is worth highlighting that the interpretation proposed so far combines the information gathered through the whole optimization process of the HPC, which has been done in view of highlighting the contribution of each layer on the overall device efficiency. Other circuits might be employed to fit the data previously shown, eventually shifting the focus to the behaviour of the device rather than breaking up the contributions coming from the individual layers. This could have been done, for example, collapsing all the 4 R-CPE into a single element where the overall resistance would have represented the charge transfer resistance of the whole device. Further evidence supporting the view presented in this section could be retrieved performing additional experiments varying the applied potential and evaluating how each element changes, following the examples recently reported in literature [132].

Nevertheless, the outcome of this analysis suggests that the rate-limiting element when it comes to charge transport can be traced to the TiO_2 ESL, while the HSL is no longer the bottleneck. Several promising candidates are available to replace TiO_2, but they are mainly limited from their electrochemical stability pH window. As it shall be shortly seen, an interesting feature of the newly developed architecture may ease the way toward this goal.

4.6 Photoelectrochemical stability – pH and time

As previously stated, the relevance of optimizing an architecture which combines a substantial time stability, ideally over a wide pH window, comes handy in many

respects. Firstly, when it comes to integrating a HPC in a full tandem system (i.e. coupled with additional elements like a photoanode or a PV-biased OER catalyst) time stability allows to ensure a proper functioning of the stack. It also allows to draw from a wider pool of material (mainly metal oxides) to be employed as selective contacts in these architectures, like NiO, SnO_2 or ZnO. On the other hand, the possibility of operating at pH other than acid (neutral or ideally basic) allows to facilitate the oxygen evolution reaction, which occurs with a sluggish kinetic than its cathodic counterpart. Furthermore, avoiding acidifying the electrolyte poses minor health- and safety-related hazards and it is more economically feasible.

This topic has been thoroughly investigated by Naito et al.[134], identifying buffered pH 7 electrolytes as a good compromise in terms of cost-performances for water-electrolysis systems. Based on this premises, the performances of the HPC were evaluated in pH 7 Na-phosphate buffered solution to check the performance retention beyond the acidic range. In Figure 40, the comparison of the LSV of the WSe_2/PCDTBT:PC70BM/TiO_2/RuO_2 HPC performed at pH 1 and pH 6.9 are shown. For each condition a total of 4 samples have been measured belonging to the same fabrication batch. Each curve is representative of the champion device measured in each condition, hoping to provide an encouraging perspective on this outcome. Remarkably, this architecture shows an excellent performance retention in the two different pH conditions both from the photovoltage point of view and from the current density at 0 V_{RHE}. When compared to literature, this is the very first

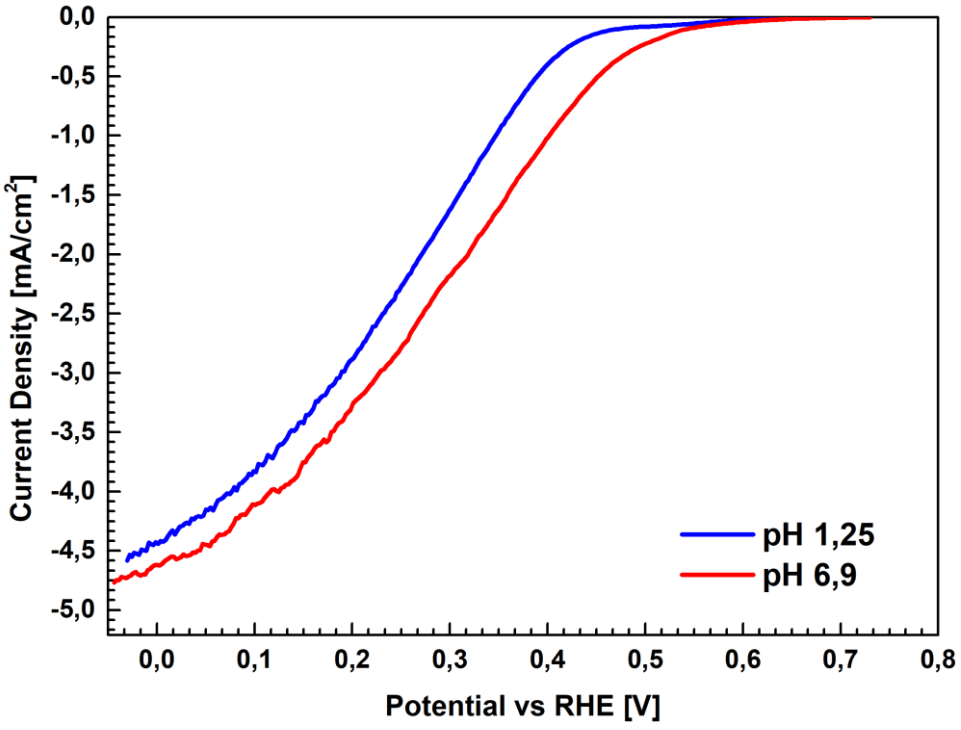

Figure 40: Polarization curve of a HPC (ITO/WSe_2/PCDTBT:PC70BM/TiO_2/RuO_2) in acid (blue curve) and neutral pH (red curve)

demonstration of a HPC which can operate with equal efficiency in the investigated pH range[34], thus corroborating the validity of the optimization approach.

This analysis can be concluded discussing the extended stability measurement of this architecture, as shown in Figure 41. This measurement has been performed at 0 V_{RHE} of applied potential at pH 1.25. This condition was selected since it allows for an easier comparison with existing work in literature. It is clear that the dedicated materials research and device engineering allowed to significantly extend the operational stability of this architecture both when compared to the CuI based HPC[40] and also to the WO_3 based one[126]. Indeed, complete recovery of the photocurrent has been achieved for until 4 hours of continuous measurement when bubbles were removed from the surface and when partial solution refreshment was performed. Afterwards, a slow decaying of the photocurrent is reported, which leads to halving the initial current density value after 11 hours. Eventually, the measurement is stopped when the current density dropped below 1 mA/cm^2.

To gain more insights on this phenomenon, we shall look up to some recently published papers in which in depth investigation and optimization of HPC

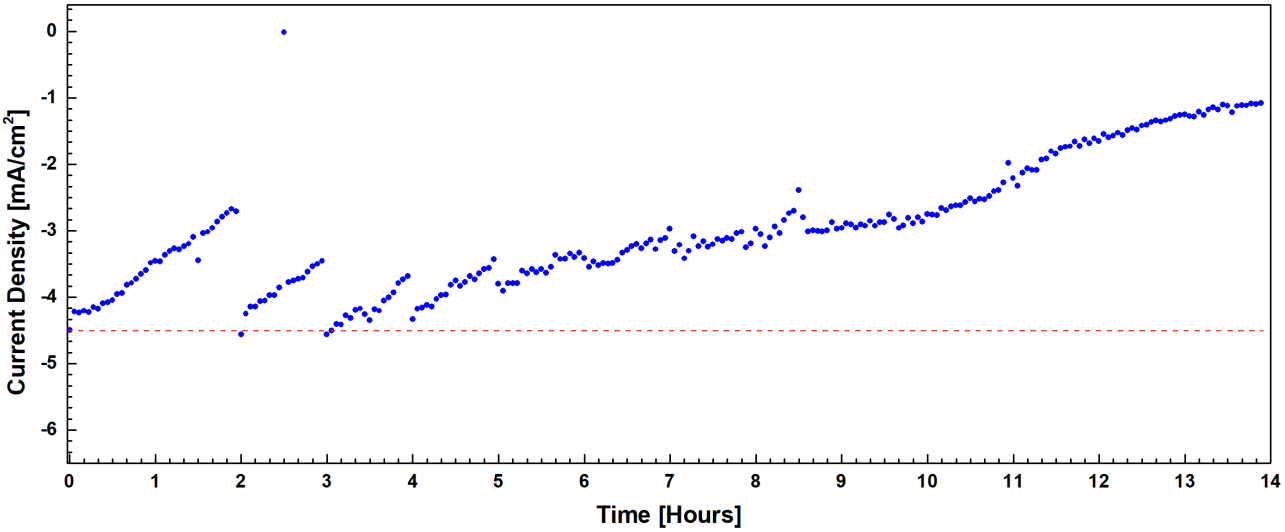

Figure 41: extended chronoamperometry of a HPC at 0 V_{RHE}. The dotted red line identifies the initial value of current.

architectures allowed to achieve extended operational stability[36]. In this example, Yao and co. workers demonstrated showed that fullerene acceptors were the main cause of degradation of HPC and that charge accumulation within the BHJ lead to an accelerated and unrecoverable degradation kinetic. Based on the results discussed so far, it was demonstrated that stable devices can be obtained also when fullerene acceptors are present in the BHJ. While this is partially in disagreement with their findings the fact that ineffective charge extraction from the photoactive layer may cause an enhanced degradation is fully in accordance with the present data, as thoroughly discussed in this work. Indeed, it is suggested that this may be the cause of the slow decaying photocurrent profile of the current

architecture, where charge accumulation at the interface with the ESL is thought to be the rate-determining process. By combining these findings, the stability issue of HPC can be solved once and for all.

4.7 Conclusions

To summarize the efforts committed to the realization of a stable, high performing hybrid organic-inorganic photocathode, the most relevant take home messages will be highlighted, emphasizing the relevance of cross-disciplinary applications of these findings.

From a purely materials-engineering related point of view, a comprehensive view of how to fabricate, optimize and characterize WSe_2 thin films deposited via physical vapour deposition was offered. The tools to assess its structure, interpret its properties and tune them according to the needs of the desired application were also provided. As for the field of HOPEC-WS, it was made possible to access a structurally ordered with preferential 1T phase, intrinsically p-doped material with excellent hole transport properties and suitable work function alignment. This can further serve as guideline, which information can be used also to engineer other TMDs compounds in a similar fashion.

It was also demonstrated that, by replacing P3HT:PCBM with PCDTBT:PC70BM and optimizing the ESL and catalyst layer, the newly designed architecture successfully combined efficient hydrogen generation by direct conversion of sunlight with a remarkable stability. This further allowed to access useful information through spectroscopic techniques, which highlighted a dedicated optimization of the ESL and eventually of the BHJ would lead to a further improvement of the device performances.

Finally, the optimized architecture stability was demonstrated through extended chronoamperometric measurement achieving a hydrogen evolution related photocurrent in excess of 14 hours. Remarkably, photoelectrochemical performance retention has been demonstrated for devices operated both in acidic and neutral environment. The relevance of this results allows to envisage a high stability and efficiency full tandem system which, thanks to this interesting feature, could be designed to operate at neutral pH, with positive impact on the overall reaction kinetic of the system and with an eye on the technological feasibility of this technology.

Chapter 5
A Broader Outlook on Solar Conversion Technologies

An interesting aspect of the so far presented results it that they can potentially be translated to several closely related fields. To this extent, the following discussion will focus on how the knowledge gained on developing stable and efficient HPC can have positive outcomes also in the akin field of solar cells. In particular, taking as in inspiration the work done with the HPC-PSC tandem, some innovative strategies will be presented in which PSC stability toward harsh conditions can be enhanced by exploiting engineered selective contacts.

From the cross-disciplinary interaction between these two fields it will be possible to have a mutual benefit, as both are committed to the same goal of promoting a sustainable energy transition.

5.1 Engineered HSL for Moisture Resistant PSC

Perovskite solar cells efficiencies experienced a steady increase over the years, and several start-ups and companies are setting up for their large-scale deployment[135]. Nevertheless, the photoactive layer of these devices is highly sensitive to oxygen/humidity exposure[81,135]. Humidity, and water, in particular promote the dissociation of this material, which in turn loses its excellent photogeneration performances. As for many other technologies, the first straightforward approach was to design encapsulation methods which isolate the material from the environment. However, similarly to what was seen for HPC, these efforts have been proven to be inefficient, thus hindering the penetration of this technology to the market[135].

Taking advantage of the knowledge gained on optimizing photoelectrochemical water splitting systems, a novel strategy which can offer an intriguing perspective to stabilize PSC moduli is proposed. This approach aims at designing engineered charge selective contacts which can simultaneously act as charge extractors and moisture neutralizers. By preventing humidity to reach the perovskite layer, the whole device performances will be retained.

In direct solar cell architectures, the first layer which comes in contact with environmental agents is the hole transporting one. Thus, embedding a WS-active material in this layer, it would be possible to locally dissociate water prior that it reaches the photoactive layer. While doing this, ideally the charge selective performances shall not be harmed. The optimization of this layer must therefore address the stability (also from a photoelectrochemical point of view) and the energetic alignment of the materials involved. Also, at least for one of the components involved, a suitable catalytic activity toward water oxidation is desired.

A suitable material which combines the aforementioned requirements is copper thiocyanate (CuSCN). This material has been proven to efficiently catalyse the oxygen evolution reaction when employed in a photocatalytic system, realizing a $BiVO_4$/CuSCN heterostructure[136]. Furthermore, its efficiency as hole selective layer has been demonstrated in several works, in which devices employing this material displayed an enhanced stability[137,138].

In order to ease the processing step, a mixed HSL has been designed. Indeed, CuSCN deposition poses some drawback when solution processing has to be employed. These are mainly related to poor solvent orthogonality with respect to the other layers, which leads to their partial dissolution. To this extent, our collaborators optimized a continuous flow hydrothermal synthesis process which allowed to obtain CuSCN in the form of ligand-free nanoplatelets (CuSCN-NP). These CuSCN-NP have been then dispersed in a P3HT polymeric matrix, in order to obtain an easily processable, homogeneous film (further details on the process can be found at [74]). Being P3HT a deeply investigated and cheap p-type polymer, the resulting film is expected to efficiently behave as hole selective layer. Furthermore, given its the suitable energetic alignment with the CuSCN valence band, the charge transfer within the composite matrix should be favoured.

In the following sections, the performances of PSC based on the so obtained CuSCN@P3HT composite hole transporting material (HTM) will be assessed and compared to those employing pure P3HT HSL. The focus shall be set on discussing the performance retention of PSC exposed to high-RH environment, aiming at elucidating the influence of CuSCN species on moisture neutralization. Furthermore, the suggested mechanism of stabilization will be discussed in detail, highlighting the guidelines to efficiently exploit this new approach.

5.1.1 Water Splitting Active HSL

While in the published paper[74] many details on the characterization, fabrication and optimization of the CuSCN@P3HT composite are reported, herein the attention will be focussed on the catalytic behaviour of the best performing combination. Afterwards the discussion will be moved on how this behaviour dictates the stabilization mechanism on the full PSC.

The optimized composite employs a dispersion of CuSCN-NP 5 wt.% in P3HT. While assessing its water splitting behaviour, the attention was focussed on the anodic reaction, where CuSCN is expected to play a role due to its favourable energetic structure and to the cathodic one. It is further expected that, given the morphology of this material, the amount of active sites available on the edges of the nanoplatelets could have a substantial impact on the electrochemical performances. To make this analysis as close as possible to the real working conditions the full device (ITO/SnO_2/perovskite/HTM/Au) was "split-up", realizing half device architecture (HTM/Au/ITO) so that the HTM is directly in contact with the electrolyte. Both the CuSCN@P3HT composite and the bare P3HT control sample will be defined as HTM.

The OER/HER performances are investigated by means of a 3-electrode configuration linear sweep voltammetry in a pH 7, 0.1M Phosphate Buffer solution, both in dark and under illumination. On the anodic side, no photo-enhancement effect is recorded, as it can be seen in Figure 42 where for both HTMs light and dark regime are alternated each 0.05 V. Nevertheless, the neat and composite material display a remarkably different behaviour. In terms of overpotential, the CuSCN@P3HT HTM has an onset 0.2 V more cathodic than the neat HTM. Furthermore, the current density is two orders of magnitude higher when CuSCN is present in the film. This suggests that the addition of CuSCN has a positive impact on the catalytic efficiency of the HTM when it comes to promote the OER.

Additional differences arise on the cathodic side of the reaction. Since the energetic of the system is now suitably aligned with the reaction potential, the effect of photogenerated charges is now appreciable in both conditions (Figure 43.a and 43.b). Thus, provided that a fraction of residual photons can reach the HTM after passing through the photoactive layer, they can provide an additional photovoltage which can add up to the one coming from perovskite itself. This will further reduce the potential required for the water splitting reaction to occur. This can be taken

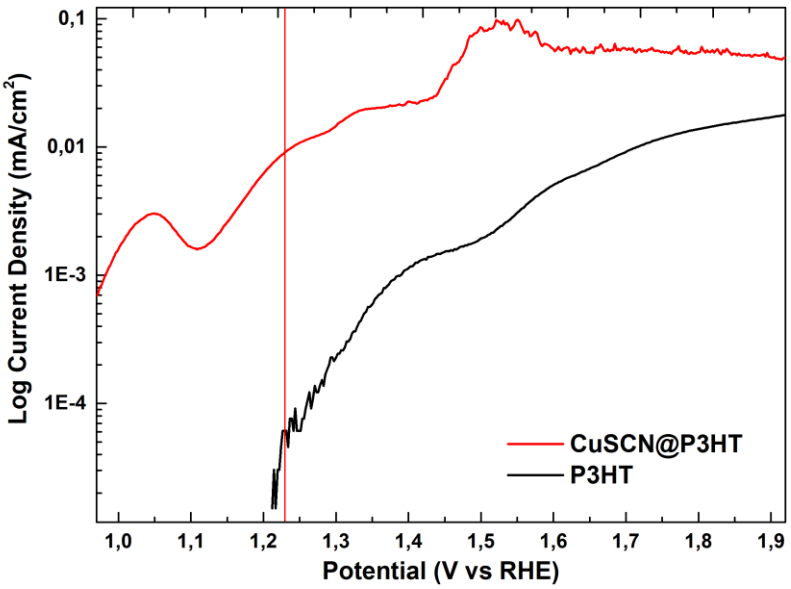

Figure 42: Anodic polarization curves of the neat P3HT and CuSCN@P3HT HTM. Both the measurements are performed under alternated light/dark regime. The vertical red line identifies the O_2 evolution potential. Ref [74].

as true even if the effect in the full PSC will not be as pronounced as what seen here. Furthermore, a different behaviour is reported depending on the presence of molecular oxygen dissolved in the solution. These species are always present in solutions exposed to atmosphere, and their concentration depends mainly on the nature of the electrolyte and its temperature. To work in de-aerated condition, the electrolyte is typically purged with N_2 for at least 20 minutes, so that O_2 is stripped away. When no molecular oxygen is present, the behaviour of the neat and composite HTM are comparable down to -0.1 V_{RHE}. At potential more negative than this threshold value, a catalytic onset can be identified in the CuSCN@P3HT HTM, which points out that the addition of CuSCN favours the HER as well. The neat P3HT film does not display an HER onset in the potential region of the LSV.

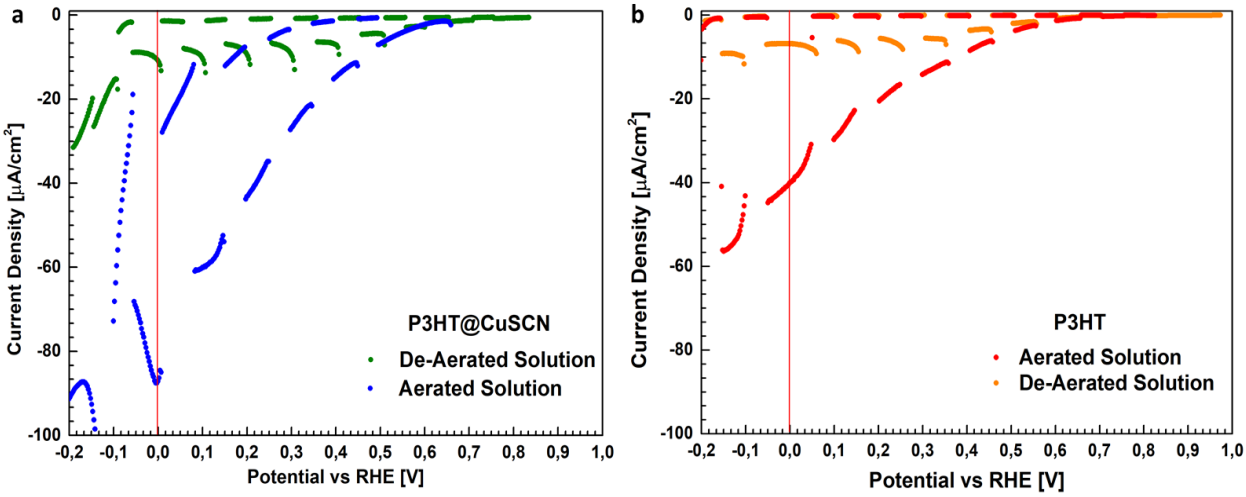

Figure 43: Cathodic polarization curves of the neat P3HT and CuSCN@P3HT HTM in aerated/de-aerated solution. Both the measurements are performed under alternated light/dark regime. The vertical red lines identify the H_2 evolution potential.

When no purging step is performed, thus allowing molecular oxygen to be dissolved in the solution up to its equilibrium concentration, a different light-induced interaction arises. For the composite film, an increase in current density is reported both in light and in dark conditions. The magnitude of the photo-enhancement in aerated condition is proportional to the increase in current density in dark aerated condition. On the other hand, the current density of the neat film in dark is not affected by the presence of O_2, while it increases with respect to the de-aerated condition when the neat P3HT film is illuminated. The interaction of P3HT with light, when immersed in aerated solutions, has been previously investigated[139]. It has been found that upon illumination, photogenerated charges accumulated at the interface between the polymer film and the electrolyte led to a surface polarization effect which enhances and facilitates the charge transfer process across this interface. When CuSCN is present, it further increases the efficiency of this process, facilitating the charge transfer between the film and the reactants.

After having assessed the anodic and cathodic behaviour of the CuSCN@P3HT composite with respect to the neat P3HT film, it can be concluded that the overall water splitting reaction is favoured by the presence of CuSCN nanoplatelets. This also provides the very first experimental evidence of the WS performances of a composite film employing P3HT and CuSCN. In the overall reaction balance, the anodic steps are those which kinetics and potential are less favourable. However, it has been demonstrated that oxygen in its radical form can induce a p-doping effect in P3HT, which further enhances its hole transport properties. As soon as the second reaction step is reached ($HO^* \rightleftharpoons H^+ + O^* + e^-$), the oxygen atom adsorbed to an electrochemical active site (O^*) is already reactive enough to participate to the doping process. This further eases the potential requirement, as a positive effect shall be reached even at the intermediate steps of the WS reaction.

Prior switching the focus from the pure (photo)electrochemical characterization to the expected behaviour within a PSC, the results can be briefly summarized to give a key of reading for the solar cell integration. Provided that this HTM material has been engineered to prevent moisture to reach the photoactive layer, its enhanced (photo)catalytic behaviour is expected to allow a fraction of the atmospheric humidity to be dissociated into harmless components such as molecular hydrogen or oxygen. Furthermore, reactive oxygen species generated as part of the WS full reaction can also induce a positive p-type doping in the P3HT, with beneficial influence on the full device performances. Overall, this shall contribute to stabilize the performance of a solar cell by preventing moisture to dissociate the photoactive layer material.

When envisaging the translation of these results to the behaviour in a full SC, it must be taken into account that the amount of reagents available are roughly six orders of magnitude lower (taking into account the water content in atmosphere). Thus, while the magnitude of this effect will surely be lower, this mechanism is expected to hold true also in high RH% environment.

5.1.2 High RH% stabilization of PSC

To validate the mechanism suggested in the previous section, the time-dependent performances of two types of PSC will be compared, one employing the composite HTM and a control one with neat P3HT. In these experiments carried out by our collaborators both the architectures are going to be exposed to two different environmental conditions. The first, defined as "dry", in which the PSCs will be stored in glovebox after having characterized their photovoltaic behaviour right after fabrication. The second, in which the PSCs will be stored in a custom-made container with controlled humidity (RH>80%). For both conditions, the devices will be removed from the storage housing and tested at fixed time intervals to assess the evolution of their performances. While a detailed discussion of these results is beyond the scope of this section, the most relevant aspects which are a direct consequence of the previously suggested hypothesis will be discussed. A complete picture can be found in the related published paper [74].

Two parameters which allow to have an insightful perspective on the performance of a solar cell are its PCE and V_{OC}. The first gives an overall description of how the SC performs, while the latter allows to infer how the energetics of the system evolves as a function of the inferred modification taking place at the HTM/Perovskite interface. The endurance tests data for these parameters are shown in Figure 44 both in forward (f) and reverse (r) current-voltage scans.

On the PCE side, it can be seen that the control devices (pure P3HT) show a substantial performance decrease when exposed to high RH condition while negligible degradation occurs if stored in dry. This in consistent with the fact that environmental humidity causes an irreversible degradation of the photoactive layer. By contrast, devices employing the composite CuSCN@P3HT HTM show a much lower performance loss when exposed to humidity. Furthermore, a similar performance loss is seen also on the "dry stored" samples for the composite HTM. This allows to rule out any humidity-dependent degradation of the solar cell, confirming that the addition of CuSCN to the hole transport material efficiently imparts moisture resistance to the whole device. The decrease in PCE of the composite HTM PSC is mainly affected by a decrease in the J_{SC} of the cell. The reason of this has to be traced back to an auxiliary contribution of CuSCN to

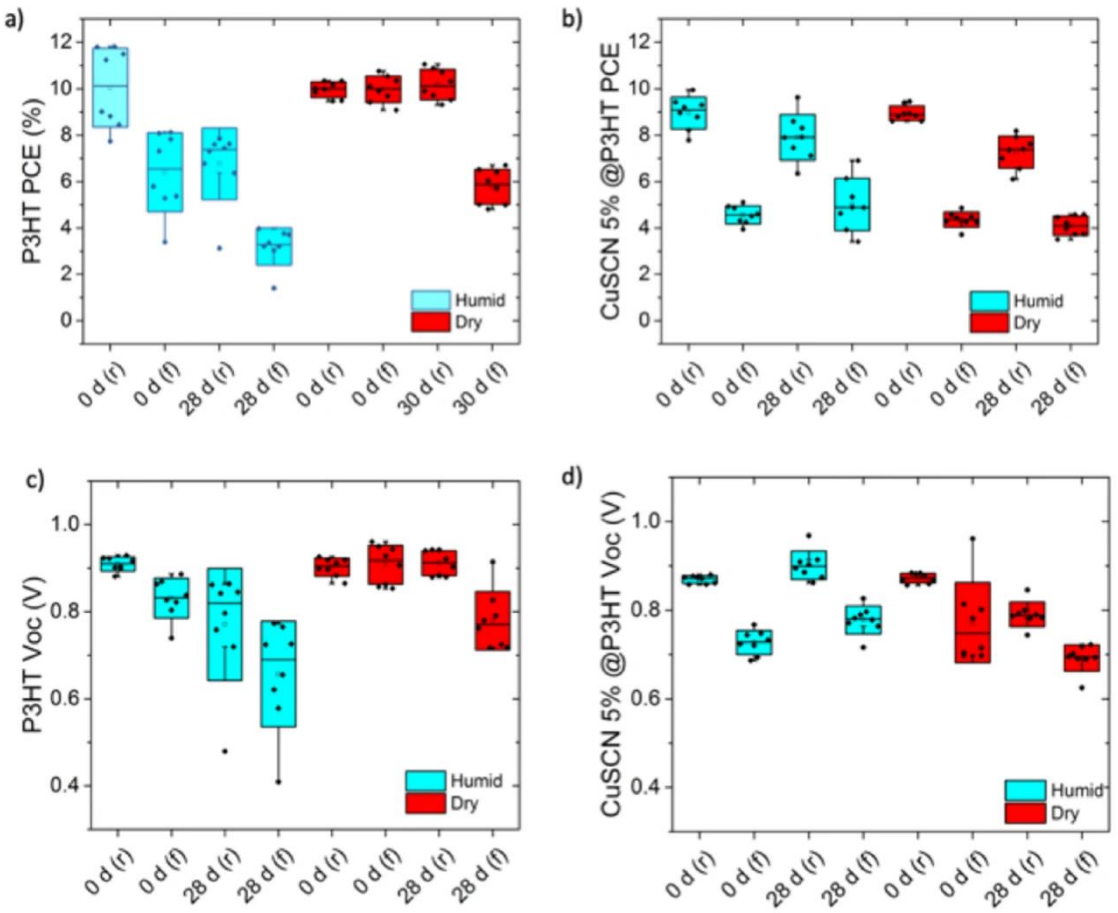

Figure 44: Statistical data on PCE and V_{OC} variations for 28 days for PSC employing the neat P3HT (a and c) or CuSCN@P3HT (b and d) HTM. The colour coding identifies water-saturated or dry atmosphere. Ref [74].

photocurrent generation, harvesting the UV/blue region of the spectra due to the large band gap of this material.

This is also confirmed by the open circuit potential statistical analysis shown in Figure 44.c and 44.d for the neat and composite film respectively. This parameter is found to slightly increase when the composite HTM is employed in high RH atmosphere, suggesting a more suitable energetic alignment at the HTM/perovskite layer as a result of the humidity driven stabilization process. By contrast, when stored in dry atmosphere the V_{OC} of this architecture slightly decreases, confirming that the effect seen on devices stored in high RH% is indeed connected to the occurrence of the suggested stabilization mechanism of moisture prevention and p-doping of the P3HT matrix.

A further evidence of the p-doping process taking place in the HTM is the evolution of the WF of this layer when exposed to high RH% conditions. The value for the film exposed to this ageing condition is of -5.1 eV, which is also suitably aligned with the work function of the gold back contact. This further confirms that charge extraction at this interface is favoured. When comparing these data with the ones acquired on dry-stored samples, the latter displays a large variability (5.2 eV – 4.75 eV) which is addressed to the influence of CuSCN-NP dispersed in the matrix,

leading to a local variation of WF. Overall, being the measured WF of neat P3HT stored in dry equal to 4.8 eV, it can be concluded that the exposure to environmental humidity leads to a p-doping effect in the HTM. The origin of this doping effect is correlated to the formation of oxygen as environmental moisture is dissociated when interacting with this material.

Based on these evidences, one can speculate on how this mechanism takes place within an unsealed PSCs exposed to high RH%. It can be suggested that, simultaneously to the classical PV operating mode (charges collected to the external circuit) a parasitic mechanism occurs on the upper layers, which consumes a fraction of the photogenerated charges to bias the water dissociation. This is schematically depicted in Figure 45, in which the charge transfer steps and the energetic alignment of each layer are shown alongside to the water splitting potentials for the anodic and cathodic reaction. The "parasitic" water splitting reaction is thought to occur as soon as water starts to diffuse through the topmost layers of the device. As photogenerated holes reach a CuSCN active site where an H_2O molecule is bound, it readily oxidises it to yield an oxygen molecule/oxygen reactive specie. This then leads to the p-doping of the adjacent P3HT region. The other half reaction occurs in the interfacial region between the photoactive layer and the HTM. Provided that some positively charged H^+ ions are present in the

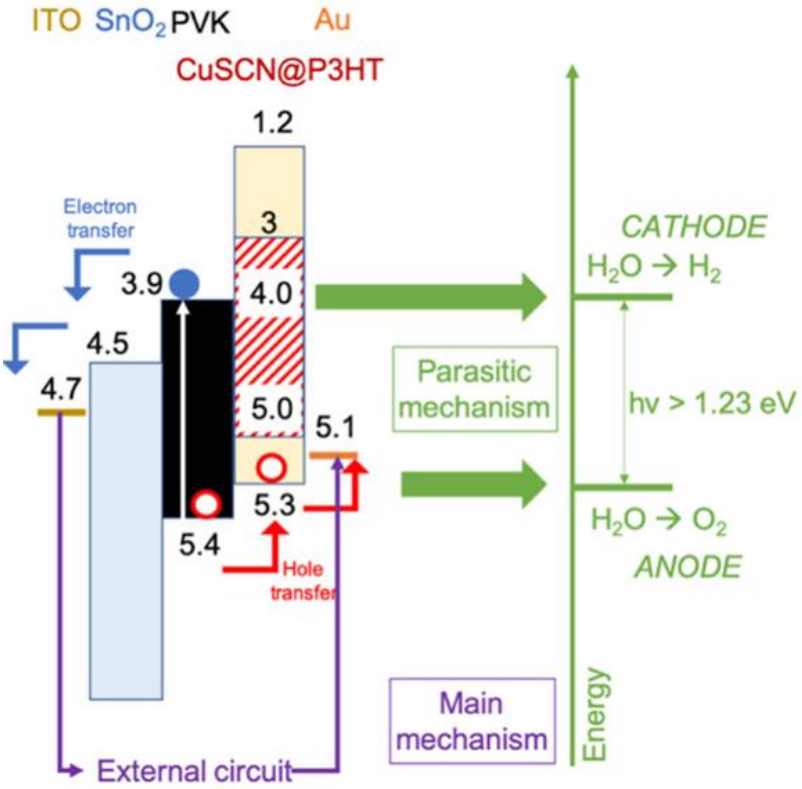

Figure 45: Proposed mechanisms for the two processes happening within the WS-integrating PSC. The "main mechanism" (violet) is the regular working process of the PSC. The "parasitic mechanism" is the suggested WS-process occurring at the perovskite/CuSCN@P3HT interface. Ref [74].

HTM, they can attract a fraction of negatively charged electrons which are photogenerated in the region adjacent to the interface. Since CuSCN has been demonstrated to catalyse also the cathodic reaction, H^+ ions can be reduced to molecular hydrogen once photogenerated electrons diffuse towards the catalytic active site. The net result of this parasitic mechanism is, as suggested, the dissociation of water molecules prior that they can reach the photoactive layer, causing an irreversible degradation. This stabilization effect allowed to retain the performances of the PSC even in high RH% environment for more than 28 days.

5.2 Take Home Messages and Outlooks

This chapter provided a successful demonstration of how moisture resistance can be imparted to unprotected PSCs through engineered hole transport materials embedding water splitting active species. The addition of CuSCN nanoplatelets in a P3HT matrix returned several advantages such as the aforementioned stabilization effect but also a more favourable charge transport properties due to an improved energetic alignment of the HTM with the photoactive layer. This very first demonstration opens up to the possibility of designing novel approaches to stabilize PSCs, without the need of relying on encapsulating strategies, eventually obtaining PSCs which can withstand extended exposure to harsh environment. This further confirms how a synergistic approach between the field of (photo)electrochemistry and solar cells may yield ground-breaking results *via* sharing of mutual knowledge.

Chapter 6

Conclusions

Throughout this thesis, several topics connected to the world of sustainable H_2 production have been addressed. To this extent, the fundamental role of solar energy conversion both through pure photoelectrochemical devices and photovoltaic cells was demonstrated. In particular, organic based devices have been the *leitmotiv* of this work. Their potential at the current state and in the near future has been thoroughly discussed.

The starting ground of this work was the benchmark HPC of Comas et al. [40] which architecture was ITO/CuI/P3HT:PCBM/TiO_2/Pt. To demonstrate how this device could participate in clean hydrogen production, a HPC-PSC tandem has been realized. To this extent, a specific optimization was carried out which returned a new HPC with enhanced transparency and improved performances. In particular, the maximum power point of this newly designed architecture was anodically shifted (3.98 mA/cm^2 – 0.303 V_{RHE} and 4.6 mA/cm^2 – 0.33 V_{RHE} for the reference and optimized devices respectively), thus favouring the integration in the tandem stack. This tandem retuned the very first evidence of substantial water splitting from fully organic-based devices with 2.03% STH efficiency. To fill the gap with other, widely investigated, inorganic systems a sensitivity analysis has been performed with the final aim of identifying the most efficient way to perform a targeted optimization to increase the performances of the HPC. The outcome of this investigation pinpointed some useful information which allowed to envisage a performance increase for this kind of system to 10% STH in short term and 20% STH in long term perspective. The main focus should be set on identifying novel organic semiconductors which could return lower voltage losses and increased photocurrent generation. This is a topic which is already returning promising results in the akin field of OPV, allowing to reach PCE above 15%. Additionally, specific selective layers design and optimization is desired in order to minimized undesired series resistances and simultaneously extend the HPC lifetime by selecting intrinsically electrochemically stable materials.

This prompted the development of a newly designed architecture which takes into account the guidelines retrieved from the sensitivity analysis performed on the HPC-PSC tandem. To ensure the stability of the device, a WSe_2 based HSL has been investigated and optimized. Its superior electrochemical stability, suitable

charge transport properties and tuneable optoelectronic structure greatly fitted the need of this specific application. Through a thermally controlled phase transition process, it was possible to selectively access the 1T', 1T and 2H phase of the material. Furthermore, tuning the annealing atmosphere, a best condition was identified which combined a suitable work function, a correct energetic alignment with many semiconducting polymers and an enhanced p-type behaviour. This allowed to develop a new HPC in which WSe_2 was coupled to a novel BHJ which employed the *push-pull* copolymer PCDTBT and the fullerene acceptor PC70BM, a TiO_2 ESL and RuO_2 catalyst. This newly designed architecture displayed a remarkable electrochemical stability of more than 14 hours under continuous illumination at 0 V_{RHE}. Furthermore, same photocurrent performances were retained both in acidic and neutral electrolyte (4.5 mA/cm^2 @pH1.25 vs 4.75 mA/cm^2 @pH 6.9). This will yield positive results when integrating this HPC in a tandem system since working in a neutral environment would reduce the overpotentials for the OER to occur.

The relevance of selective contacts engineering on the final device performance has been corroborated from the results obtained on the optimized and newly designed HPCs architectures. To demonstrate how this approach can be beneficial also to fields other than HOPEC-WS, a multimaterial HSL was designed in which water splitting active species were embedded in an organic matrix. The so obtained CuSCN@P3HT composite allowed to impart moisture resistance to a PSC which performances were almost unaffected after 28 days of exposure to high RH environment. This effect has been ascribed to the synergistic effect of the CuSCN species which have been demonstrated to have catalytic activity both toward the HER and OER reaction when compared to the neat P3HT film. In the PSC, a moisture neutralization effect has been obtained at the HSL/Perovskite layer where water molecules coming from the environment are dissociated in harmless by-products thanks to the suitable energetic alignment of the materials employed. Furthermore, a beneficial p-doping effect occurs as the P3HT matrix takes up the generated reactive oxygen species.

Aside from the main experimental outcomes discussed in this thesis, it became evident how a synergist approach is paramount to enable a transition toward a new energetic scenario. The advancements obtained in the field of HOPEC-WS reached a point in which the next step requires to take advantage of the newly developed organic semiconductors which are now leading to a new bloom of the OPV field. Similarly, the world of PSC can benefit of the knowledge of the field of PEC-WS by designing novel approaches to impart moisture resistance to the otherwise water sensitive photoactive layer. To make hydrogen produced from renewables a real deal requires a commitment which spans beyond the field of single technology. This thesis hopes to foster this cross-talk, encouraged from the results shown in these pages.

Appendix

Methods

I Photocathode Fabrication

I.I Substrate Preparation

The substrates of choice for the preparation of the HPC architecture are TCO-coated glass slides. They ensure a high optical transparency and low sheet resistivity, thus efficiently collecting charges to be extracted to the external circuit. The most common examples are indium- or fluorine-doped tin oxide (ITO and FTO respectively). Examples of architectures employing both these materials are present in the text. Yet, in both case the preparation process is the same.

Starting from a commercially available substrate, samples of 15x20 mm^2 each are obtained. A "P" is craved on the glass side by means of a diamond-tip pen to ease the recognition of the conductive surface during the handling of the substrate. A careful cleaning procedure is performed in order to remove any residual contaminants which can be adsorbed onto the surface as a consequence of the fabrication process. To this extent, a series of sonication baths at 40°C are performed in which the employed solvent is sequentially modified. The first step is performed in a water-based solution with an alkaline detergent (distilled water + 2% Hellmanex®). Samples are then removed from the sonication bath and carefully washed with water to remove any residual trace of detergent. A second sonication step is performed in distilled water. Following this, samples are sonicated in acetone and isopropyl alcohol in two subsequent steps to further remove any residual organic contaminant. Finally, samples are dried by means of a N_2 gun and placed in a muffle furnace at 200°C for 2h, allowing a complete evaporation of any residual solvent.

I.II Hole Selective layer – CuI

To obtain HPC which employ this HSL, a solution containing the Copper Iodide precursor is prepared employing acetonitrile as a solvent for its subsequent spin

coating. The right amount of CuI powder (CuI, Sigma Aldrich, electronic grade 99.995% pure) is weighted to obtain a solution with final concentration of 10 mg/mL. The powder is then brought inside a N_2 filled glovebox (H_2O and O_2 < 20 ppm - in the case of films processed in controlled atmosphere) or under a fumehood (for air processed films). In both cases, the correct amount of solvent is then added and the solution is stirred overnight at room temperature to allow a complete dissolution of the powder. Prior spin coating, the cleaned substrates are treated by means of an O_2 plasma asher (15 min, 100 W Power) so that the surface wettability is improved. After this process, the substrates are either brought into the glovebox or under the fumehood and placed on the spincoater. The spin coating process parameters are identical in both cases, so no further distinction is going to be reported. A few drops of solution are placed onto the substrate with a plastic syringe equipped with a PTFE filter (cut-off dimension 450 nm), allowing a complete coverage of the surface. The spin coating process (60s, 4000 rpm, max acceleration) is started as soon as the last drop reaches the surface, allowing a homogeneous evaporation of the solvent. In both cases, samples are then stored in the glovebox until needed.

I.III Hole Selective layer – Pristine WSe_2

When WSe_2 is employed as HSL, the pristine material is obtained via pulsed laser deposition. The process takes in a high-vacuum deposition chamber by means of a high-power laser source which operates in pulsed regime. The schematic of these system is shown in Figure 46. High vacuum regimes are obtained by means of a pumping system which employs a scroll pump and a turbomolecular pump. The first is employed to lower the pressure down to few Pa, while vacuum levels in the order of 10^{-4} Pa are reached once the turbomolecular pump is turned on. A quartz window allows the UV-laser radiation to enter the chamber with negligible attenuation (window transmittance >98%). The laser source is a krypton fluoride excimer laser (Coherent COMPexPro 205 – emitted wavelength 248 nm, pulse duration 15 ns) which output power and pulse frequency can be tuned by means of an electronic control unit. Prior entering the chamber, the laser beam is collimated by means of a plano-convex lens (focal length 50 mm) which can be moved along the optical path by means of a moving stage. This allows to control the size of the focal spot on the targe material, thus tuning the energy density per unit area. Acting on the desired laser power output, frequency and focal positioning of the lens it is possible to adjust the fluence on the target material and adjusted according to the requirements of the deposition process. Additionally, acting on the background gas type and pressure and on relative distance between the substrate and the target it is further possible to control the growth regime of the

deposition and the final morphology of the film. The way in which these parameters participate in determining the final properties of the film is a direct consequence of this peculiar physical vapour deposition technique. Here, the laser pulse is employed to transfer enough energy to the target material for it to be locally vaporized where the laser pulse is focalized. The fraction of material which undergoes this transition is then ejected from the target thanks to the pressure gradient between the target itself and the chamber pressure. This results in a supersonic plasma plume in which the emitted species (from atoms to clusters) travel toward the substrate and perpendicularly to the target. The high energy of the emitted species causes them to bind to the substrate generate the deposit. The amount of energy that the particle have once they reach the substrate ultimately determines the morphology of the film. The larger the distance between the substrate and the target, and the higher the pressure, the more the emitted species may undergo scattering events which will make them lose kinetic energy. The higher their final energy, the more compact will be the resulting film and vice versa. Eventually, a boundary region exists between the two conditions in which the interactions with the gas phase causes them to have a sufficient amount of energy to organize themselves forming nanostructures with preferential direction growth perpendicular to the substrate.

The target film thickness for the WSe_2 HSL is too low to allow this nanostructure to develop. Yet, the aim is to obtain the seed layer of this morphology which is characterized by a columnar structure with preferential orientation perpendicular to the substrate. The target material (WSe_2, Testbourne, 99.95% pure) is placed on a roto-translational target holder which ensure a homogeneous material consumption. To ensure that no oxidation occurs during the deposition, pure argon (Rivoira, 6.0 purity) is employed as a background gas. The process optimization has been performed tuning the deposition pressure in the range between 5 to 30 Pa. Similarly, the laser fluence has been tested from 1.4 J/cm^2 to 2 J/cm^2. Target-to-substrate distance has been fixed at 50 mm. The optimal condition has been identified as 1.4 J/cm^2, 20 Pa background pressure, obtaining a growth rate of approximatively 1.5 nm/s (desired thickness 30 nm).

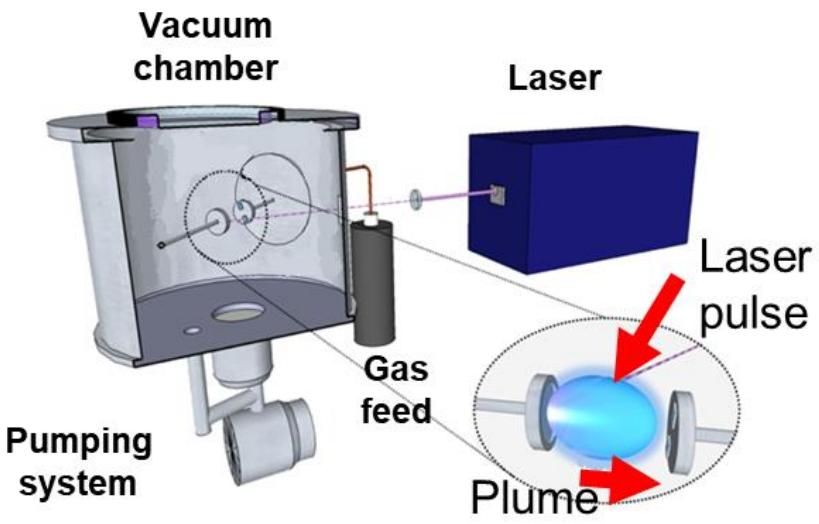

Figure 46: Schematics of the PLD set up.

I.IV Hole Selective layer – Annealed WSe_2

To investigate how the pristine material evolves as a function of temperature, several annealing processes in controlled atmosphere have been performed. Avoiding the presence of oxygen is paramount, as its interaction at high temperature would easily lead to have an oxidized film. To this extent, annealing processes have been performed either in a resistively heated quartz tubular furnace equipped with a vacuum system or in a N_2 filled glovebox. When performed in vacuum, the furnace was evacuated down to 10-3 Pa prior starting the heating program. In both the cases, the annealing temperature has been reached in a controlled way by gradually ramping the temperature both during the heating and cooling steps. For all the conditions, the ramp was set to 4°C/min and the dwelling time to 2h. This ensured that the annealed film did not build up any stress state due to sudden heating/cooling which could have led to cracks formation or film detachment.

I.V Organic Photoactive layer

Two types of bulk heterojunction have been employed in this work, in which two different donor polymers are blended to two different fullerene acceptors.

Donor Polymers:

- poly(3-hexylthiophene-2,5-diyl); P3HT - Sigma Aldrich, regioregular, electronic grade, 99.995% pure, average molecular weight 15000 – 45000 g/mol;
- Poly[N-9'-heptadecanyl-2,7-carbazole-alt-5,5-(4',7'-di-2-thienyl-2',1',3'benzothiadiazole)]; PCDTBT - Ossila;

Fullerene Acceptors:

- [6,6]-phenyl C61 butyric acid methyl ester; PC60BM – Nano-C, 99.9% Pure;
- [6,6]-phenyl C71 butyric acid methyl ester; PC70BM – Ossila;

The details of each formulation, the spin coating recipes and the final thickness are provided in Table 6.

Table 6: Details of the formulation and spin recipe for each BHJ.

Donor	Acceptor	D:A	Final Concentration	Solvent	Spin Speed	Spin Time	Thickness
P3HT	PCBM	1:0.7	51 mg/mL	CB	1600 rpm	1'	160 nm
PCDTBT	PC70BM	1:4	30 mg/mL	o-DCB	1200 rpm	1'	80 nm

The prepare each solution, the same procedure is employed as herein described. The first step is to dissolve amount of donor material in the solvent volume required to obtain the final blend. The solution is heated on a hotplate for one hour without stirring, allowing a complete dissolution of the polymer. In a separate vial, the correct amount of acceptor is weighted. Then, the previously prepared solution with the donor material is transferred into the vial where the acceptor has been weighted. The blend is then stirred at 65°C for at least 3 hours prior spin coating on top of the ITO/HSL.

A sufficient amount of solution is drop-casted on top of each sample (typically 80 µL for this specific sample size). The spin program is started right after having dispensed the solution, according to the details provided in Table 6. According to the type of BHJ, a thermal activation step is necessary in order to promote a correct segregation of the D/A phases. This treatment will be performed upon completion of the device – after having deposited the ESL and catalyst – as it further promotes an efficient interface formation of the whole multi-layered architecture.

I.VI Electron Selective Layer – TiO_2

The nanostructured TiO_2 electron selective layer is deposited on top of the BHJ. The details of the process are independent on the type of D/A materials employed. As for the WSe_2 HSL, this material is deposited via pulsed laser deposition starting from a high purity TiO_2 target (Testbourne, 99.9% pure). The deposition process has been optimized to obtain a film with high surface area, exploiting the positive influence of the nanostructure growth. To enhance the conductivity of the film, a reducing atmosphere has been employed to further enhance the n-type character of the ESL. Thus, the background gas selected is a mixture of argon-hydrogen (Rivoira, 6.0 purity, 5% hydrogen in volume) with a final pressure of 45 Pa and a laser fluency of 2 J/cm^2. The deposition time has been calibrated to obtain a 100 nm thick film. Do avoid the formation of short-circuit paths between the ESL and the TCO, the sample has been masked to expose an active area o 10x10 mm^2. Same deposition mask will be employed to deposit the platinum catalytic layer.

I.VII Catalyst – Platinum

To deposit the platinum catalyst layer, pulsed-direct current magnetron sputtering has been employed. As for the pulsed laser deposition, this physical vapour deposition is performed in the high-vacuum chamber. This technique exploits the erosive action of ionized gas particles to eject clusters of atoms from the surface of the target material. To sustain the ionization of the gas particles, a high voltage is applied between the cathode (the target material) and the magnetron head which serves as an anode. This potential field forces the free electrons present in the chamber toward the anode following the lines of the magnetic field generated by the permanent magnet inside the sputtering head. Along this path, the gas atoms are positively ionizing by interacting with the highly energetic electrons. These positively charged species are then drawn toward the negatively biased target material with high kinetic energy. This energy is transferred to the atoms of the material on the target, providing them with enough force to be ejected from the surface. Since this technique operates in pulsed regime, it allows to switch with high frequency the polarity of the components, avoiding the accumulation of charged species on the surface which would reduce the sputtering yield. This is also highly affected by the applied potential, which is controlled by the external power source. Indeed, the source is controlled in power, so it adjusts the current-voltage working point in order to match the requested output. The working point is highly dependent on the type of material which is being sputtered and the gas

type/pressure. The nature of the gas also affects the nature of the process. If the process gas is inert (like argon) the sputtered material does not undergo any chemical modification during the process. On the other hand, if a reactive specie is present (like oxygen), it is possible to induce an oxidation of the emitted species that can be converted for example from metal (at the target) to oxides (at the substrate). Usually, a mixture of gases is employed in reactive processes as the sputtering power ox reactive oxygen species is poor and its main action would be to induce a surface oxidation of the target material. The addition of an inert gas provides to have a substantial sputtering efficiency, while the oxidant fraction reacts while the species travel toward the substrate.

In this specific case, the deposition chamber has been equipped so that the catalyst can be deposited as soon as the ESL deposition is concluded, without exposing the samples to atmosphere and preserving a neat surface. Thus, once the PLD step is concluded, the chamber is evacuated from the process gas and brought down to its base vacuum value. Then the new process gas for the Pt sputtering process is fluxed into the chamber. In this case, the gas of choice is pure argon (Rivoira, 6.0 purity) with a total pressure of 15 Pa. The p-DC MS deposition has been performed at a fixed power of 22 W (working point 62 mA 348 V) on a pure Pt target (Kurt J. Lesker, 99.9% pure). The pressure and working power have been selected so that the emitted species have a low energy once they reach the substrate, avoiding damaging of the TiO2 layer and deep implantation. The deposition rate is 0,05 nm/s, and the deposition time has been adjusted to obtain films of 4, 10 and 16 nm.

I.VIII Catalyst – RuO_2

After the optimization, HPC architectures have been realized replacing Pt with RuO_2. To ensure a better adhesion on the catalyst layer, p-DC MS has been replaced with photoassisted electrodeposition. This technique allows to obtain a homogeneous coverage of solid species on a conductive electrode. The electrode which has to be coated must be immersed in an electrochemical solution in which a precursor of the material to be deposited has been dissolved. The precursor, once dissolved release the final material in its ionic form. When enough potential is applied to the working electrode, the ions exchange charge with the electrode and gets deposited in solid form on the surface. Here, the process is aided by shining light on the HPC in order to increase the conductivity of the BHJ and allow to work at very low applied potentials.

In this specific case, the electrodeposition bath consisted of a 1.3 mM solution of $KRuO_4$, as described in the work of Tilley et al. [140]. The process has been performed

in a 2-electrode configuration in galvanostatic mode (fixed current density of -28,3 $\mu A/cm^2$) in which the HPC was the working electrode and a Pt wire was placed as counter/reference electrode. The very low required current density allowed to operate at very low applied potential and in a slow growth regime. This ensured that the HPC did not undergo any degradation. The deposition time has been set to 450 s, obtaining a 4 nm thick RuO_2 layer on an area of 0.2 cm^2 as defined by the vinyl tape mask.

I.IX Thermal Activation

To finalize the HPCs, a mild thermal treatment is performed in order to favour the reorganization of the BHJ and favour interface formation. This step is performed in a N_2 filled glovebox and at relatively low temperatures not to induce degradations on the organic materials due to the interaction with thermally activated oxygen radicals which can break open the polymer chains, reducing its charge transport properties. For HPC employing P3HT:PCBM, the temperature was set to 130°C and kept constant for 10 minutes. When PCDTBT:PC70BM was used as BHJ, lower temperatures were selected (80°C) for the same amount of time. Once the annealing is concluded, the samples are allowed enough time to cool down prior being removed from the glovebox for the characterization.

II Ru-catalyst for OER in HPC-PSC Tandem

The realization of the OER catalyst employed in the HPC-PSC tandem has been done following the guidelines of Oppedisano et al. [83]. In their work they realized a high performing Ru catalyst via electrodeposition starting from a 0.25 M $HClO_4$ solution with 15mM $RuCl_3 \cdot xH_2O$ precursor. Here their recipe has been replicated to obtain a high performing OER catalyst on par of the state of the art electrocatalyst. The electrodeposition is performed on a titanium foil, to which a potential of -5 VRHE is applied for 300 s. Before the electrodeposition, a galvanostatic pulse sequence is applied to promote a homogeneous nucleation of clusters on the surface. The film has been deposited on an active area of 0.066 cm^2, defined using a vinyl tape mask.

III Perovskite solar cells

The synthesis and fabrication of the materials and devices connected to the realization of the perovskite solar cells presented in this work has been carried out from our collaborators. Thus, a detailed description can be found in the published papers[68,74].

IV Electrochemical Set Up

The electrochemical characterization of the HPCs and catalysts are performed in an electrochemical cell in which the water splitting reaction occurs. According to the type of measurement, both 3-electrode or 2-electrode configuration are adopted. In a 3-electrode configuration, the element which is under investigation is placed as working electrode. A catalytic counter electrode is employed so that the other half reaction can occur without limiting the process taking place on the working electrode. The third element is a reference electrode against which the potential of the working electrode can be measured and referred to a known scale. In a 2-electrode configuration, the reference electrode is removed and the potential can only be expressed as ΔV between the working and counter electrode.

In both cases, the electrodes are immersed in the electrolyte which is contained in a glass cell with two quartz sides and airtight openings through which the electrodes or additional components can be inserted. The quartz sides allow, in the case of measurements performed under illumination, to avoid undesired absorption of the UV-part of the spectrum from the glass. Careful cleaning by means of milli-Q water is performed on each element before assembly of the full electrochemical system. When measurements required the absence of oxygen, a vigorous N_2 flow is fluxed in the cell by means of a porous septum immersed in the solution. This allows to strip molecular oxygen dissolved in the electrolyte and in the internal environment of the cell. The outlet flux is allowed to pass in a water bath which prevents back-diffusion of oxygen from the external environment.

IV.I Illumination System

To assess the photoactivity of the elements, their response to simulated sunlight is acquired by means of a solar simulator (Lot Oriel, model LS0306). The system is equipped with a 300 W xenon arc lamp and a set of filters which precisely allow to modulate the output according to the AM 1.5 G spectrum. This standard defines

the solar radiation incident on the earth with a 48.2° zenith angle, correspondent to 1.5 atmospheric thicknesses, resulting in an incident power density of 100 mW/cm^2. The output is calibrated by means of a photodiode which allowed to identify the focal region where the intensity was equal to 1 Sun.

IV.II Counter and Reference Electrodes

The reference electrode employed in 3-electrode measurements is a Ag/AgCl saturated in KCl. This electrode redox couple has a known potential of + 0.1976 V_{SHE}. It is a widely employed and robust reference electrode and, taking into account its offset value and the influence of the solution pH it is possible to express the potential of a given electrochemical measure with respect to the Reversible Hydrogen Electrode (RHE) potential through the Nernst Equation:

$$E_{RHE} = E_{REF} + E^0_{REF} + 0.0591 \times pH$$

Here E_{RHE} is the potential with respect to the RHE scale, E_{REF} is the potential measured with respect to the reference electrode (+0.1976 V for Ag/AgCl) and pH indicates the measured pH value.

The counter electrode is a coiled platinum wire, which is known to be an excellent catalyst also for water oxidation. This configuration ensures that the high surface area is such not to limit the reaction kinetic and avoid gas bubbles to stick on the surface.

IV.III Electrolytic solution

In this work, two main electrolytes have been employed. One has been used for the characterization of HPC/characterization of the tandem in acid pH and the second for the assessment of the performance retention of the WSe_2-based HPC in neutral pH.

The acid electrolyte is a H_2SO_4 based solution in which sulphuric acid (Sigma Aldrich, 95-98% concentrated) is dissolved in milli-Q water to reach a pH of 1.25. The so prepared solution is stirred overnight and the pH valued is checked by means of a pH meter prior having it used for the electrochemical characterization, eventually adjusting is value by adding water or H_2SO_4.

The neutral electrolyte is a 0.1 M Sodium Phosphate buffer solution with pH= 6.9. The solution is prepared by mixing Sodium phosphate dibasic heptahydrate ($Na_2HPO_4 \cdot 7H_2O$, Sigma Aldrich, ACS reagent, ≥98% Pure) and Sodium phosphate

monobasic monohydrate ($NaH_2PO_4 \cdot H_2O$, Sigma Aldrich ACS reagent, ≥98% Pure) in milli-Q water. The solution is stirred overnight and the pH is checked by means of a pH-meter before the electrochemical measurements. Eventually, the addition of $Na_2HPO_4 \cdot 7H_2O$ or $NaH_2PO_4 \cdot H_2O$ is performed to adjust the pH to the desired value.

As previously described, both the electrolytes are purged with N_2 to avoid dissolved oxygen to react with the photocathode during the measurements.

IV.IV Three- electrode Configuration

Electrochemical reactions are the result of an anodic and a cathodic component. To address them separately, the electrochemical characterization is performed in a three-electrode system. This ensures that the recorded current/potential is related to the reactions occurring ad the electrode/electrolyte interface of the working element only. When two-electrode configurations are employed, the counter electrode needs to balance the reaction occurring at the working electrode and potential recorded is thus connected to the whole process taking please in the electrochemical cell, thus not allowing to disentangle the reactions occurring at the two electrodes. Therefore, three-electrode measurements are preferred as it allows to retrieve meaningful information on the working electrode as the half-cell dynamics are the ones being recorded. Here, the potential is read as a difference between the working electrode and the reference, where the latter does not participate to the reaction but serves solely to provide a, indeed, a reference value. The reaction occurring at the counter electrode is not influencing the measurement at the working electrode, as its potential/current are controlled by the external system in order to balance the reaction.

V Tandem HPC-PSC-OER

The electrochemical characterization of the three-element tandem system required to adapt the measurement set-up accordingly. Here, the system employs two electrochemically active components: the photocathode and the anodic electrocatalyst. Thus, these two elements when part of the tandem will behave as in a two-electrode configuration in which the value of potential will correspond to the value applied from the potentiostat across them. Additionally, the PSC must be included in the system so that its photovoltage can contribute to the overall system potential balance. Thus, the back contact of the HPC will be connected to

one of the end contacts of the PSC, while the other one will be connected to the potentiostat. Ultimately, this will lead to "two" components: the HPC-PSC and the OER catalyst. The recorded potential in the full assembly will not be converted to the RHE scale, as its value is just an indication of the overall potential drop across the system.

In this configuration, the operating current density recorded will be proportional to the solar to hydrogen efficiency of the system through the equation:

$$\eta_{STH} = \frac{J_{op}\, E_{WS}\ FE}{P_{in}}$$

In which J_{op} is the operating current density [A/cm^2], E_{WS} is the water splitting potential [1.23 V_{RHE}], FE is the faradaic efficiency and P_{in} is the incident solar power [W/cm^2].

This formula can be also rewritten as:

$$\eta_{STH} = \frac{r_{H2}\ \Delta G^0}{P_{sun}\, A}$$

Where rH_2 is the molar rate of hydrogen production [mol/s] times the molar change in Gibbs free energy for the reaction ΔG^0 [J/mol], P_{sun} is the illumination power density [mW/cm^2] and A the electrochemical active area [cm^2]. The Faradaic efficiency is what links J_{op} to rH_2.

VI Electrochemical Measurements

All the measurements have been performed by connecting the electrochemical cell to a potentiostat (Autolab PGSTAT 30), which was controlled via a dedicated proprietary software (Nova 2.0). The same software also allowed to perform data analysis on the spectroscopic procedures.

VI.I Linear Sweep Voltammetry (LSV)

Linear sweep voltammetry is a widely employed electrochemical characterization technique in which the current flowing through the working electrode is recorded as a function of the applied potential. The potential is swept linearly across a range of value which is defined according to the type of electrode which is being characterized. The scan rate [mV/s] is selected at the beginning of the

measurement and is constant for each scan. This latter parameter has to be chosen taking into account that it can influence the magnitude of the measured current. Indeed, as the potential is scanned, is leads to a polarization of the electrode surface which in turns causes ions to move toward it. This leads to the formation of a diffusion layer in which the ions concentration is lower than in the bulk of the electrolyte, which then lowers the measured current. A suitable measurement condition has been selected to be 10 mV/s. This ensures that the measured current is not limited by the kinetics of the reaction and still falls in a reversible reaction regime.

When it comes to characterizing photoactive components, LSVs can be performed alternating light and dark regime. This allows to simultaneously access the photoactive behaviour of the device and its pure electrochemical one. While the current recorded under illumination is proportional to the hydrogen evolution reaction, the component in dark conditions allows to access information on eventual reactions occurring. Ideally, the value of the dark current should be orders of magnitude lower than the photocurrent. This is common component and is ascribed as leakage current in an ideal photodiode. If higher values are recorded, this could allow to identify reactions, even irreversible ones, which could be occurring in the multi-layered architecture. This could be the case, for example, if some chemical degradation is occurring.

Characteristic values can be retrieved from a linear sweep voltammetry, which complement the description of the investigated device. The open circuit potential (V_{OC}) can be measured when no potential is applied to the working electrode. Usually, this potential is set as the initial value for the LSV scan. As soon as the potential scan begins, the (photo)current starts to rise. Once it exceeds the threshold value of 10 μA/cm^2, the corresponding potential identifies the onset potential (V_{OP}). This quantity is commonly accepted to represent a valuable indication of the photocurrent connected to the HER, as it should be one o.o.m higher than the dark current. Further analysis of the LSV allows to obtain a descriptive parameter to compare the performances of different photocathodes. This value is the ratiometric power-saved (φ_{Saved}) and gives an indication of the amount of power that the photoelectrode is providing to bias the HER which would otherwise be provided by an external system.

This can be obtained from the following equation:

$$\varphi_{Saved} = \frac{f_{FE} J_{MPP} V_{MPP}}{P_{in}}$$

This is identified by multiplying the whole range of current-voltage data acquired from the LSV and corresponds to the maximum value of the plot. At that point,

the corresponding potential identified the maximum power point (V_{MPP}) which corresponds to a given current density value from the LSV (J_{MPP}).

VI.II Cyclic voltammetry (CV)

Similarly to LSV, cyclic voltammetry records the working electrode current as a function of the applied potential. Here, instead of a single sweep, the potential is cyclically scanned between an upper and lower limit for a given amount of times/cycles. The range is selected according to the electrode under investigation. This measure allows to identify redox reactions occurring between the electrode and the electrolyte which can be identified as peaks in the current profile during the backward/forward scan. If the current profile is overlapped upon successive cycles, the peaks which are recorded can be ascribed to reversible redox reactions. The opposite holds true if the peaks height/positions change over time, as they can be related to irreversible/time dependent processes. This allows to gain insights on the electrochemical stability of the material/device under investigation in that specific potential range and electrolytic solution. Also in this case, the scan rate has the same influence as for LSVs and has been set to 10 mV/s.

VI.III Chronoamperometry (CA)

This electrochemical measurement allows to record the time dependent behaviour of the (photo)current of the working electrode at a fixed applied potential. According to the type of electrode, the potential can be chosen in relation to the desired information which are aimed to be obtained. As an example, it can be the hydrogen evolution potential (0 V_{RHE}), the oxygen evolution potential (1.23 V_{RHE}) or the maximum power point of the device (V_{MPP}). Similarly, the duration of the measure and the time sampling frequency can be chosen arbitrarily. The change in photocurrent density gives indication on the stability of the device under the specific testing conditions. A decaying current profile may suggest that a degradation is occurring at the working electrode. In the case of photoelectrodes, CA can be performed under continuous illumination or also in chopped regime. This allows to evaluate how the dark current (which can be connected to irreversible degradation processes occurring within the architecture) evolves over time.

VI.IV Electrochemical Impedance Spectroscopy (EIS)

By means of Electrochemical Impedance Spectroscopy (EIS) it is possible to obtain a frequency dependent characterization of the behaviour of an electrode. It works by applying a frequency modulation to an input signal (current/voltage) and record the response of the system. The sinusoidal variation of the input leads the output to be modulated as well. A given value of input signal is chosen, the system then applies a small amplitude variation which falls within the boundaries of the perturbation theory. By taking the ratio between input and output signal, the complex impedance data are obtained. The representation of the real and imaginary component of the impedance are visually represented by the Nyquist plot. On the other hand, the frequency dependent behaviour of the phase or the modulus of the impedance can be represented by means of the Bode plot.

The complex set of data can be employed to get insights on the frequency dependent behaviour or the electrochemical process occurring on a given system. This can be done by fitting the experimental data with an equivalent circuit with a proper combination of resistances, capacitances or constant phase elements. Each element provides a description of a given charge-related process occurring at the electrode. While the interpretation of the data is far from being trivial, it offers some intriguing perspectives on the behaviour of the system. In this work, the frequency range employed was 0.5 Hz to 10 5 Hz and the modulation amplitude 10 mV.

Fitting of the data has been done with the proprietary software Nova 2.0 which includes an efficient tool to perform this analysis.

VI.V Intensity Modulated Photocurrent/Photovoltage Spectroscopy (IMPS/IMVS)

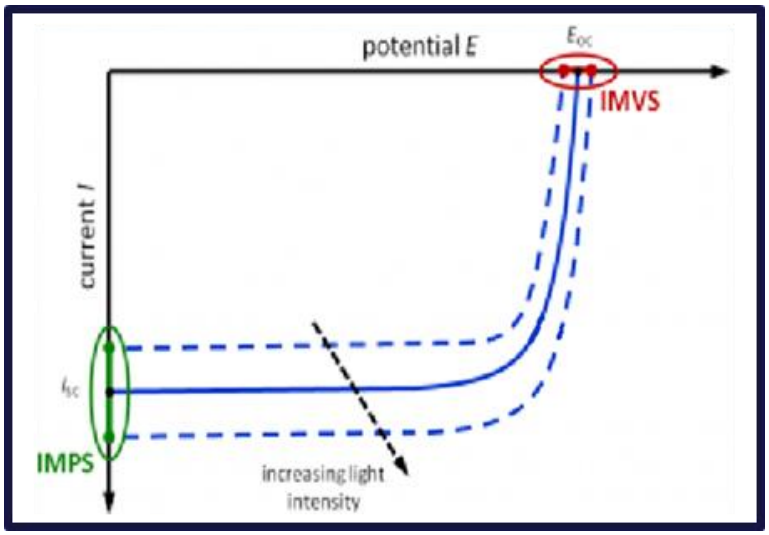

Figure 47: Schematics of the IMPS and IMVS procedure with respect to a typical J-V characteristic.

These spectroscopic techniques are similar to the previously discussed EIS. The main difference is that here the sinusoidal modulation is applied to the light source rather than to the applied current/voltage. To perform these measurements, the illumination source is a monochromatic LED in place of the solar simulator. This allows to select a proper wavelength so that the photogenerated charges arise from a selective excitation of the photoactive layer only. In this way is possible to rule out additional contributions of photogenerated charges coming from other layers which may have different characteristic times. A schematic of these measurements can be seen in Figure 47. From Intensity Modulated Photocurrent Spectroscopy (IMPS), it is possible to retrieve useful information on the characteristic diffusion time of photogenerated charges across a photoelectrode. This is achieved by applying a fixed potential (e.g. 0 V_{RHE}) and measure the photocurrent output. This output will be modulated according to the frequency dependent amplitude variation of the light source. Similarly to EIS, these complex data can be represented through Nyquist or Bode plots. The most interesting parameter which can be extracted from this analysis is the characteristic frequency of the maximum of the Nyquist plot (f_{IMPS}). The diffusion time τ_d can be obtained from the formula:

$$\tau_d = \frac{1}{(2 * \pi * f_{IMPS})}$$

Intensity Modulated Photovoltage Spectroscopy (IMVS) is a close relative of IMPS, the main difference is that it is performed by imposing the circulating current to

be equal to 0 and measuring the voltage output. This condition corresponds to the V_{OC} of the device. Here, information on the characteristic recombination time of the photogenerated charges (τ_{rec}) can be obtained from the frequency maximum of the Nyquist plot (f_{IMVS}). Like for IMPS, the formula is:

$$\tau_{rec} = \frac{1}{(2 * \pi * f_{IMVS})}$$

By combining this information, it is possible to obtain the charge collection efficiency of the device (η_{CC}) as:

$$\eta_{CC} = 1 - \frac{\tau_d}{\tau_{rec}}$$

This parameter offers a good indication of the fraction of photogenerated charges which can be extracted from the photoelectrode and the extent of those lost to recombination.

VII Morphological and Structural Characterization

VII.I Atomic Force Microscopy

The surface topography of the materials has been probed by means of atomic force microscopy (AFM). The system (Agilent 5500) allowed resolve features with a vertical resolution of fractions of nanometers and 10-15 nm in of lateral resolution. Operating in tapping-mode, the cantilever tip oscillates close to its resonance frequency in close proximity of the surface. The tip, which has a small radius of curvature, is highly sensitive to interactions with the material. Here, electrostatic and Van Der Waals forces causes the cantilever to modify its oscillation period. This variation is resolved from a detector which reads the position of the reflection of a laser that is focalized on the cantilever tip. The detector then converts this spatial displacement in a height variation induced by the material surface. As the tip is scanned line-by-line on the sample, it is then possible to reconstruct a topography map of the scanned area. Furthermore, the phase variation of the tip oscillation can also be recorded to obtain a phase contrast map. This allows to deduce variations of the material composition, as the phase is highly sensitive to material-specific surface properties. To avoid damaging of the tip, an electronic feedback controls the deflection of the cantilever preventing it to stick to the surface due to the strong interaction.

Analysis of the AFM data has been performed with Gwyddion, a dedicated software that allows to obtain a broad range of parameters from the height maps.

VII.II Scanning Electron Microscopy (SEM)

Scanning electron microscopy is a powerful tool that allows to probe the morphology of a surface with accuracy down to few tens of nanometres. Aside from instrument-specific variations, several specific components are always necessary. A vacuum system is required in order to operate the instrument. It ensures that the emitted electron beam is not attenuated upon interaction with gas molecules and that the electron source does not get corrupted at high temperature due to the presence of oxygen. The source is typically a tungsten filament which, upon heating, emits electron via thermionic emission with energy ranging from 0.2 to 40 keV. The emitted beam is focussed by means of condenser lenses and scanned on the surface through deflector plates. Once the electron beam impinges on the surface, it can lead to several types of interactions which offer complementary information. Secondary electrons can be emitted from the surface as a consequence of the interaction. Since surface features have different emission yield, once detected, they provide a morphology image in which the contrast arises from these discontinuities. A different analysis can be done on the basis of backscattered electrons. These species are electrons from the source beam which are reflected upon interaction with different specimens present in the interaction volume. As different materials have different density, a phase contrast can be obtained highlighting different composition on the specimen under investigation. By tuning parameters such as beam energy, focal point, magnification and stigma it is possible to adjust the quality of the image which ultimately is highly dependent on the material itself. In this work two types of instruments have been employed, a Zeiss SUPRA40 and a JEOL InTouchScope™. The first has been employed to acquire high resolution images, while the latter allowed a faster but less accurate imaging.

VII.III X-Ray Diffraction Spectroscopy (XRD)

X-Ray Diffraction Spectroscopy allows to investigate the crystalline structure of the material. This technique relies on the interaction of X-ray radiation which has a characteristic wavelength comparable to interatomic distance across crystalline planes in a material. Upon interactions with the lattice, the radiation is reflected outside the sample at a characteristic angle. A moving detector collects the outgoing signal over a predefined range of angles. The complete diffractogram can then be compared with the ones available in the instrument proprietary database allowing to identify the crystalline phases present in the sample. Diffraction peaks

arise only when a constructive interference condition is satisfied. This is expressed through the Bragg's law:

$$n\lambda = 2d \sin\theta$$

Where $n\lambda$ express a multiple of the exciting wavelength, d is the spacing between lattice planes and θ is the incident angle. Each peak can further be analysed through Scherrer's equation, obtaining the average size of the crystalline domains.

The instrument employed is a Bruker D8 Advance. It employs a copper target which generates X-ray radiation in a cathode ray tube. The copper Kα radiation (1.54 Å) is then selected by means of a monochromator and collimated toward the sample.

VIII Optical and Electronical Measurements

VIII.I Kelvin Probe Force Microscopy

A Kelvin probe force microscope (KP Technology, KPSP020) is employed to measure the work function of the materials and substrates tested in this work. AFM can be employed to perform this type of measure provided that suitable tip and configuration are employed. In the current case, the instrument is composed of a non-scanning tip which locally evaluates the work function of the material. It is an indirect measure, as the work function has to be calibrated with respect to a known reference. The setup is composed of a software controlled digital control unit to which an oscilloscope is connected. The oscilloscope generates an output oscillating signal which is fed to the probe sensor and tip. The tip is brought close to the surface of the sample until the intensity of the signal reaches a sufficient value. As the tip oscillates, the capacitance between the tip and the surface changes and charges are moved in the electrical circuit of the instrument. The potential read by the instrument is converted in terms of contact potential difference (CPD), that is the potential required to align the vacuum levels of the tip and the samples. This potential is equal to the one which has to be applied to the material in order to remove the outmost electron on its surface. Once calibrated against a reference sample (Gold, WF= 4.8 eV), this value returns the actual work function of the sample.

VIII.II Raman Spectroscopy

Raman spectra were acquired with a Renishaw InVia Raman Microscope, using a 532 nm excitation laser line. Static or extended acquisitions have been performed to maximize the quality of the signal. The focusing lens and the incident power

was adjusted for each material to avoid material modification due to interaction with the laser beam. Through Raman Spectroscopy it is possible to gather detailed

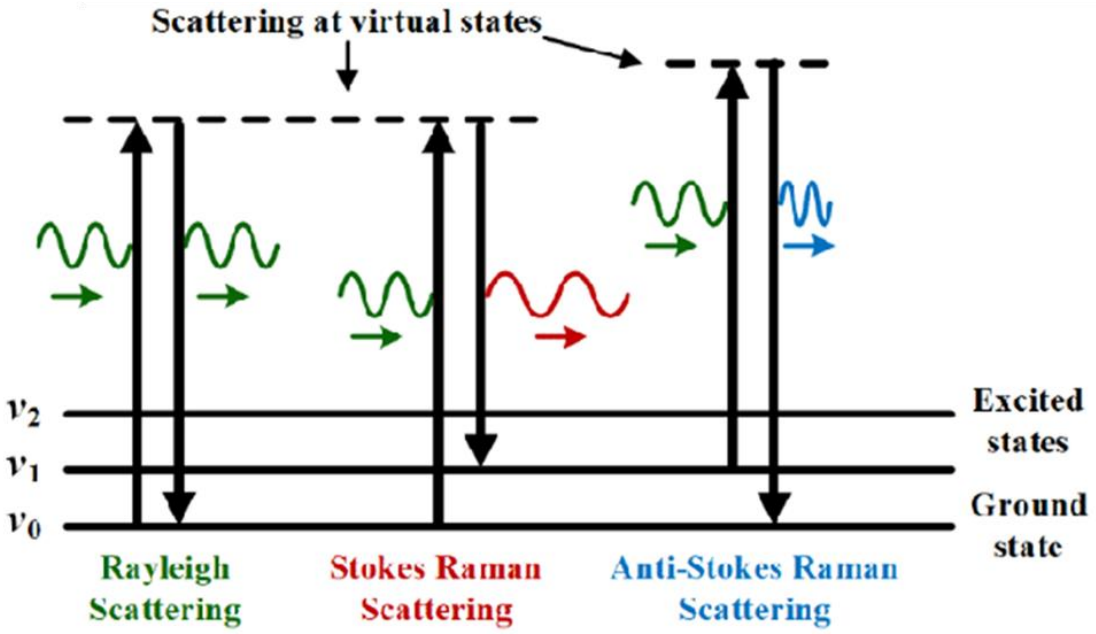

Figure 48 : Schematics of the scattering events which take place upon interaction of a monochromatic light source with a material and the relative outgoing signal. Ref: 10.1049/hve.2019.0157

information such as the chemical structure of a material and its crystalline phase. The process relies on the interaction of a material with a monochromatic light source. The scattering events which occur after this interaction can be of different kinds and are briefly shown in Figure 48. The vast majority of the radiation is reflected back with the same wavelength that it had before hitting the material (Rayleigh Scatter), thus it does not carry any information on the material. A small fraction of the incoming radiation is, however, emitted at a different wavelength (Raman Scattering). The difference is quantified in Raman Shift (cm^{-1}), and it is a unique signature of the interaction of light with the chemical structure of the sample under investigation. The count of Raman Scattered photons over a range of Raman Shift allow to reconstruct the Raman Signature of a substance. The peaks can then be analysed to understand the structure of the material.

VIII.III UV-Vis Spectrophotometry

In most of the cases discussed in this work it has been necessary to assess the optical absorption properties of the materials and devices being tested. This has been done by means of a Perkin Elmer – Lambda 1050 spectrophotometer. The instrument is equipped with multiple light sources and detectors which allow to cover a range of wavelength between 250 – 2000 nm. Before reaching the sample,

a monochromator selects each wavelength individually and scans the selected range with a selected interval. The measurements were performed equipping the integrating sphere module. This allowed to collect the Total Transmittance (T) and Total Reflectance (R) data. The two components can be then used to obtain the absorptance of the material with the relationship:

$$A[\%] = 100 - T[\%] - R[\%]$$

IX Tandem Modelling

Modelling of the theoretical STH efficiency of tandem systems is an interesting topic which has been previously investigated from several groups[90–93] allowing to picture the efficiency of these systems under various assumptions. Yet, a dedicated model which accurately describes the efficiency of PEC-PV systems based on organic materials is still missing. This section will provide a step-by-step description of the process which led to the performance validation of this specific system and the sensitivity analysis to reach 20% STH.

Each photoactive material can, upon photon absorption, produce a theoretical value of photocurrent as described by the Shockley-Queisser analysis:

$$J_L = q \int_{E_g}^{\infty} IPCE\, n_{ph}(E) dE$$

Being J_L the theoretical (maximum) value of photocurrent, q the elementary charge, IPCE the incident photon to current efficiency, n_{ph} the number of incident photons (for this application, related to the AM 1.5G solar irradiance spectrum. These values are integrated over all the photons which energy is higher than the material bandgap (E_g).

Since the ultimate requirement which has to be met for this system to perform water splitting the overall voltage of the stack, it is convenient to express the current-voltage characteristic of each element by means of a current-dependent photovoltage – an inverse formulation of the diode equation. Following the work of Fountaine et al. [90]:

$$V_{PV}(j) = \frac{n_d k_B T}{q} ln \left[\frac{f_{abs} J_L - j - \frac{(V_{PV} + jR_S)}{R_{Sh}}}{J_0/_{ERE}} + 1 \right] - jR_S$$

where n_d is the diode ideality factor, k_B is the Boltzmann constant, T the device temperature, f_{abs} is the semiconductor absorption fraction, ERE is the external radiative efficiency, J_0 is the dark current, R_s and R_{sh} are the series and shunt resistance respectively. This expression describes accurately the photovoltage characteristic of a generic solar cell. While it is sufficient to describe the PSCs behaviour, it needs an additional contribution in order to model the behaviour of a HPC. This contribution is the overpotential connected to the catalytic reaction occurring at the HPC/electrolyte interface. Generally speaking, the overpotential of a given catalytic reaction ($V_{cat}(j)$) can be described through an inverse formulation of the Butler-Volmer equation:

$$V_{cat}(j) = \frac{RT}{\alpha n_e F} sinh^{-1}\left(\frac{j}{2\,J_{0,cat}}\right)$$

Where α is the charge transfer coefficient, ne is the number of electrons taking part in the reaction, F is the Faraday constant and $J_{0,cat}$ is the catalytic exchange current density. The anodic and cathodic overpotential are denoted as $V_{cat,a\,(j)}$ and $V_{cat,c\,(j)}$ respectively.

The photovoltage of the HPC is thus a superimposition of the diode equation and the Butler-Volmer equation for the cathodic half reaction. Thus, the corresponding current voltage characteristic for the photocathode will be:

$$V_{HPC}(j) = V_{PV}(\mathrm{j}) - V_{cat,c}(j)$$

In order to take into account the peculiar characteristic of organic semiconductors, an additional term will be included which describes the intrinsic losses which limit the maximum photovoltage achievable with this type of material. From a given BHJ, this value is strictly correlated to the energy difference between the highest occupied molecular orbital (HOMO) of the donor and the lowest unoccupied molecular orbital (LUMO) of the acceptor, minus the voltage loss (V_{LOSS}) arising from to the non-ideality of the system.

$$V_{OC} = \frac{1}{e}\left(E_{A,LUMO} - E_{D,HOMO}\right) - V_{LOSS}$$

The voltage loss is an empirical way to take into account energy lost both during charge generation and charge recombination. Understating the insurgence of these phenomena is one of the hot topics in the field of OPV, as it represents a significant barrier towards the implementation of high-PCE moduli. Including this parameter

in the model is therefore essential to effectively describe the maximum photovoltage values that can be achieved by the system.

In order to identify suitable combinations of materials and devices which supply enough potential for the water splitting reaction to occur, the lower limit must be identify the condition above which a current shall circulate into the system. This is indeed the electrochemical potential for water splitting (E_{WS} = 1.23 V_{RHE}). Thus, the overall balance of the system shall satisfy the following relation:

$$V_{HPC-PSC}(j) = V_{PV}(j) + V_{HPC}(j) - V_{cat,a}(j) \geq E_{WS}$$

At the maximum efficiency point of the system (i.e. when the output voltage is equal to the water splitting potential) the operating current of the system can be identified, which can be converted into the system STH through the formula:

$$\eta_{STH} = \frac{J_{op} E_{WS}\, FE}{P_{in}}$$

Where J_{op} is the operating current density, E_{WS} is the water splitting potential of 1.23 V_{RHE}, FE is the Faradaic Efficiency and P_{in} is the incident solar power.

Bibliography

1. Commission, E. European Green Deal. Available at: https://ec.europa.eu/info/strategy/priorities-2019-2024/european-green-deal_en. (Accessed: 20th March 2021)
2. Mackay, J. R. & Fyles, J. G. A Hydrogen Economy. *Science (80-.).* 1323 (1972).
3. Cihlar, J. *et al. Hydrogen generation in Europe: Overview of costs and key benefits*. (2020).
4. IRENA. *Hydrogen From Renewable Power*. *International Renewable Energy Agency* (2018).
5. Commission, E. *COMMUNICATION FROM THE COMMISSION TO THE EUROPEAN PARLIAMENT, THE COUNCIL, THE EUROPEAN ECONOMIC AND SOCIAL COMMITTEE AND THE COMMITTEE OF THE REGIONS*. (2020).
6. Nakamura, A. *et al.* A 24.4% solar to hydrogen energy conversion efficiency by combining concentrator photovoltaic modules and electrochemical cells. *Appl. Phys. Express* **8**, (2015).
7. NREL. Best Research Cell Efficiency Chart. (2021). Available at: https://www.nrel.gov/pv/assets/pdfs/best-research-cell-efficiencies.20200104.pdf. (Accessed: 20th March 2021)
8. Li, J. & Wu, N. Semiconductor-based photocatalysts and photoelectrochemical cells for solar fuel generation: a review. *Catal. Sci. Technol.* **5**, 1360–1384 (2015).
9. Bak, T., Nowotny, J., Rekas, M. & Sorrell, C. . Photo-electrochemical hydrogen generation from water using solar energy. Materials-related aspects. *Int. J. Hydrogen Energy* **27**, 991–1022 (2002).
10. Jia, J. *et al.* Solar water splitting by photovoltaic-electrolysis with a solar-to-hydrogen efficiency over 30%. *Nat. Commun.* **7**, 1–6 (2016).
11. European Commission. A Hydrogen Strategy for a climate neutral Europe The path towards a European hydrogen eco-system step by step : (2020).
12. Emanuele Taibi and Raul Miranda (IRENA), Wouter Vanhoudt, Thomas Winkel, J.-C. L. and F. B. (Hinicio). *Hydrogen From Renewable Power*. (2018).
13. Fujishima, A. Eletrochemical Photolysis of Water at a Semiconductor Electrode. *Nat. Mater.* **238**, 37–32 (1972).
14. Pan, L. *et al.* Boosting the performance of Cu2O photocathodes for unassisted solar water splitting devices. *Nat. Catal.* **1**, 412–420 (2018).
15. Jiang, C., Moniz, S. J. A., Wang, A., Zhang, T. & Tang, J. Photoelectrochemical devices for solar water splitting – materials and challenges. *Chem. Soc. Rev.* **46**, 4645–4660 (2017).
16. Tachibana, Y., Vayssieres, L. & Durrant, J. R. Artificial photosynthesis for solar water-splitting. *Nat. Photonics* **6**, 511–518 (2012).
17. Chen, Y. *et al.* Metal Oxide-Based Tandem Cells for Self- Biased Photoelectrochemical Water Splitting. *ACS Energy Lett.* **5**, 844–866 (2020).
18. Ahmed, M. & Dincer, I. A review on photoelectrochemical hydrogen production systems: Challenges and future directions. *Int. J. Hydrogen Energy* **44**, 2474–2507 (2019).
19. Cheng, W. H. *et al.* Monolithic Photoelectrochemical Device for Direct Water Splitting with 19% Efficiency. *ACS Energy Lett.* **3**, 1795–1800 (2018).
20. Tembhurne, S., Nandjou, F. & Haussener, S. A thermally synergistic photo-electrochemical hydrogen generator operating under concentrated solar irradiation. *Nat. Energy* **4**, 399–407 (2019).
21. Kim, J. H., Han, S., Jo, Y. H., Bak, Y. & Lee, J. S. A precious metal-free solar water splitting cell with a bifunctional cobalt phosphide electrocatalyst and doubly promoted bismuth vanadate photoanode. *J. Mater. Chem. A* **6**, 1266–1274 (2018).
22. Kim, J. H. *et al.* Hetero-type dual photoanodes for unbiased solar water splitting with extended light

harvesting. *Nat. Commun.* **7**, 1–9 (2016).
23. Pihosh, Y. *et al.* Photocatalytic generation of hydrogen by core-shell WO3/BiVO4 nanorods with ultimate water splitting efficiency. *Sci. Rep.* **5**, 1–2 (2015).
24. Kim, M. *et al.* Oxygen-Vacancy-Introduced BaSnO 3− δ Photoanodes with Tunable Band Structures for Efficient Solar-Driven Water Splitting. *Adv. Mater.* **31**, 1903316 (2019).
25. Pinaud, B. A. *et al.* Technical and economic feasibility of centralized facilities for solar hydrogen production via photocatalysis and photoelectrochemistry. *Energy Environ. Sci.* **6**, 1983–2002 (2013).
26. Glenis, S., Tourillon, G. & Garnier, F. Photoelectrochemical properties of thin films of polythiophene and derivatives: Doping level and structure effects. *Thin Solid Films* **122**, 9–17 (1984).
27. Fumagalli, F. *et al.* Hybrid organic–inorganic H 2 -evolving photocathodes: understanding the route towards high performance organic photoelectrochemical water splitting. *J. Mater. Chem. A* **4**, 2178–2187 (2016).
28. Abe, T. *et al.* Organophotocatalysis system of p/n bilayers for wide visible-light-induced molecular hydrogen evolution. *RSC Adv.* **2**, 7992 (2012).
29. Bourgeteau, T. *et al.* A H2-evolving photocathode based on direct sensitization of MoS3 with an organic photovoltaic cell. *Energy Environ. Sci.* **6**, 2706 (2013).
30. Bourgeteau, T. *et al.* Enhancing the Performances of P3HT:PCBM–MoS 3 -Based H 2 -Evolving Photocathodes with Interfacial Layers. *ACS Appl. Mater. Interfaces* 150721161652007 (2015). doi:10.1021/acsami.5b03532
31. Bourgeteau, T. *et al.* All solution-processed organic photocathodes with increased efficiency and stability via the tuning of the hole-extracting layer. *J. Mater. Chem. A* **4**, 4831–4839 (2016).
32. Rojas, H. C. *et al.* All Solution-Processed, Hybrid Organic-Inorganic Photocathode for Hydrogen Evolution. *ACS Omega* **2**, 3424–3431 (2017).
33. Guerrero, A. *et al.* Organic photoelectrochemical cells with quantitative photocarrier conversion. *Energy Environ. Sci.* **7**, 3666–3673 (2014).
34. Bellani, S. *et al.* Graphene-Based Hole-Selective Layers for High-Efficiency, Solution-Processed, Large-Area, Flexible, Hydrogen-Evolving Organic Photocathodes. *J. Phys. Chem. C* **121**, 21887–21903 (2017).
35. Francàs, L. *et al.* Rational design of a neutral pH functional and stable organic photocathode. *Chem. Commun.* **54**, 5732–5735 (2018).
36. Yao, L. *et al.* Establishing Stability in Organic Semiconductor Photocathodes for Solar Hydrogen Production. *J. Am. Chem. Soc.* **142**, 7795–7802 (2020).
37. Bellani, S., Antognazza, M. R. & Bonaccorso, F. Carbon-Based Photocathode Materials for Solar Hydrogen Production. *Adv. Mater.* **31**, 1801446 (2019).
38. Steier, L. & Holliday, S. A bright outlook on organic photoelectrochemical cells for water splitting. *J. Mater. Chem. A* **6**, 21809–21826 (2018).
39. Yao, L., Rahmanudin, A., Guijarro, N. & Sivula, K. Organic Semiconductor Based Devices for Solar Water Splitting. *Adv. Energy Mater.* **8**, 1802585 (2018).
40. Rojas, H. C. *et al.* Polymer-based photocathodes with a solution-processable cuprous iodide anode layer and a polyethyleneimine protective coating. *Energy Environ. Sci.* **9**, 3710–3723 (2016).
41. Sariciftci, N. S., Smilowitz, L., Heeger, A. J. & Wudl, F. Semiconducting polymers (as donors) and buckminsterfullerene (as acceptor): photoinduced electron transfer and heterojunction devices. *Synth. Met.* **59**, 333–352 (1993).
42. Siegmund, B. *et al.* Exciton Diffusion Length and Charge Extraction Yield in Organic Bilayer Solar Cells. *Adv. Mater.* **29**, 1–5 (2017).
43. Chi, D., Qu, S., Wang, Z. & Wang, J. High efficiency P3HT:PCBM solar cells with an inserted PCBM layer. *J. Mater. Chem. C* **2**, 4383–4387 (2014).
44. Tang, C. W. Two-layer organic photovoltaic cell. *Appl. Phys. Lett.* **48**, 183–185 (1986).
45. Li, W. *et al.* Achieving over 11% power conversion efficiency in PffBT4T-2OD-based ternary polymer solar cells with enhanced open-circuit-voltage and suppressed charge recombination. *Nano Energy*

44, 155–163 (2018).
46. Arca, F., Loch, M. & Lugli, P. Enhancing efficiency of organic bulkheterojunction solar cells by using 1,8-diiodooctane as processing additive. *IEEE J. Photovoltaics* **4**, 1560–1565 (2014).
47. Yuan, J. *et al.* Single-Junction Organic Solar Cell with over 15% Efficiency Using Fused-Ring Acceptor with Electron-Deficient Core. *Joule* **3**, 1140–1151 (2019).
48. Zhao, K. *et al.* Highly efficient organic solar cells based on a robust room-temperature solution-processed copper iodide hole transporter. *Nano Energy* **16**, 458–469 (2015).
49. Cheng, P., Li, G., Zhan, X. & Yang, Y. Next-generation organic photovoltaics based on non-fullerene acceptors. *Nat. Photonics* **12**, 131–142 (2018).
50. Xiao, Y. *et al.* Efficient ternary bulk heterojunction solar cells with PCDTBT as hole-cascade material. *Nano Energy* **19**, 476–485 (2016).
51. Li, S., Liu, W., Li, C. Z., Shi, M. & Chen, H. Efficient Organic Solar Cells with Non-Fullerene Acceptors. *Small* **13**, 1–15 (2017).
52. Lin, Y. *et al.* An Electron Acceptor Challenging Fullerenes for Efficient Polymer Solar Cells. *Adv. Mater.* **27**, 1170–1174 (2015).
53. Cui, Y. *et al.* Over 16% efficiency organic photovoltaic cells enabled by a chlorinated acceptor with increased open-circuit voltages. *Nat. Commun.* **10**, 1–8 (2019).
54. Zhang, J. *et al.* PCE11-based polymer solar cells with high efficiency over 13% achieved by room-temperature processing. *J. Mater. Chem. A* **8**, 8661–8668 (2020).
55. Baran, D. *et al.* Reducing the efficiency-stability-cost gap of organic photovoltaics with highly efficient and stable small molecule acceptor ternary solar cells. *Nat. Mater.* **16**, 363–369 (2017).
56. Gevorgyan, S. A. *et al.* Lifetime of Organic Photovoltaics: Status and Predictions. *Adv. Energy Mater.* 1–17 (2015). doi:10.1002/aenm.201501208
57. Hoke, E. T. *et al.* The role of electron affi nity in determining whether fullerenes catalyze or inhibit photooxidation of polymers for solar cells. *Adv. Energy Mater.* **2**, 1351–1357 (2012).
58. Steim, R., Kogler, F. R. & Brabec, C. J. Interface materials for organic solar cells. *J. Mater. Chem.* **20**, 2499 (2010).
59. Yip, H.-L. & Jen, A. K.-Y. Recent advances in solution-processed interfacial materials for efficient and stable polymer solar cells. *Energy Environ. Sci.* **5**, 5994 (2012).
60. Clarke, T. M. & Durrant, J. R. Charge photogeneration in organic solar cells. *Chem. Rev.* **110**, 6736–6767 (2010).
61. Roger, I., Shipman, M. A. & Symes, M. D. Earth-abundant catalysts for electrochemical and photoelectrochemical water splitting. *Nat. Rev. Chem.* **1**, 0003 (2017).
62. Giuffredi, G. *et al.* Non-Equilibrium Synthesis of Highly Active Nanostructured, Oxygen-Incorporated Amorphous Molybdenum Sulfide HER Electrocatalyst. *Small* **16**, 2004047 (2020).
63. Miyata, A. *et al.* Direct measurement of the exciton binding energy and effective masses for charge carriers in organic-inorganic tri-halide perovskites. *Nat. Phys.* **11**, 582–587 (2015).
64. D'Innocenzo, V. *et al.* Excitons versus free charges in organo-lead tri-halide perovskites. *Nat. Commun.* **5**, 1–6 (2014).
65. Green, M. A., Ho-Baillie, A. & Snaith, H. J. The emergence of perovskite solar cells. *Nat. Photonics* **8**, 506–514 (2014).
66. Kojima, A., Teshima, K., Shirai, Y. & Miyasaka, T. Organometal halide perovskites as visible-light sensitizers for photovoltaic cells. *J. Am. Chem. Soc.* **131**, 6050–6051 (2009).
67. Green, M. A. *et al.* Solar cell efficiency tables (Version 55). *Prog. Photovoltaics Res. Appl.* **28**, 3–15 (2020).
68. Tao, C. *et al.* Fully Solution-Processed n–i–p-Like Perovskite Solar Cells with Planar Junction: How the Charge Extracting Layer Determines the Open-Circuit Voltage. *Adv. Mater.* **29**, 1–7 (2017).
69. Liu, C. *et al.* Ultra-thin MoOx as cathode buffer layer for the improvement of all-inorganic CsPbIBr2 perovskite solar cells. *Nano Energy* **41**, 75–83 (2017).
70. Mosconi, E., Amat, A., Nazeeruddin, M. K., Grätzel, M. & De Angelis, F. First-principles modeling of

mixed halide organometal perovskites for photovoltaic applications. *J. Phys. Chem. C* **117**, 13902–13913 (2013).
71. Buin, A., Comin, R., Xu, J., Ip, A. H. & Sargent, E. H. Halide-Dependent Electronic Structure of Organolead Perovskite Materials. *Chem. Mater.* **27**, 4405–4412 (2015).
72. Maculan, G. *et al.* CH3NH3PbCl3 Single Crystals: Inverse Temperature Crystallization and Visible-Blind UV-Photodetector. *J. Phys. Chem. Lett.* **6**, 3781–3786 (2015).
73. McMeekin, D. P. *et al.* A mixed-cation lead mixed-halide perovskite absorber for tandem solar cells. *Science (80-.).* **351**, 151–155 (2016).
74. Kim, M. *et al.* Moisture resistance in perovskite solar cells attributed to a water-splitting layer. *Commun. Mater.* **2**, 1–12 (2021).
75. Machui, F. *et al.* Cost analysis of roll-to-roll fabricated ITO free single and tandem organic solar modules based on data from manufacture. *Energy Environ. Sci.* **7**, 2792–2802 (2014).
76. Song, Z. *et al.* A technoeconomic analysis of perovskite solar module manufacturing with low-cost materials and techniques. *Energy Environ. Sci.* **10**, 1297–1305 (2017).
77. Alfano, A. *et al.* Photoelectrochemical water splitting by hybrid organic-inorganic systems: setting the path from 2% to 20% solar-to-hydrogen conversion efficiency. *iScience* **24**, 102463 (2021).
78. Coridan, R. H. *et al.* Methods for comparing the performance of energy-conversion systems for use in solar fuels and solar electricity generation. *Energy Environ. Sci.* **8**, 2886–2901 (2015).
79. Byers, J. C., Heiser, T., Skorobogatiy, M. & Semenikhin, O. A. Effect of Aging and PCBM Content on Bulk Heterojunction Organic Solar Cells Studied by Intensity Modulated Photocurrent Spectroscopy. *ACS Appl. Mater. Interfaces* **8**, 28789–28799 (2016).
80. Yang, W. *et al.* Solar water splitting exceeding 10% efficiency: Via low-cost Sb2Se3photocathodes coupled with semitransparent perovskite photovoltaics. *Energy Environ. Sci.* **13**, 4362–4370 (2020).
81. Kim, J. Y., Lee, J. W., Jung, H. S., Shin, H. & Park, N. G. High-Efficiency Perovskite Solar Cells. *Chem. Rev.* **120**, 7867–7918 (2020).
82. Chegaar, M. *et al.* Effect of illumination intensity on solar cells parameters. *Energy Procedia* **36**, 722–729 (2013).
83. Oppedisano, D. K., Jones, L. A., Junk, T. & Bhargava, S. K. Ruthenium Electrodeposition from aqueous solution at high cathodic overpotential. *J. Electrochem. Soc.* **161**, 489–494 (2014).
84. McCrory, C. C. L. *et al.* Benchmarking Hydrogen Evolving Reaction and Oxygen Evolving Reaction Electrocatalysts for Solar Water Splitting Devices. *J. Am. Chem. Soc.* **137**, 4347–4357 (2015).
85. Cherevko, S. *et al.* Oxygen and hydrogen evolution reactions on Ru, RuO2, Ir, and IrO2 thin film electrodes in acidic and alkaline electrolytes: A comparative study on activity and stability. *Catal. Today* **262**, 170–180 (2016).
86. Heumueller, T. *et al.* Reducing burn-in voltage loss in polymer solar cells by increasing the polymer crystallinity. *Energy Environ. Sci.* **7**, 2974–2980 (2014).
87. Kawano, K. & Adachi, C. H. Evaluating carrier accumulation in degraded bulk heterojunction organic solar cells by a Thermally stimulated current technique. *Adv. Funct. Mater.* **19**, 3934–3940 (2009).
88. Salvador, M. *et al.* Burn-in Free Nonfullerene-Based Organic Solar Cells. *Adv. Energy Mater.* **7**, 1700770 (2017).
89. Wu, L., Zang, H., Hsiao, Y. C., Zhang, X. & Hu, B. Origin of the fill factor loss in bulk-heterojunction organic solar cells. *Appl. Phys. Lett.* **104**, 153903 (2014).
90. Fountaine, K. T., Lewerenz, H. J. & Atwater, H. A. Efficiency limits for photoelectrochemical water-splitting. *Nat. Commun.* **7**, 1–9 (2016).
91. Haussener, S. *et al.* Modeling, simulation, and design criteria for photoelectrochemical water-splitting systems. *Energy Environ. Sci.* **5**, 9922–9935 (2012).
92. Holmes-Gentle, I. & Hellgardt, K. A versatile open-source analysis of the limiting efficiency of photo electrochemical water-splitting. *Sci. Rep.* **8**, 1–9 (2018).
93. Hu, S., Xiang, C., Haussener, S., Berger, A. D. & Lewis, N. S. An analysis of the optimal band gaps of light absorbers in integrated tandem photoelectrochemical water-splitting systems. *Energy Environ.*

Sci. **6**, 2984–2993 (2013).
94. Jiang, Q. *et al.* Surface passivation of perovskite film for efficient solar cells. *Nat. Photonics* **13**, 460–466 (2019).
95. Menke, S. M., Ran, N. A., Bazan, G. C. & Friend, R. H. Understanding Energy Loss in Organic Solar Cells: Toward a New Efficiency Regime. *Joule* **2**, 25–35 (2018).
96. Noel, N. K. *et al.* Lead-free organic-inorganic tin halide perovskites for photovoltaic applications. *Energy Environ. Sci.* **7**, 3061–3068 (2014).
97. Rajagopal, A. *et al.* Highly Efficient Perovskite–Perovskite Tandem Solar Cells Reaching 80% of the Theoretical Limit in Photovoltage. *Adv. Mater.* **29**, 1–10 (2017).
98. Shao, S. *et al.* Highly Reproducible Sn-Based Hybrid Perovskite Solar Cells with 9% Efficiency. *Adv. Energy Mater.* **8**, 1702019 (2018).
99. Zhao, D. *et al.* Low-bandgap mixed tin-lead iodide perovskite absorbers with long carrier lifetimes for all-perovskite tandem solar cells. *Nat. Energy* **2**, 1–7 (2017).
100. Yu, X., Prévot, M. S., Guijarro, N. & Sivula, K. Self-assembled 2D WSe 2 thin films for photoelectrochemical hydrogen production. *Nat. Commun.* **6**, (2015).
101. Addou, R. & Wallace, R. M. Surface Analysis of WSe2 Crystals: Spatial and Electronic Variability. *ACS Appl. Mater. Interfaces* **8**, 26400–26406 (2016).
102. Ahn, H. S., Chizhik, S. A., Dubravin, A. M., Kazachenko, V. P. & Popov, V. V. Application of phase contrast imaging atomic force microscopy to tribofilms on DLC coatings. *Wear* **249**, 617–625 (2001).
103. Pang, G. K. H., Baba-Kishi, K. Z. & Patel, A. Topographic and phase-contrast imaging in atomic force microscopy. *Ultramicroscopy* **81**, 35–40 (2000).
104. Yannopoulos, S. N. & Andrikopoulos, K. S. Raman scattering study on structural and dynamical features of noncrystalline selenium. *J. Chem. Phys.* **121**, 4747–4758 (2004).
105. Bozheyev, F., Harbauer, K. & Ellmer, K. Highly (001)-textured p-type WSe2 Thin Films as Efficient Large-Area Photocathodes for Solar Hydrogen Evolution. *Sci. Rep.* **7**, 16003 (2017).
106. Grigoriev, S. N., Fominski, V. Y., Nevolin, V. N., Romanov, R. I. & Volosova, M. A. Control of structure of WSex/C nanocoatings synthesized via pulsed laser deposition. *Inorg. Mater. Appl. Res.* **6**, 143–150 (2015).
107. Li, H. *et al.* WSe2nanofilms grown on graphite as efficient electrodes for hydrogen evolution reactions. *J. Alloys Compd.* **725**, 884–890 (2017).
108. Yu, X. & Sivula, K. Photogenerated Charge Harvesting and Recombination in Photocathodes of Solvent-Exfoliated WSe2. *Chem. Mater.* **29**, 6863–6875 (2017).
109. Dominguez-Meister, S., Justo, A. & Sanchez-Lopez, J. C. Synthesis and tribological properties of WSex films prepared by magnetron sputtering. *Mater. Chem. Phys.* **142**, 186–194 (2013).
110. Grigoriev, S. N. *et al.* Formation of thin catalytic WSe x layer on graphite electrodes for activation of hydrogen evolution reaction in aqueous acid. *Inorg. Mater. Appl. Res.* **7**, 285–291 (2016).
111. Lei, B. *et al.* Nondestructive hole doping enabled photocurrent enhancement of layered tungsten diselenide. *2D Mater.* **6**, (2019).
112. Almadori, Y., Bendiab, N. & Grévin, B. Multimodal Kelvin Probe Force Microscopy Investigations of a Photovoltaic WSe2/MoS2 Type-II Interface. *ACS Appl. Mater. Interfaces* **10**, 1363–1373 (2018).
113. Wang, K. *et al.* Interlayer Coupling in Twisted WSe2/WS2 Bilayer Heterostructures Revealed by Optical Spectroscopy. *ACS Nano* **10**, 6612–6622 (2016).
114. Cui, Z. *et al.* Effect of vacancy defect on optoelectronic properties of monolayer tungsten diselenide. *Opt. Quantum Electron.* **50**, 1–9 (2018).
115. Sokolikova, M. S., Sherrell, P. C., Palczynski, P., Bemmer, V. L. & Mattevi, C. Direct solution-phase synthesis of 1T' WSe 2 nanosheets. *Nat. Commun.* **10**, (2019).
116. Ding, Y. *et al.* First principles study of structural, vibrational and electronic properties of graphene-like MX2 (M=Mo, Nb, W, Ta; X=S, Se, Te) monolayers. *Phys. B Condens. Matter* **406**, 2254–2260 (2011).
117. Zhao, W. *et al.* Evolution of Electronic Structure in Atomically Thin Sheets of WS 2 and WSe 2. *ACS*

Nano **7**, 791–797 (2013).
118. McDonnell, S. *et al.* Hole contacts on transition metal dichalcogenides: Interface chemistry and band alignments. *ACS Nano* **8**, 6265–6272 (2014).
119. Id, M. *et al.* Enhanced Hole Injection into Single Layer WSe 2. **6**, 309–313 (2017).
120. Eng, A. Y. S., Ambrosi, A., Sofer, Z., Šimek, P. & Pumera, M. Electrochemistry of transition metal dichalcogenides: Strong dependence on the metal-to-chalcogen composition and exfoliation method. *ACS Nano* **8**, 12185–12198 (2014).
121. Shtansky, D. V. *et al.* Structure and properties of multi-component and multilayer TiCrBN/WSex coatings deposited by sputtering of TiCrB and WSe2 targets. *Surf. Coatings Technol.* **202**, 5953–5961 (2008).
122. Cao, W. *et al.* Designing band-to-band tunneling field-effect transistors with 2D semiconductors for next-generation low-power VLSI. *Tech. Dig. - Int. Electron Devices Meet. IEDM* **2016**-**Febru**, 12.3.1-12.3.4 (2015).
123. Guo, Y. *et al.* Probing the Dynamics of the Metallic-to-Semiconducting Structural Phase Transformation in MoS2 Crystals. *Nano Lett.* **15**, 5081–5088 (2015).
124. Byrley, P., Liu, M. & Yan, R. Photochemically induced phase change in monolayer molybdenum disulfide. *Front. Chem.* **7**, 1–9 (2019).
125. Lu, Q., Yu, Y., Ma, Q., Chen, B. & Zhang, H. 2D Transition-Metal-Dichalcogenide-Nanosheet-Based Composites for Photocatalytic and Electrocatalytic Hydrogen Evolution Reactions. *Adv. Mater.* **28**, 1917–1933 (2016).
126. Mezzetti, A. *et al.* Stable hybrid organic/inorganic photocathodes for hydrogen evolution with amorphous WO<inf>3</inf>hole selective contacts. *Faraday Discuss.* **198**, (2017).
127. Pirelli. Power is Nothing Without Control. (1993). Available at: https://www.pirelli.com/global/it-it/life/power-is-nothing-without-control-compie-25-anni. (Accessed: 21st March 2021)
128. Pastor, E. *et al.* Spectroelectrochemical analysis of the mechanism of (photo)electrochemical hydrogen evolution at a catalytic interface. *Nat. Commun.* **8**, (2017).
129. Byers, J. C., Ballantyne, S., Rodionov, K., Mann, A. & Semenikhin, O. A. Mechanism of recombination losses in bulk heterojunction P3HT: PCBM solar cells studied using intensity modulated photocurrent spectroscopy. *ACS Appl. Mater. Interfaces* **3**, 392–401 (2011).
130. Bertoluzzi, L. & Bisquert, J. Equivalent circuit of electrons and holes in thin semiconductor films for photoelectrochemical water splitting applications. *J. Phys. Chem. Lett.* **3**, 2517–2522 (2012).
131. Klahr, B., Gimenez, S., Fabregat-Santiago, F., Bisquert, J. & Hamann, T. W. Photoelectrochemical and impedance spectroscopic investigation of water oxidation with 'co-Pi'-coated hematite electrodes. *J. Am. Chem. Soc.* **134**, 16693–16700 (2012).
132. Moehl, T., Cui, W., Wick-Joliat, R. & Tilley, S. D. Resistance-based analysis of limiting interfaces in multilayer water splitting photocathodes by impedance spectroscopy. *Sustain. Energy Fuels* **3**, 2067–2075 (2019).
133. Cui, W., Moehl, T., Siol, S. & Tilley, S. D. Operando electrochemical study of charge carrier processes in water splitting photoanodes protected by atomic layer deposited TiO2. *Sustain. Energy Fuels* **3**, 3085–3092 (2019).
134. Naito, T., Shinagawa, T., Nishimoto, T. & Takanabe, K. Water Electrolysis in Saturated Phosphate Buffer at Neutral pH. *ChemSusChem* **13**, 5921–5933 (2020).
135. Roy, P., Kumar Sinha, N., Tiwari, S. & Khare, A. A review on perovskite solar cells: Evolution of architecture, fabrication techniques, commercialization issues and status. *Sol. Energy* **198**, 665–688 (2020).
136. Vo, T. G., Chiu, J. M., Tai, Y. & Chiang, C. Y. Turnip-inspired BiVO4/CuSCN nanostructure with close to 100% suppression of surface recombination for solar water splitting. *Sol. Energy Mater. Sol. Cells* **185**, 415–424 (2018).
137. Arora, N. *et al.* Perovskite solar cells with CuSCN hole extraction layers yield stabilized efficiencies greater than 20%. *Science (80-.).* **358**, 768–771 (2017).

138. Kung, P. K. *et al.* A Review of Inorganic Hole Transport Materials for Perovskite Solar Cells. *Adv. Mater. Interfaces* **5**, 1–35 (2018).
139. Bellani, S. *et al.* Reversible P3HT/Oxygen Charge Transfer Complex Identi fi cation in Thin Films Exposed to Direct Contact with Water. *J. Phys. Chem. C* **118**, 6291–6299 (2014).
140. Tilley, S. D., Schreier, M., Azevedo, J., Stefik, M. & Grätzel, M. Ruthenium Oxide Hydrogen Evolution Catalysis on Composite Cuprous Oxide Water Splitting Photocathodes. *Adv. Funct. Mater.* **24**, 303–311 (2014).